2012

Measuring Actin Dynamics Through Image Analysis and Modeling

Matthew Bruce Smith
Lehigh University

Measuring Actin Dynamics Through Image Analysis and Modeling

by

Matthew B. Smith

A Dissertation
Presented to the Graduate Committee
of Lehigh University
in Candidacy for the Degree of
Doctor of Philosophy
in
Physics

Lehigh University
September 2012

Approved and recommended for acceptance as a dissertation in partial fulfillment of the requirements for the degree of Doctor of Philosophy.

Matthew B. Smith
Measuring Actin Dynamics Through Image Analysis and Modeling

Date

Dimitrios Vavylonis, Dissertation Director, Chair

Accepted Date

Committee Members

Ivan Biaggio

James D. Gunton

Yong W. Kim

Xiaolei Huang

Contents

List of Tables

List of Figures

ABSTRACT

In this work I use modeling and image analysis to study the dynamics of the actin cytoskeleton. Actin is a protein that polyermizes into filaments. Actin plays an important role in many functions of the cell: it is a dynamic facet of the cytoskeleton that helps cells determine their shape; it is a principal component of mechanisms used for cell motility; and it is fundamental to cytokinesis during cellular division. In vitro experiments have helped to understand many aspects of actin polymerization, but the kinetics of actin polymerization in live cells often reveal surprising results. New live cell experimental techniques make it possible to measure the kinetics, localization, and abundance of proteins with ever greater precision. These novel techniques create challenges for both extracting data from complex images, and mathematical modeling to interpret the underlying mechanisms.

The first type of experiment I examine allows measurement of growth rates and persistence length of actin polymers in vitro. In this method researchers polymerize actin filaments on a glass slide with fluorescently labeled actin. Individual actin filaments can then be imaged over time using time-lapse Total Internal Reflection Fluorescence (TIRF) microscopy. To address the challenge of measuring actin filaments quickly and accurately I developed an interactive software tool for segmentation, tracking, and visualization of individual fibers. The algorithm used is called Stretching Open Active Contours. Open active contours are parametric curves that deform to minimize the sum of an external energy derived from the image and an internal bending and stretching energy. Images of simulated semiflexible polymers with known bending and torsional rigidity are analyzed to validate the method. This method was used successfully to measure the curvature and tangent correlations of actin filaments imaged by TIRF microscopy in vitro. It was also used to measure curvature distributions for 3D image stacks of actin cables in fission yeast, imaged by spinning disk confocal microscopy.

The second type of experiments are live cell experiments that demand computational image analysis. In experiments performed by the group headed by Naoki Watanabe, the kinetics of actin can be observed through single molecule speckle (SiMS) microscopy of lamellipodia. Lamellipodia are flat ($\sim$ 200nm thick) protrusions that cells use to crawl on flat surfaces. By imaging the lamellipodium of cells expressing low concentrations of labeled protein, the behavior of single actin proteins can be observed. Labeled proteins appear as speckles when they are part of an actin

filament. When a speckle appears it corresponds to actin polymerization and when a speckle disappears it corresponds to depolymerization. Locating and tracking speckles is very tedious due to the low signal to noise and due to the different structures found near the lamellipodium. I present a program, Speckle TrackerJ, which addresses some of these challenges using computer assisted techniques for finding positions and tracking particles in different situations. A dynamic user interface assists in creating, editing and refining particle tracks. This program has been useful for measuring actin and related proteins in the cytoskeleton. For example, we used the program to measure the diffusion coefficient of capping proteins (CP) in the lamellipodium and we efficiently measured the appearance and disappearance of EGFP-actin speckles within the lamellipodium of motile cells. By measuring the appearance and disappearance of actin speckles we observe the kinetics of actin binding to the filamentous network in the lamellipodium. This program was also able to assist in tracking vesicles in supported lipid bilayer experiments performed by E. Karatekin and A. Gohlke.

Finaly, I use modeling combined with results of the previous experiments to interpret the results of live cell experiments using Fluorescent Recovery After Photobleaching (FRAP). Prior FRAP experiments using EGFP-actin have suggested that polymerization occurs exclusively at the leading edge of motile cells. This result contradicts results from the SiMS experiments where recovery occurs throughout the lamellipodium. To compare these two types of experiments I used the statistics obtained from SiMS experiments to create a model for the steady state distribution and kinetics of actin in the lamellipodium. I used this model to demonstrate that by including two species of diffuse actin both types of experiments, FRAP and SiMS, do not contradict each other. The second species of diffuse actin consists of slowly diffusing oligomers that associate to the F-actin network throughout the lamellipodium or break up into monomers after a characteristic time. Our work motivates studies to test the presence and composition of slowly diffusing actin species that may contribute to local remodeling of the actin network and increase the amount of soluble actin available for polymerization.

Chapter 1

Actin polymerization and the lamellipodium

1.1 BACKGROUND

1.1.1 Actin is part of the machinery of crawling cells

Active cell motion is found in a wide range of organisms, such as the "run and tumble" motions of the bacteria *Escherichia coli* [1], to white blood cells in our immune system [2]. In both of these examples the cells build complicated structures out of proteins to produce motility. The subject of this work is motility based on the actin cytoskeleton. Actin plays an important role in cell motility [3], it helps cells determine their shape [4], and it is fundamental to cytokinesis during cell division [5]. One of the best systems to study actin based motility are cells that crawl using a lamellipodium. Lamellipodia are thin sheet like structures that protrude along a surface (see Fig. 1.1). Lamellipodia protrusions are approximately 200 nm thick and extend several micrometers from the body of the cell. The basic structure of the lamellipodium is a plasma membrane supported by a dendritic network of actin filaments (Fig. 1.2). Protrusion of lamellipodia is driven by polymerization of actin monomers into filaments at the leading edge.

The organization of actin into the branched network seen in Fig. 1.2B requires many proteins. In addition to actin, lamellipodia are characterized by actin filament nucleating proteins such as: the Arp2/3 complex; adhesion proteins that cross the plasma membrane to interact with the surroundings; proteins that attach to the ends of filaments and prevent polymerization, such as Capping Protein (CP); and

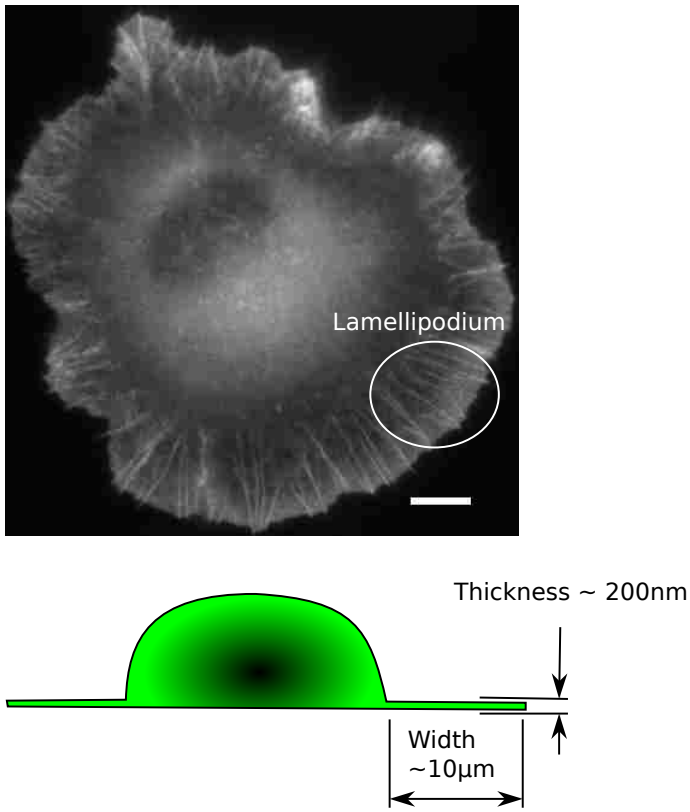

Figure 1.1: Overview of a cell with a lamellipodium. The top image is an epifluorescent image of a XTC cell expressing EGFP-actin [6]. The lamellipodium goes around the circumference of this cell and gives it a "fried egg" morphology (Scale bar: 8 μm). The bottom cartoon depicts a side view of the cell, to show how the lamellipodium would compared to the body of the cell.

proteins that bind and sever actin filaments such as ADF/cofilin. The roles of some of these proteins are described in the dendritic nucleation model of the lamellipodia (see Section 1.1.4).

1.1.2 Basics of actin polymerization

Actin can exist either as a monomer (globular or "G-actin") or as a polymer (filamentous or "F-actin"). Actin filaments are polarized with a "barbed" end and a "pointed" end (see Fig. 1.3A). The names barbed and pointed are a reference to the way actin filaments looked in early electron micrographs where actin was imaged while bound to myosin [8, 9].

Each end of an actin filament has different polymerization rates and different

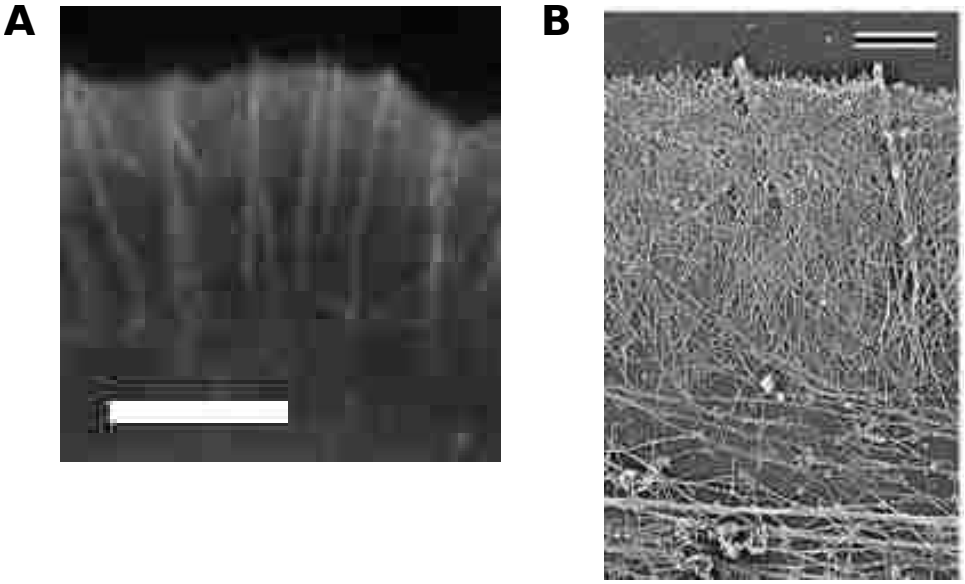

Figure 1.2: Electron Microscopy reveals the actin network in the lamellipodium. A) Cropped region from the cell showing in Fig. 1.1. Scale bar: 8 μm. B) Electron Micrograph of a Xenopus fibroblast from Ref. [7] shows the dense brush-like network of actin filaments at the leading edge. Scale bar: 1 μm.

steady-state conditions depending on the state of the actin monomers. The state of an actin subunit is determined by a bound nucleotide. Each actin subunit has a binding cleft where it can bind a nucleotide, either ATP or ADP (Fig. 1.3B). G-actin can bind both ATP and ADP, but because ATP exists in excess in the cytoplasm a majority of actin available for polymerization is G-actin bound to ATP ("ATP-actin"). ATP-actin polymerizes faster at the barbed ends of actin filaments than at the pointed ends (see Fig. 1.3A). Shortly after being polymerized, ATP-actin subunits hydrolyze the ATP into an ADP and a phosphate, Pi, at a rate of 0.3 s^{-1} [10, 11]. A subunit with ADP and Pi is ADP-Pi-actin. Phosphate release into solution occurs at a rate of 0.003 s^{-1} [10] and the subunit becomes ADP-actin. This is one way that actin polymerization consumes energy, which can be used by cells for directed motion and organized structures required for cellular functions.

One technique used to measure actin polymerization uses a fluorescent dye, pyrene [14]. Pyrene can be covalently bound to actin monomers and used to polymerize with a mixture of labeled and unlabeled actin subunits. Filamentous pyrene-actin is ~ 20 times brighter than monomeric pyrene-actin [10], so the amount of polymerized

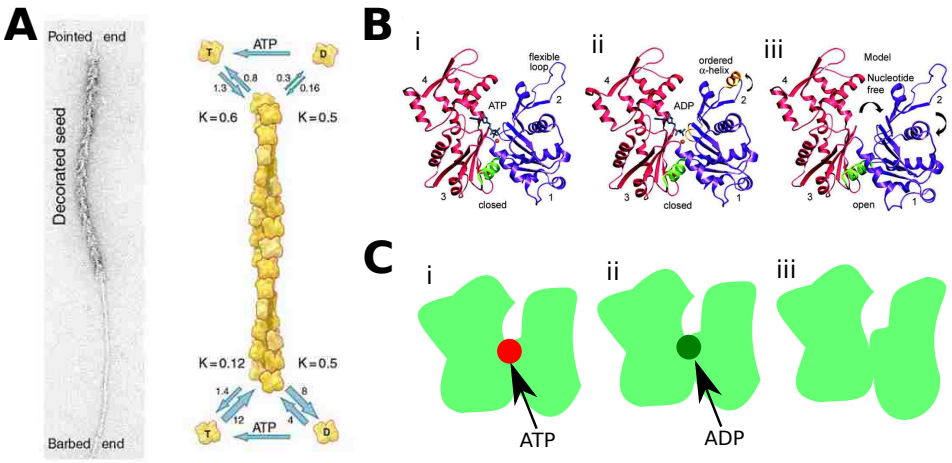

Figure 1.3: A) Actin filaments from Ref. [12]. Left: EM picture of an actin filament that has been decorated by myosin heads and then allowed to polymerize again. The shape of the myosin attached the the actin filaments resembles an arrowhead. That is how the barbed and pointed ends were named. The undecorated ends of the filament show that the barbed end grew much faster than the pointed end. Right: Schematic of the polymerization rates at the different ends of the filament. Labels T, D represent the type of nucleotide (ATP or ADP, respectively) that is bound to the actin subunit. Actin subunits hydrolyze ATP into ADP when they are in a filament; when they are in solution they will replace the ADP with ATP. B) Crystal structure of actin monomers with different bound nuecleotides from ref.[13]. i) ATP-actin ii) ADP-actin and iii) actin without the bound nucleotide and divalent ion which is required for actin polymerization. C) Cartoon representation of B.

actin can be measured by measuring the total fluorescence intensity as a function of time. When salt is added to a low-salt solution of labeled and unlabeled monomers, polymerization begins. Experiments with pyrene-actin show that low concentrations of actin ($< 10\mu$M) have a significant delay in polymerization. This is due to slow nucleation of actin filaments: actin monomers need to first form a stable trimer or tetramer before it can polymerize into filaments [14]. After the initial delay, the rate of polymerization increases rapidly, possibly due to the addition of barbed ends created by fragmentation [14]. This process continues until most of the available actin is consumed and the remaining actin in solution is at the critical concentration, $\sim 0.1\mu$M [15]. When the solution reaches a steady state, there is still turnover in the polymerized actin because of the ATP-actin hydrolysis cycle. ATP-actin, ADP-Pi-actin and ADP-actin have different critical concentrations and at steady state the

barbed end is polymerizing while the pointed end is shrinking [15, 16].

Pyrene fluorescence assays are a powerful tool that allowed measurements of actin polymerization in real time during the 1980's and 1990's. These assays measure actin polymerization in bulk experiments, where the behavior of individual filaments needs to be inferred from the results. They also involve complications when actin binding proteins alter the pyrene fluorescence. A more recent technique used to measure actin polymerization is Total Internal Reflection Fluorescence (TIRF) microscopy [17]. TIRF enables imaging individual actin filaments as they grow in real time (see Fig. 1.4). In these experiments a solution containing actin monomers covalently bound to a fluorescent dye such as Alexa 488, and unlabeled actin monomers is contained above a slide. The slide is coated with proteins that attach to actin filaments. The slide is illuminated by an evanescent wave so that only the fluorescent proteins near the slide, < 200nm, are illuminated. Only actin filaments that are attached to the slide will be close enough to be illuminated and the result is a clear image of individual filaments as they polymerize (see Fig. 1.4). In addition to imaging actin filaments, the interaction of other proteins and actin filaments can also be studied using this technique.

Although TIRF improves the ability to observe actin polymerization, it also creates new challenges regarding analysis. For example, in order to measure polymerization kinetics, filaments need to be quickly and accurately tracked. I addressed this issue by writing a program for tracking filaments described in Chapter 2.

1.1.3 Regulation of actin polymerization

One way to control actin polymerization is through the nucleation of new filaments. The actin related protein complex, Arp2/3, is one of the major actin filament nucleators in cells. Arp2/3 protein complex contains seven proteins. Two of these proteins, Arp 2 and 3, are similar in structure to actin monomers [18]. Arp2/3 nucleates actin filaments by branching off of existing filaments (see Fig. 1.5A). Arp2/3 anchors the pointed end of the daughter filament to the mother filament at an angle of 70 degrees. When ATP-actin is polymerized *in vitro*, more branches are found on the younger parts of mother filaments [17]. Further evidence has shown that this is because Arp2/3 mediated branches are more stable when the mother filament is ATP-actin or ADP-Pi-actin compared to ADP-actin [19].

Another important protein is profilin. Profilin regulates actin polymerization in

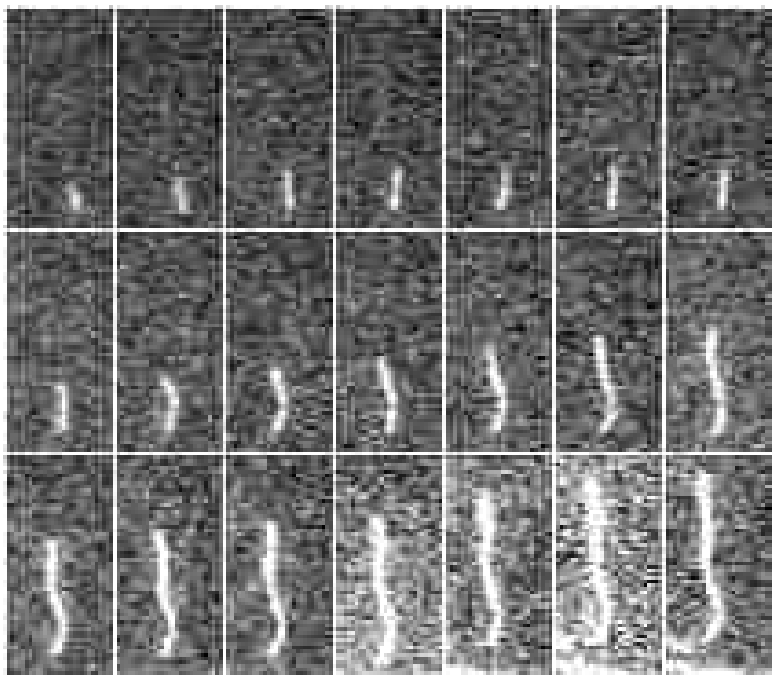

Figure 1.4: An actin filament with Alexa 488 labeled subunits growing in a TIRF microscopy experiment. The filament is growing on a slide that is being illuminated by a laser reflected off of the slide. The total internal reflection causes an evanescent wave to illuminate only the fluorescent subunits that are attached to the slide. The time between frames is 10 seconds apart and the final length is $\sim 10\mu$m. There are approximately 237 subunits per μm. Images were provided by I. Fujiwara and the experimental details have been published in [15].

multiple ways. It binds to free actin monomers (see Fig. 1.5B) and increases the rate of nucleotide exchange [10]. Profilin works in conjunction with Thymosin-β_4, a protein that binds and sequesters G-actin, to maintain a pool of free G-actin. Profilin allows G-actin to bind to the barbed end of filaments but restricts growth from the pointed end[16]. It suppresses spontaneous nucleation, which is very fast at physiological concentrations of G-actin $\sim 100\mu$M. It can also bind to the barbed ends of filaments, and when in high concentration can restrict polymerization [24]. Profilin also causes an increase in the amount of Arp2/3 mediated branching [17].

A protein that is critical for the regulation of actin turnover is Cofilin. Cofilin is a protein that binds to the sides of filaments (see Fig. 1.5C), especially ADP-actin and severs them into smaller pieces [10]. Cofilin accelerates Pi release [25]. It can also bind to G-actin monomers. It's primary function appears to be to increase F$\rightarrow$G

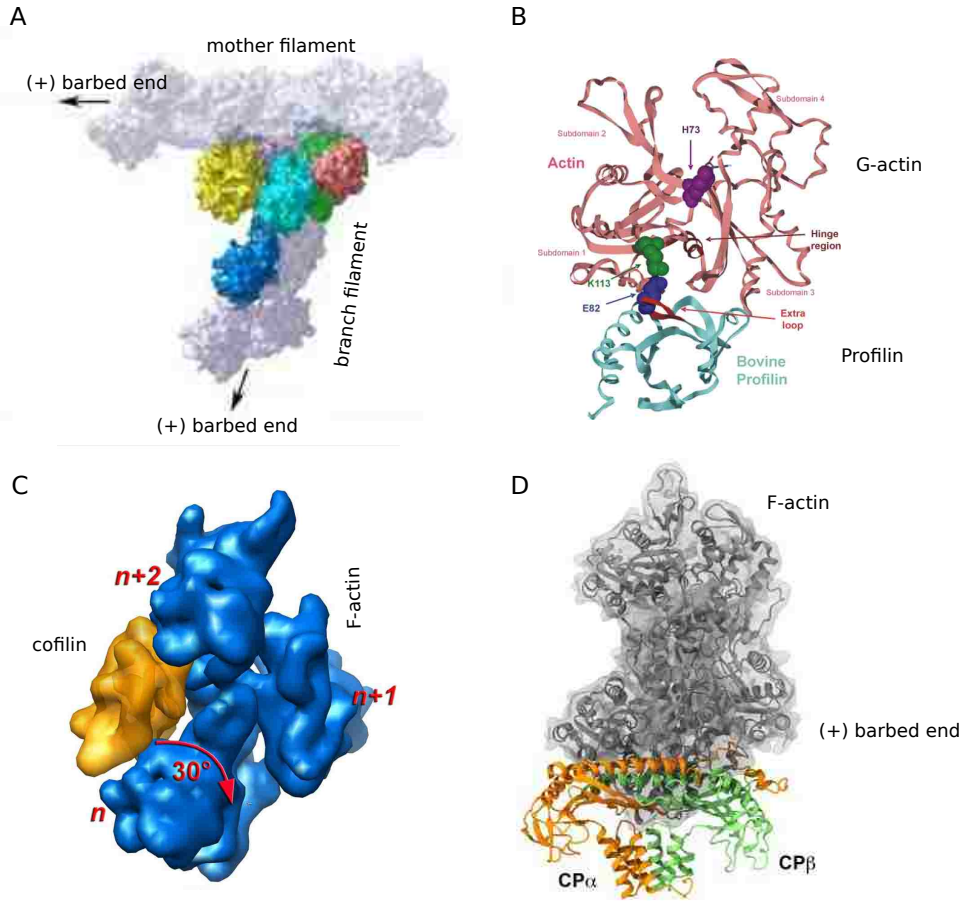

Figure 1.5: A) Model of activated Arp2/3 complex from Ref. [20]. By binding to the sides of existing actin filaments, Arp2/3 nucleates new filaments. Two of the proteins in the Arp2/3 complex, Arp2 and Arp3, are very similar to actin monomers. B) Co-crystal structure of β-actin (light-red) and bovine profilin (light blue) from Ref. [21]. C) Pseudoatomic model of cofilin bound to filamentous actin, where the actin filament has undergone a conformational change due to the binding of cofilin. From Ref. [22]. D) CP/F-actin model of CP bound to F-actin at the barbed end, from Ref. [23]. CP is a heterodimer with a CPα subunit and a CPβ subunit, shown in orange and green respectively.

turnover through severing and possibly in cooperation with other proteins such as Aip1 [26].

Another important protein is capping protein (CP) [23]. CP is a heterodimer that binds to the barbed ends of actin filaments (see Fig. 1.5) and blocks polymerization. In the presence of profilin, CP effectively blocks polymerization. This is because profilin can reduce both the rates of nucleation and pointed-end polymerization, while

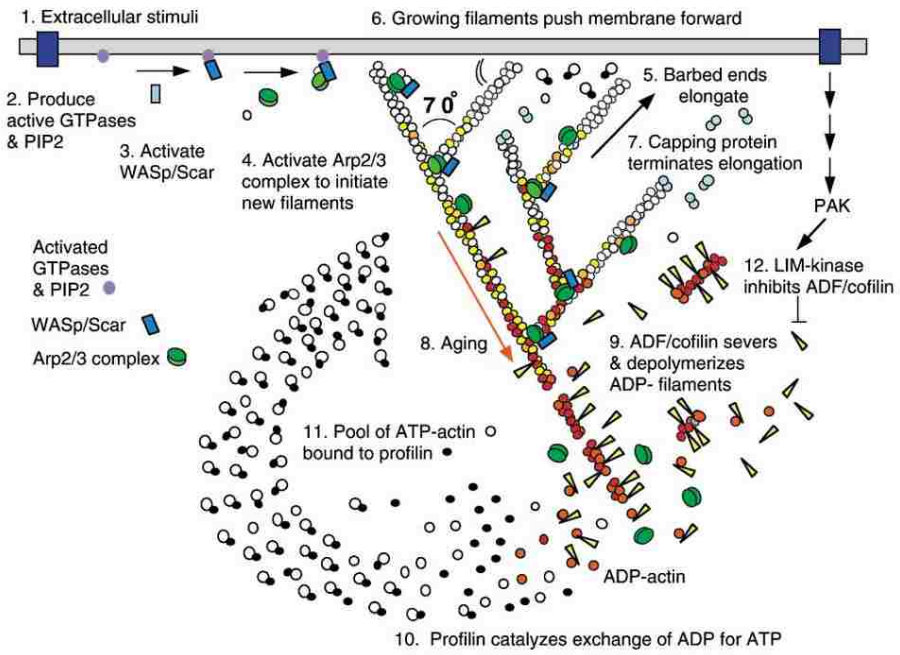

Figure 1.6: Dendritic Nucleation/Array Treadmilling Model for Protrusion of the Leading Edge [12].

CP blocks the barbed end [25].

I have described some of the more well known proteins that participate in the regulation of actin polymerization based on in vitro experiments. Unfortunately in live cells the behavior of proteins may not be the identical to the behavior seen in vitro. These differences make it nescessary to also study the polymerization kinetics of actin in living cells. The lamellipodium is a good system for performing such studies due to it's geometry and because many of the proteins characteristic of lamellipodia are well studied.

1.1.4 Dendritic nucleation model

In preceding section I briefly introduced some of the more important actin polymerization regulating proteins in the lamellipodium. These studies have been used to develop the dendritic nucleation model [12] shown in Fig. 1.6.

Starting at the leading edge there are receptors that respond to external signals

and activate protein WASP (Wiskott-Aldrich Syndrome Protein). WASP in turn activates Arp2/3 complex. The Arp2/3-initiated branches form at an angle of about 70 degrees from the mother actin filament [12]. This process is believed to generate the branched structure seen in Fig. 1.2. Nucleation by the Arp2/3 complex is autocatalytic because creation of more filaments allows further branching sites. This would lead to unbounded growth in the number of barbed ends. CP limits this growth by binding reversibly to the barbed ends of actin filaments and preventing both polymerization and depolymerization. It has been suggested that CP helps to funnel free subunits to the leading edge by blocking the polymerization of filaments growing at a distance from the leading edge, which will keep the free monomer pool high [27].

Actin is also recycled, by the disassembly of filaments. Aged actin filaments are primarily ADP-actin with ADF/cofilin bound to the sides. ADF/cofilin causes filament severing (see Fig. 1.6). Other proteins such as Aip1 may cooperate with ADF/cofilin to destabilize actin filaments [28]. The ADP-actin monomers in the cytoplasm then exchange ADP for ATP with the help of profilin, so that they can reassemble at the barbed ends near the leading edge. Throughout this process the actin network is undergoing "retrograde flow": even though the leading edge is protruding or stationary, the actin filaments themselves are moving backwards towards the center of the cell.

Figure 1.6 shows a cartoon of what is happening in the cell, but the kinetics of proteins and their functions in the lamellipodium is still an active area of research, with many questions remaining.

1.1.5 Fluorescence microscopy methods to study dynamics at the leading edge.

In the previous sections I have discussed studies that use chemical dyes to label actin proteins. In these studies purified actin is combined with dyes and allowed to bind covalently to actin and then the labeled actin can be used for polymerization. One challenge to combine this technique with living cells is getting the dyes into the cells. One way to do this is to use chemicals to fix the cell, so that components to do not move any more and then use a detergent to remove the plasma membrane. A common way to incorporate a dye is to label the toxin phalloidin [29]. Phalloidin binds to actin filaments and prevents depolymerization. While this is adequate for studying the steady state distribution of actin, it is not ideal for studying the dynamics

of polymerization. Another technique used to incorporate dyes into living cells is to inject the labeled proteins into the cells via microinjection [30] or electroporation [31], which reversibly ruptures the membranes so that there is fluid transfer between the cell and the solution. This technique enables looking at the dynamics of labeled proteins. However, the dyes and antibodies used to stain the particles or proteins might cause side-effects to the host organism.

A revolutionary technique to study proteins in living cells uses Green Fluorescent Protein (GFP) [32]. This fluorescent protein from the *Aequorea* jellyfish was successfully cloned and expressed in organisms other than the *Aequorea*. Cells can be modified to produce GFP using their own machinery, without the requirement of any jellyfish-specific enzymes to cause fluorescence. The gene that encodes for GFP can also be combined with a gene that encodes for a protein and when the cell produces that protein, it is labeled with GFP. While this technique is widely used, occasionally the mutation can be fatal or seriously alter the behavior of cells because it interferes with the function of the endogenous protein. Imaging cells containing GFP can be challenging due to photobleaching and blinking [33].

Fluorescence microscopy has been used to monitor the dynamics of actin and regulators at the leading edge [7, 34–41]. By introduction of fluorescently labeled proteins using genetic methods or microinjection, the dynamics of assembly and disassembly can be monitored in live cells [37, 39, 41–44]. At high concentrations of fluorescent actin, the actin network at the leading edge appears as a uniform intensity field (see Fig. 1.7A). At lower concentrations of actin markers, the actin appears as "speckles" which can be small aggregates of 3-5 fluorophores [45] or single molecules [41] (see Fig. 1.7B).

Another type of experiment that uses fluorescence to probe protein dynamics is Fluorescent Recovery After Photobleach (FRAP). This method takes advantage of the fact that fluorophores bleach under high illumination. A high intensity laser is used to bleach a region of fluorecently labeled proteins. The rate of fluorescence recovery depends on their how the protein behaves. This technique can be used to measure diffusion coefficients, and binding and unbinding rates [46]. It has also been applied to study dynamics and localization of actin polymerization in the lamellipodia [43, 44].

In this thesis I present work from a collaboratory effort with Naoki Watanabe (Laboratory of Single-Molecule Cell Biology, Tohoku University Graduate School

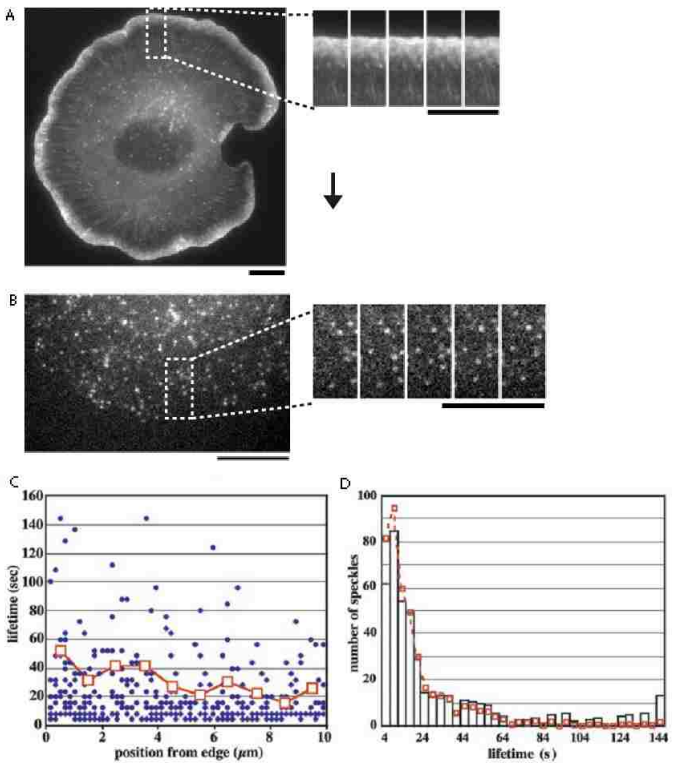

Figure 1.7: Images of cell at different fluorescent marker concentration. (A) Image of an XTC on poly-L-lysine coated slide (Naoki Watanabe, Laboratory of Single-Molecule Cell Biology, Tohoku University Graduate School of Life Sciences, Sendai, Miyagi, Japan). B) A similar cell with a much lower marker count, diluted to 1: 100000. Only immobilized markers show up as speckles. Scale bars: 10μm C) Speckle lifetime versus distance from leading edge. Blue circles show lifetime at appearance location. Red boxes are average lifetime with calibration for photobleaching [41]. D) Histogram of speckle lifetimes [41].

of Life Sciences, Sendai, Miyagi, Japan) who has developed single molecule speckle (SiMS) microscopy for imaging single molecules in lamellipodia. In his experiments low concentration of markers (GFP or dye labeled actin) are used and the result is an image of speckles (see Fig. 1.7B). A speckle is a stationary fluorescent marker that corresponds to a polymerized protein [39, 41, 47]. A diffuse particle, one that is not bound to the actin network, still contributes light but it does not form a speckle because of its motion during image acquisition [6].

1.2 MOTIVATION AND OUTLINE

Understanding the behavior of proteins in cells combines a number of processes: identifying interacting proteins, understanding in vitro properties, and characterizing their behavior in the cells. The lamellipodium is a great system for studying the actin cytoskeleton since many of these steps have significant progress. The three main goals of this thesis contribute to the field of actin dynamics as follows.

First, improve techniques for extracting relevant data from fluorescent microscopy images. Studies of actin polymerization rates using TIRF microscopy vitro [15, 48] demonstrate a need for reliably extracting the shapes of linear elements. I have developed a tool for measuring the linear structures in fluorescent microscopy.

Second, develop a method for analyzing images of live cells from SiMS microscopy. This task is very tedious due to the low signal to noise, and the heterogeneous composition of cells. To address these challenges I wrote a new tool, Speckle TrackerJ, which uses computer assisted techniques for finding positions and tracking particles in different situations.

Third, model actin turnover in the lamellipodium and compare it to the results obtained from two different experimental techniques. The model describes the overall actin concentration profile and simulates FRAP recovery based on data from SiMS experiments. Studies of actin dynamics at the leading edge of motile cells with single molecule speckle (SiMS) microscopy have shown a broad distribution of EGFP-actin speckle lifetimes and indicated actin polymerization and depolymerization over an extended region. Other experiments using FRAP with the same EGFP-actin as a probe have suggested, by contrast, that polymerization occurs exclusively at the leading edge.

The following sections contain a brief outline of the remaining chapters in this thesis.

1.2.1 Extracting filament structures from fluorescence microscopy images

I wrote a software tool, "JFilament," based on an algorithm developed during a collaboration with Dr X. Huang at the P.C. Rossin College of Engineering and Applied Science, Lehigh University. The algorithm uses stretching open active contours to measure the growth rate of actin filaments in TIRF microscopy [49]. Stretching open

active contours are parametric curves that deform to minimize the sum of an external energy derived from the image and an internal bending and stretching energy. The external energy generates (i) forces that attract the contour towards the central bright line of a filament in the image, and (ii) forces that stretch the active contour towards the ends of bright ridges. The algorithm has been useful for a variety of applications. Chapter 2 describes JFilament a tool for segmentation, tracking, and visualization of individual fibers. Images of simulated semiflexible polymers with known bending and torsional rigidity are analyzed to validate the method. This method is used to quantify the conformations and dynamics of actin in two examples: actin filaments imaged by TIRF microscopy in vitro, and actin cables in fission yeast imaged by spinning disk confocal microscopy.

1.2.2 Particle tracking in fluorescence microscopy

In Chapter 3 I address some challenges using computer assisted techniques for finding positions and tracking particles in speckle microscopy. I wrote Speckle TrackerJ with a dynamic user interface to assist in creating, editing and refining particle tracks. The following are results from application of this program: (1) Tracking single molecule diffusion in simulated images. The shape of the diffusing marker on the image changes from speckle to cloud, depending on the relationship of the diffusion coefficient to the camera exposure time. We use these images to illustrate the range of diffusion coefficients that can be measured. (2) We used the program to measure the diffusion coefficient of capping proteins (CP) in the lamellipodium. We found values of order 0.5 μm^2/s, suggesting CP association with protein complexes or the membrane. (3) We demonstrate efficient measuring of appearance and disappearance of EGFP-actin speckles within the lamellipodium of motile cells that indicate actin monomer incorporation into the actin filament network. (4) We marked appearance and disappearance events of fluorescently-labeled vesicles to supported lipid bilayers and tracked single lipids from the fused vesicle on the bilayer. This is the first time that vesicle fusion has been detected with single molecule sensitivity and the program allowed us to perform a quantitative analysis. (5) By discriminating between undocking and fusion events, dwell times for vesicle fusion following vesicle docking to membranes can be measured.

1.2.3 Theoretical model of actin turnover in the lamellipodium

Chapter 4 is a theoretical study of actin turnover in the lamellipodium. I used data from single molecule experiments by Naoki Watanabe to create a steady state profile of actin in the lamellipodium. From the steady state profile we can calculate the G-actin depletion near the leading edge. Knowing the steady state G-actin concentration I created a 2D stochastic simulation to explore a long standing issue in the field that has been divided by seemingly contradicting experimental results: where does actin polymerization occur in the lamellipodium?

We focus on two types experiments for our analysis, namely Fluorescence recovery after photobleaching (FRAP) [43] and Single Molecule Speckle (SiMS) microscopy [41]. FRAP shows very little fluorescent actin recovery away from the leading edge, which has been interpreted as a lack of actin turnover away from the leading edge. These experiments support a whole network treadmilling model in which actin polymerization occurs almost exclusively at the leading edge. Conversely, SiMS microscopy shows actin turnover throughout the lamellipodium. Other studies also suggest a capacity for remodeling throughout lamellipodia [36, 39, 40, 45, 47, 50–52].

By using the model I developed we were able to compare the two experimental results (FRAP and SiMS). The model uses the statistics of actin polymerization from SiMS to simulate FRAP in the lamellipodium. The recovery is measured in two regions, the front and back for comparison with experiments. There is good agreement between the experiment and model, except for the recovery at the back. In the model with actin monomers as the only diffuse species recovery at the back is too fast. To explore possible sources of these differences, we consider actin existing as oligomers in the lamellipodium. The model containing oligomers is in better agreement with the FRAP experiments and demonstrates that remodeling could be happening throughout the lamellipodium.

Chapter 2

Extracting filament structures from fluorescent microscopy images

This chapter describes the work performed with post-doctoral researcher Eddy Yusuf and members of Dr. Xiaolei Huang's group, Tian Shen, and Hongsheng Li at Lehigh University. I wrote a program that is used for tracking filamentous structures in images captured by fluorescent microscopy. The program uses an algorithm developed by Li et al [49]. Additional E. Yusuf used this software to track actin structures which is described here. This work has been published in Cytoskeleton [53].

2.1 INTRODUCTION

The assembly of actin and tubulin proteins and their bacterial homologues into long filaments underlies important cellular processes such as cell motility, intracellular transport, and cell division [54–56]. Image analysis of fluorescently-labeled cytoskeletal filaments has provided insights into the function of the cytoskeleton. Examples of such studies include measurements of actin polymerization rates using TIRF microscopy (TIRFM) in vitro [15, 48], shapes of microtubules and actin filaments [57–64], shapes of MreB bundles in E. coli [65, 66], spatial distribution of actin stress fibers [67–69], and network morphology and distribution of intermediate filaments [70–72].

Reliably extracting information on the shapes of linear elements that correspond to filaments or bundles involves two image analysis tasks: segmentation (i.e. extracting the centerline of filaments), and tracking (i.e. measuring motion and deformation

over time). A large body of prior work has described algorithms that aid in detection of dynamic linear structures in images.

In two dimensions (2D), semi-automated methods have been used to track actin filament ends for measuring elongation rates [48]. Automated methods exist for tracking the tips of microtubules [73–76]. In [77], the body of a microtubule can be extracted and tracked over frames using tangential constraints. [49, 78] used open active contour models to extract filaments and proposed mechanisms for handling filament intersections.

Related methods have been developed to extract linear and tubular structures in 3D images. Some model-free techniques, such as mathematical morphology [79], matching filters [80], region growth [81], and minimum description length [82] have been used with considerable success. Model-based approaches have broader applications since they are more robust to noise and can conveniently integrate prior knowledge; these include particle filters [83], minimal path [84], level set [[85], and snake-based methods [86, 87].

Several groups have made software that implements segmentation of linear structures freely available. This includes the 3D FIRE (FIbeR Extraction) Matlab code [88], the NeuriteTracer [89] and NeuronJ [90] ImageJ plugins, and more recently, V3D-Neuron [91]. Visualization software aids in simultaneous viewing of the raw image data superimposed on segmented structures [91, 92].

I developed a new open source, software tool that allows segmentation and tracking of filamentous structures in both two and three dimensions. This tool is based on the "Stretching Open Active Contours" algorithm [49]. Active contours, or "snakes," [93] are deformable parametric spline curves. When placed on an image, an active contour deforms "actively" to minimize its associated energy. The total energy consists of an internal energy that makes the active contour smooth by penalizing abrupt changes in direction, and an external energy that represents constraints from the image data. The external energy generates forces that attract the curve toward salient image features. Conventional active contours are closed contours. In this work open curves were used, to segment and track cytoskeletal filaments. The internal energy term remains the same as that in the original work [93]. Observing the appearance of bright ridges at approximately the central line of each filament. Snakes are deformed by two external energy terms: (i) an intensity-based energy term that is the lowest along the central bright ridges of the image, thus generating forces that attract the

open active contour towards the centerline of a filament, and (ii) a stretching energy term that exerts forces at the curve's two ends and stretches the active contour towards the ends of the filament in the image. Thus, these new active contours are called "Stretching Open Active Contours" (SOACs).

The software tool is called JFilament (http://athena.physics.lehigh.edu/jfilament/) and it is an ImageJ (http://rsbweb.nih.gov/ij/) plug-in. JFilament allows simultaneous visualization of 2D, 3D or 4D (3D space + 1 time) images together with graphical curves representing segmented filaments. Users can deform, add, delete, save and load filament curves. The overview flowchart of the JFilament is illustrated in Figure 2.1A. The main page of the JFilament user interface is shown in Figure 2.1B. In addition to SOACs, JFilament includes standard "closed" active contours which can be used for tasks such as segmentation and tracking of cell boundaries.

JFilament can be used to quantify static and dynamics properties of cytoskeletal filaments, such as bending and torsional persistence lengths (l_{p} and l_{τ}, respectively), and elongation rates. First, to validate our analysis, I generated simulated images of filaments with known l_{p} and l_{τ}. JFilament was used successfully to measure these lengths. Then, we applied our methods to two cases involving images from experiments: (i) measurements of persistence length and elongation rate of actin filaments imaged by TIRFM in vitro, and (ii) measurements of bending and torsional properties of fluorescently-labeled actin cables in fission yeast, imaged by confocal microscopy. We report the first measurements of configurational statistics of actin cables in 3D.

2.2 METHODS

2.2.1 Data: static and time-lapsed images

JFilament was designed to be used primarily for analysis of single-color fluorescence microscopy images. Typically these are (i) stacks of 2D images with each frame representing different time (as with epifluorescence or TIRFM images), or (ii) 4D stacks, with each time point represented by a 3D stack. We assume that the 3D stacks consist of equidistant confocal microscopy planes or deconvoluted epifluorescence focal

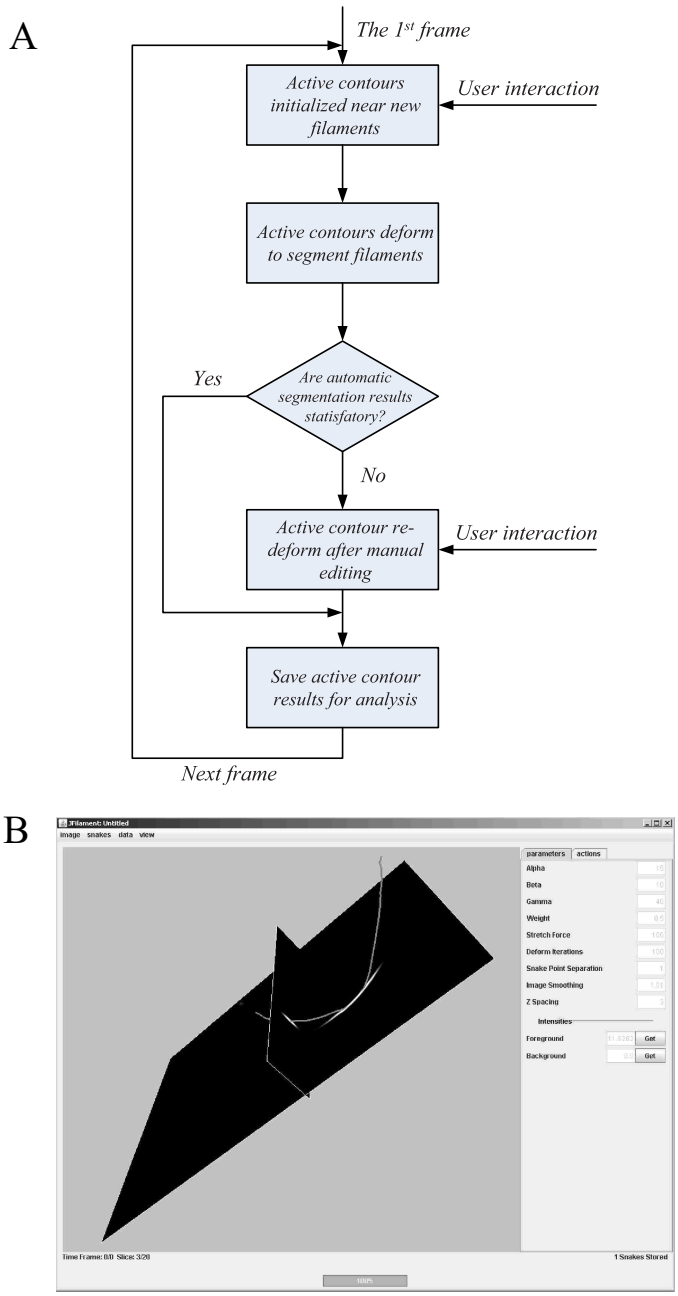

Figure 2.1: (A) The flowchart of the JFilament program. (B) A snapshot of the graphical user interface.

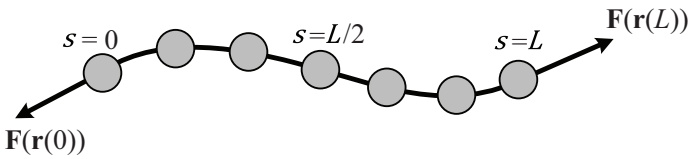

Figure 2.2: Illustration of the open active contour model, where $s \in [0, L]$ measures contour length. Points (dots) are uniformly sampled on the active contour. N is the total number of sampling points on the active contour. Internal energy favors snake shrinking and penalizes abrupt direction change along the active contour. Stretching forces (arrows) are applied at the tips ($\mathbf{r}(0)$ and $\mathbf{r}(L)$) and point outwards along the contour's tangent directions. The forces are intensity-adaptive. If the tip of the active contour is on the filament body then the force points outwards to stretch the active contour; if the tip is in the background, the force points inwards to shrink the contour.

planes. We used JFilament to analyze images of in vitro actin polymerization obtained by TIRFM from [15] and confocal microscopy images of actin cables in fission yeast labeled by GFP-CHD from [94].

2.2.2 Filament segmentation using SOACs

To locate the bright ridges that correspond to filaments, we used SOACs which are open active contours that minimize the sum of an internal and external energy [49, 93]. The internal energy of SOACs favors shorter and straighter active contours. An image-based external energy term attracts them towards the bright ridges at the central lines of filaments and extends them along linear elements depending on the location of the end points.

In 2D, let $\mathbf{r}(s) = (x(s), y(s)), s \in [0, L]$ represent an open curve parametrically (Figure 2.2), where s represents arc length along the open curve, and L is the length of the active contour. In 3D, $\mathbf{r}(s) = (x(s), y(s), z(s))$, where $s \in [0, L]$. The starting and the ending points of the active contour are $s = 0$ and $s = L$ respectively. A set of N discrete sampling points $\mathbf{r}_i = (x_i, y_i), i = 1, \cdots, N$, (or in 3D $\mathbf{r}_i = (x_i, y_i, z_i), i = 1, \cdots, N$), is sampled from the active contour to represent it. The points are sampled at approximately evenly-spaced intervals.

The active-contour-based segmentation works by minimizing the contour's overall

energy, E, which is composed of internal energy, E_{int}, and external energy, E_{ext}, *i.e.*,

$$E = E_{int} + E_{ext}. \tag{2.1}$$

The internal energy term makes the active contour smooth by penalizing abrupt changes in direction. The external energy term represents forces from the image data.

Internal Energy Term. The internal energy term, E_{int}, is defined similar to closed snakes [93]:

$$E_{int} = \int_0^L [\,\alpha|\mathbf{r}_s(s)|^2 + \beta|\mathbf{r}_{ss}(s)|^2]\,ds, \tag{2.2}$$

where $\mathbf{r}_s(s) \equiv d\mathbf{r}/ds$ and $\mathbf{r}_{ss}(s) \equiv d^2\mathbf{r}/ds^2$. The first term, $|\mathbf{r}_s(s)|^2$, penalizes stretching; the second term, $|\mathbf{r}_{ss}(s)|^2$, penalizes bending.

External Snake Energy. The external energy, E_{ext}, consists of two terms: an image term, E_{img}, and a stretching term, E_{str}:

$$E_{ext} = k \int_0^L [\,E_{img}(\mathbf{r}(s)) + k_{str} \cdot E_{str}(\mathbf{r}(s))]\,ds, \tag{2.3}$$

where k is a constant that balances the internal and external energy contributions, and k_{str} is a constant that balances the two external energy terms, which are defined below.

We use a Gaussian-filtered image, $E_{img} = G_\lambda * I$, as the image term, where G_λ is the Gaussian smoothing kernel, I denotes the original image, and * denotes the 2D or 3D filtering operator [95]. The degree of smoothing can be adjusted in JFilament by changing parameter λ. This term is different from the gradient magnitude term $|\nabla G_\lambda * I|^2$ commonly used in conventional segmentation methods [93, 96]. As shown in Figure 2.3, the gradient vectors corresponding to ∇E_{img} point toward the center of filaments. Therefore, our image term has the desired property of attracting the active contour towards the central bright ridge of the filament.

The gradient vectors of the image term, ∇E_{img}, cannot attract the tips of the active contour to grow along the filament body. In order to give an active contour the ability to stretch along a filament body, stretching forces are added to tips of the active contour ($s = 0$ and $s = L$). The tip stretching forces point outwards along the tangent direction of the active contour as shown in Figure 2.2. The direction is $-\mathbf{t}(s)$ if $s = 0$ and $\mathbf{t}(s)$ if $s = L$, where $\mathbf{t}(s) \equiv -\frac{\mathbf{r}_s(s)}{|\mathbf{r}_s(s)|}$. The magnitude of the stretching force is given by:

$$F(\mathbf{r}(s)) = (I(\mathbf{r}(s)) - I_{mean})/(I_f - I_b), \tag{2.4}$$

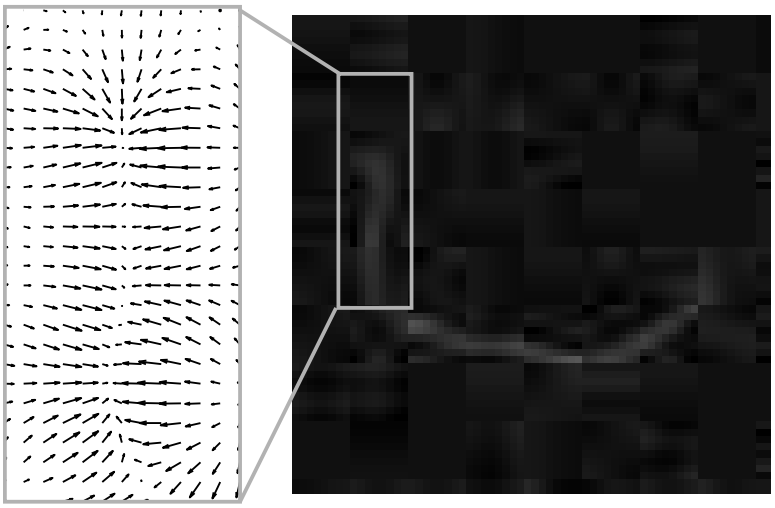

Figure 2.3: TIRFM image of a single actin filament and illustration of the gradient field of our image term, $E_{img} = G_\lambda * I$. The gradient vectors point toward the center of the filament. Therefore, the image term attracts the active contour toward the central line of the filament.

where $I(\mathbf{r}(s))$ denotes the pixel intensity value covered by a certain point $\mathbf{r}(s)$ on the active contour, I_f denotes the mean foreground (i.e. filament) intensity, I_b denotes the mean background intensity, and I_{mean} denotes the average intensity. Parameters, I_f, I_b, I_{mean}, are constants and they are estimated using foreground and background training samples before segmentation. When the intensity at the snake tip is greater than I_{mean} the force will stretch the snake. If the tip is located at a region of lower intensity than I_{mean}, the force causes the active contour to shrink. Given the stretching force definition, we have the gradient field of the stretching energy term as:

$$\nabla E_{str}(\mathbf{r}(s)) = \begin{cases} -F(\mathbf{r}(s))\ \mathbf{t}(s) & s = 0, \\ F(\mathbf{r}(s))\ \mathbf{t}(s) & s = L, \\ 0 & \text{otherwise.} \end{cases} \tag{2.5}$$

Active Contour Deformation. An open active contour deforms and stretches under the influence of forces generated by the above internal and external energy terms. Similarly to [93], the energy function of our new SOAC model is minimized using the Euler method. Since the active contour is represented by a set of discrete points, its overall energy E can be approximated by a sum of energies at these points:

$$\tilde{E} = \sum_{i=1}^{N} \tilde{E}_{int}(i) + \tilde{E}_{ext}(i), \tag{2.6}$$

where $\tilde{E}_{int}(i)$ and $\tilde{E}_{ext}(i)$ denote the internal and external energy at the ith point of the active contour, respectively. The derivatives of $\tilde{E}_{int}(i)$ and $\tilde{E}_{ext}(i)$ can be calculated with finite differences in 2D or 3D. Euler's method is used to derive the dynamics of the active contour. Therefore we minimize the energy function (2.6) by iteratively solving for the coordinates of all points and following the model evolution equations:

$$\mathbf{x}_n = (\mathbf{A} + \gamma\mathbf{I})^{-1}(\gamma\mathbf{x}_{n-1} - \partial\tilde{E}_{ext}(\mathbf{x}_{n-1}, \mathbf{y}_{n-1})/\partial x), \tag{2.7}$$

$$\mathbf{y}_n = (\mathbf{A} + \gamma\mathbf{I})^{-1}(\gamma\mathbf{y}_{n-1} - \partial\tilde{E}_{ext}(\mathbf{x}_{n-1}, \mathbf{y}_{n-1})/\partial y), \tag{2.8}$$

in 2D, and,

$$\mathbf{x}_n = (\mathbf{A} + \gamma\mathbf{I})^{-1}(\gamma\mathbf{x}_{n-1} - \partial\tilde{E}_{ext}(\mathbf{x}_{n-1}, \mathbf{y}_{n-1}, \mathbf{z}_{n-1})/\partial x), \tag{2.9}$$

$$\mathbf{y}_n = (\mathbf{A} + \gamma\mathbf{I})^{-1}(\gamma\mathbf{y}_{n-1} - \partial\tilde{E}_{ext}(\mathbf{x}_{n-1}, \mathbf{y}_{n-1}, \mathbf{z}_{n-1})/\partial y), \tag{2.10}$$

$$\mathbf{z}_n = (\mathbf{A} + \gamma\mathbf{I})^{-1}(\gamma\mathbf{z}_{n-1} - \partial\tilde{E}_{ext}(\mathbf{x}_{n-1}, \mathbf{y}_{n-1}, \mathbf{z}_{n-1})/\partial z). \tag{2.11}$$

in 3D. In the equations, $\mathbf{A}$ is a strictly penta-diagonal banded matrix created based on α and β [Equation (2.2)] and encodes the derivatives of internal energy for every point. $\mathbf{I}$ is the identity matrix, $\mathbf{x}$, $\mathbf{y}$ and $\mathbf{z}$ are the vectors representing the sets of x, y and z coordinates, γ is the step size in Euler's method, and the subscript n denotes the iteration number.

Using the above optimization method, an open active contour can efficiently deform to desired filament central line locations. During its deformation, the active contour is re-sampled every few iterations, maintaining the distance between adjacent sampling points at a fixed interval Δs_{snake}. Thus as the active contour grows longer, the number of sampling points increases, enabling the active contour to elongate. An example of the deformation process of our active contour model is shown in Figure 2.4A. Note that although the initialization is far away from the actual filament location (Figure 2.4A(i)), the active contour is able to correctly recover the filament central ridges (Figure 2.4A(iv)). In JFilament, the user is able to pick the desired number of iterations that are sufficient to ensure convergence.

User Interaction and Manual Editing. I have included manual controls that increase throughput and segmentation accuracy. In addition to initialization,

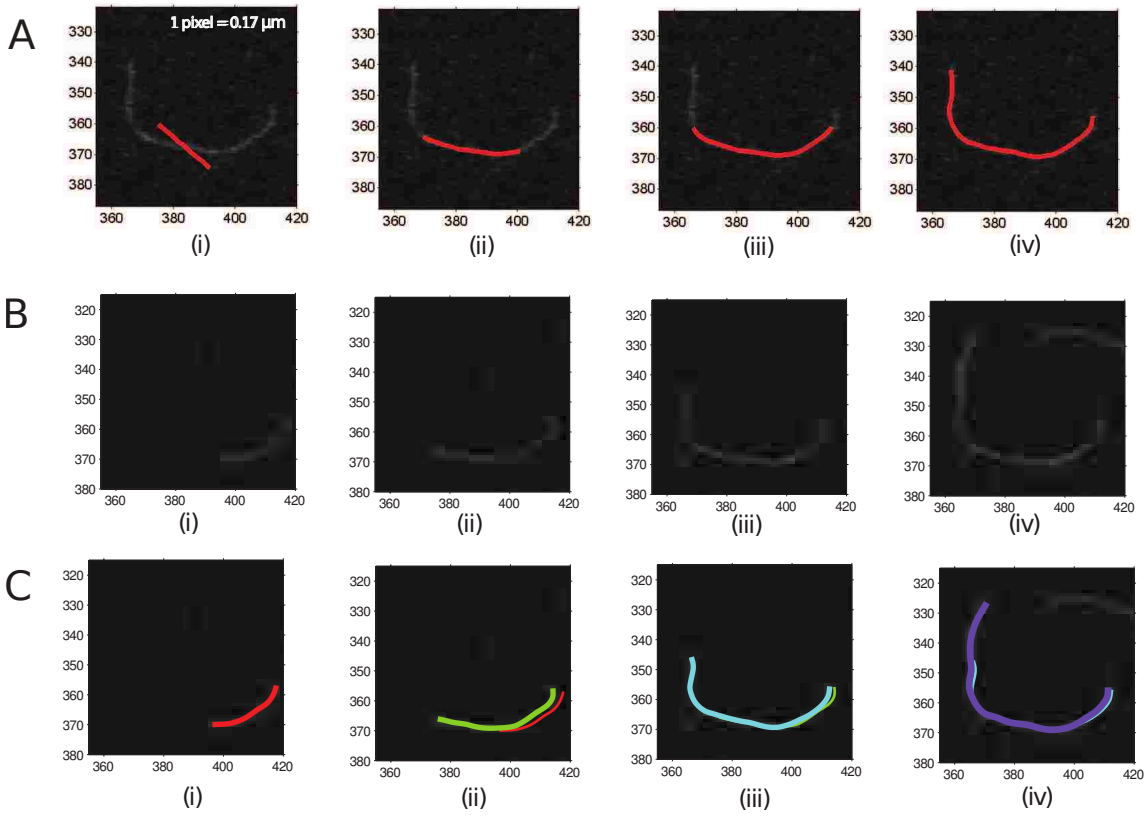

Figure 2.4: Examples of segmentation and tracking of linear structures in 2D. Units are in pixels. (A) Examples of segmentation of an actin filament in a TIRFM image. (i) Initialization of the active contour away from the central line of the filament. (ii)-(iv) The active contour after 20, 40 and 80 iterations of deformation. (B) Images of actin filament polymerization over time using TIRFM. Panels (i)-(iv) correspond to frames 1, 4, 9 and 13. The growth occurs primarily at the barbed end. (C) Illustration of tracking filament growth in panel B using SOACs. Red, green, cyan, and purple curves show SOACs for frames 1, 4, 9 and 13. Frame drift and filament shape changes can be observed; SOACs can adapt to these changes.

the ends of active contours can also be trimmed or stretched and the middle of filaments can be cropped. These simple modifications enable more accurate results by allowing the user to solve the difficulties caused by intersections or variations in intensity that are hard to predict and automate. The user can define 3D points by clicking on cross-section planes.

2.2.3 Filament tracking using SOACs

An active contour can be added and initialized manually at any time point k of a 2D or 3D image sequence. The converged snake of the k^{th} time point is used to initialize the active contour for time point $k+1$. Thus, the active contour can adapt by growing or shrinking, following the growth or shrinkage of the filament in the image over time. An example is shown in Figures 2.4B and 2.4C where the red curve denotes the active contour computed based on a filament in the first frame. The green curve represents the active contour computed for the same filament in the fourth frame. Image sequences may often show drift, i.e. translation, between contiguous frames [48]. Our algorithm is robust to mild frame drift and filament shape changes since the snake is allowed to re-equilibrate along the shifted images. An example of this is shown in Figure 2.4C.

2.2.4 Visualization

Visualization and user interactions in 3D are more challenging than those in 2D. I used Java3D for simultaneous visualization of 3D images and segmentation results represented by active contours. Figure 2.5 shows an example. The active contour, representing the segmented filament is shown on top of a 3D volume view (panel 2.5(i)). Another window shows the position of the active contour with respect to cross sections of the image with the yz, zx, and xy planes; the three planes can be moved along the x, y, and z axes (panel 2.5(ii)). The visualization platform supports rendering of 4D images.

2.2.5 Curve properties

The parametric equation of a 3D snake curve, $\mathbf{r}(s)$, can be used to evaluate the set of three Frenet–Serret orthonormal vectors (see Fig. 2.6), namely the tangent ($\mathbf{t}$), normal ($\mathbf{n}$), and binormal ($\mathbf{b}$) vectors at position s [97]:

$$\mathbf{t} = \frac{d\mathbf{r}}{ds} \tag{2.12}$$

$$\mathbf{n} = \frac{1}{|d\mathbf{t}/ds|}\frac{d\mathbf{t}}{ds} \tag{2.13}$$

$$\mathbf{b} = \mathbf{t} \times \mathbf{n}. \tag{2.14}$$

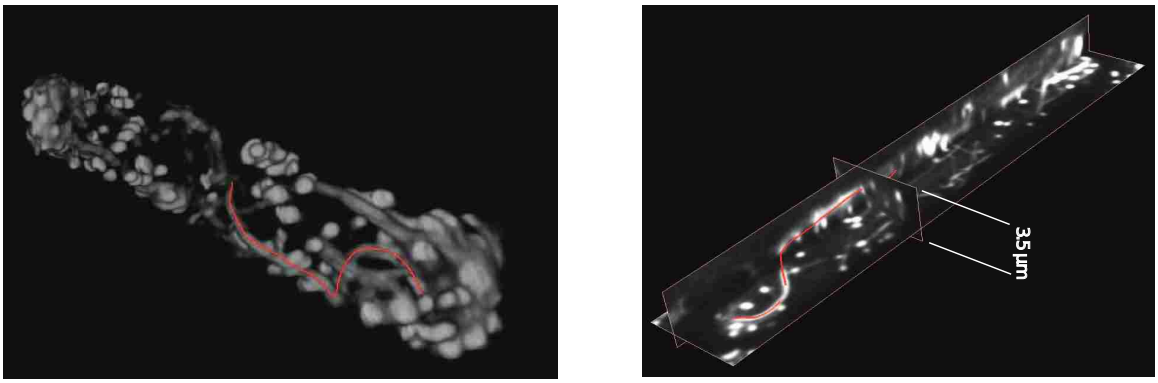

Figure 2.5: Examples of segmentation and tracking of linear structures in 3D. Illustration of 3D views together with filament segmentation results. The images show a fission yeast *cdc25-22* cell expressing GFP-CHD that marks actin cables and actin patches [94]. (i) 3D volume view and active contour of a segmented actin cable. (ii) Image of an active contour together with x, y and z cross-sections of the image.

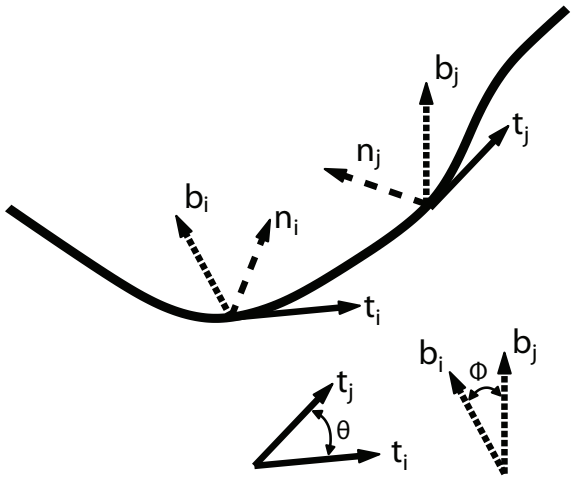

Figure 2.6: A cartoon showing a filament and sets of Frenet-Serret orthonormal vectors (tangent, $\mathbf{t}$; normal, $\mathbf{n}$; binormal $\mathbf{b}$; see Equation (2.14)) at points i and j along the filament. The vector drawings at the bottom right show the angle between tangent vectors and the angle between binormal vectors at points i and j, respectively. Averaging over such angles is used in the calculation of the tangent and binormal correlation functions.

The curvature, κ, and torsion, τ, are determined by the rates of change of the tangent vector and binormal vector with respect to the arc length:

$$\kappa = \left|\frac{d\mathbf{t}}{ds}\right|, \qquad \tau = \left|\frac{d\mathbf{b}}{ds}\right|. \tag{2.15}$$

Curvature represents the rate at which the curve deviates from a straight line on a plane. Torsion represents the rate at which the curve goes out of a plane. A 2D curve has zero torsion (constant binormal vector).

The shapes of snakes extracted from the image can be used to describe the statistical properties of an ensemble of curves that represent filaments or bundles. Such quantities include the probability distributions of curvature and torsion. Other statistical quantities are the tangent and binormal correlations. The tangent correlation function is defined as the ensemble average of the product of tangent vectors separated by a distance Δs:

$$\langle \cos\theta(\Delta s)\rangle = \langle \mathbf{t}(s+\Delta s)\cdot\mathbf{t}(s)\rangle. \tag{2.16}$$

Here, $\langle\rangle$ represents the average over all filaments and over all s along each filament. Similarly, the binormal correlation function is defined as the ensemble average of the product between binormal vectors separated by a distance Δs:

$$\langle \cos\phi(\Delta s)\rangle = \langle \mathbf{b}(s+\Delta s)\cdot\mathbf{b}(s)\rangle. \tag{2.17}$$

The tangent correlation function measures how fast a curve changes orientation while the binormal correlation function measures how fast the curve goes out of a plane.

2.2.6 Simulated semiflexible filaments

Filament Model. For testing purposes, I constructed simulated images of equilibrium semiflexible polymers (worm-like chains, "WLCs") in 2D and 3D described by the following Hamiltonian:

$$\begin{aligned} H &= H_{\text{bending}} + H_{\text{torsion}} \\ &= \frac{b}{2}\int ds\ \left[\kappa(s)\right]^2 + \frac{b_\tau}{2}\int ds\ \left[\tau(s)\right]^2, \end{aligned} \tag{2.18}$$

where b is the bending rigidity and b_τ is the torsional rigidity. The last term representing torsion is absent in 2D. In 3D, this model represents a chain with uniform bending and torsional rigidity but no coupling between bending and torsion. In general, the

energetics of biopolymers involve coupled bending, torsion and twist [98]. Equation (2.18) does not include filament twist which is a property that is not captured by SOACs. Even though H is not the most general Hamiltonian to describe WLCs, it is useful as a model for validation since its equilibrium properties are known and easy to simulate.

In the model of Equation (2.18), the tangent correlation function decays exponentially and is given by [99]

$$\langle \mathbf{t}(s+\Delta s)\cdot\mathbf{t}(s)\rangle = \exp\left\{-\frac{(d-1)\Delta s}{2l_p}\right\}, \tag{2.19}$$

where d is dimensionality and $l_p = b/k_BT$ is the persistence length. Similarly, the binormal correlation function is given by [100]

$$\langle \mathbf{b}(s+\Delta s)\cdot\mathbf{b}(s)\rangle = \exp\left\{-\frac{\Delta s}{2l_\tau}\right\}, \tag{2.20}$$

where $l_\tau = b_\tau/k_BT$ is the torsional persistence length.

The curvature distribution $P(\kappa)$, the probability density for observing a value of curvature between κ and $\kappa + d\kappa$, depends on the dimension [101]:

$$P_{\mathrm{2D}}(\kappa) = \sqrt{\frac{2l_p\Delta s_c}{\pi}}\exp\left\{-l_p\Delta s_c\kappa^2/2\right\}, \quad \mathrm{2D} \tag{2.21}$$

$$P_{\mathrm{3D}}(\kappa) = l_p\Delta s_c\ \kappa\exp\left\{-l_p\Delta s_c\kappa^2/2\right\}, \qquad \mathrm{3D} \tag{2.22}$$

where Δs_c is the length between sampling points along the curve that are used to calculate the curvature. In the model of Equation (2.18) where there is no coupling between bending and torsion, the torsion is distributed as $\exp\{-H_{\mathrm{torsion}}/k_BT\}$. Thus, the probability density for obtaining a value of torsion between τ and $\tau + d\tau$ is

$$P(\tau) = \sqrt{\frac{2l_\tau\Delta s_c}{\pi}}\exp\left\{-l_\tau\Delta s_c\tau^2/2\right\}. \tag{2.23}$$

In addition to using correlation functions and curvature/torsion distributions, the properties of semiflexible filaments can also be studied by Fourier analysis. For a 2D curve, the amplitude of the n^{th} Fourier mode is $a_n \equiv \sqrt{2/L}\int_0^L ds\,\theta(s)\cos(n\pi s/L)$, where $\theta(s)$ is the tangent angle at position s. When a 2D curve representing an equilibrium semiflexible polymer is measured with mean square point localization error ϵ^2, the mean square Fourier amplitudes satisfy[102]:

$$\langle a_n^2\rangle = \frac{1}{l_p}\left(\frac{L}{n\pi}\right)^2 + \frac{4\epsilon^2}{L}\left[1+(N-1)\sin\frac{n\pi}{2N}\right], \tag{2.24}$$

where N is the number of sample points along the curve. The persistence length l_p can be evaluated by fitting to Equation (2.24).

Generation of Images of Filaments. Trajectories of 2D semiflexible filaments were generated using a walk of constant step size δ. An angle θ between the displacement vectors of successive steps was chosen from a Gaussian distribution centered at $\theta = 0$ and variance σ_θ. The variance and the step size determine the persistence length of the filament. Expanding Equations (2.16) and (2.19) for small θ and Δs, respectively, one has $1 - \langle\theta^2\rangle/2 \simeq 1 - \delta/2l_p$. Thus, the persistence length is [101]:

$$l_p = \delta/\sigma_\theta^2. \tag{2.25}$$

The statistics of the resulting angular distributions are identical to those of a 2D worm-like chain down to the level of a single step of the walk. Images were generated by convoluting the trajectory of the walk with a Gaussian kernel.

Simulated images of filaments in 3D were generated similarly to 2D. The angle θ between successive displacement vectors was drawn from the distribution $\sim \theta \exp\left(-\theta^2/2\sigma_\theta^2\right)$ [101], with θ positive or negative. The torsional angle ϕ describing the rotation of the plane defined by two successive steps was chosen from a Gaussian distribution centered at $\phi = 0$ with variance σ_ϕ. Expanding Equations (2.16) and (2.19), one has $1 - \langle\theta^2\rangle/2 \simeq 1 - \delta/l_p$. Using $\langle\theta^2\rangle = 2\sigma_\theta^2$, we find:

$$l_p = \delta/\sigma_\theta^2; \quad l_\tau = \delta/\sigma_\phi^2. \tag{2.26}$$

The second of Equation (2.26) follows similarly from Equations (2.17) and (2.20). The generated trajectories obey the statistics of Equation (2.18) down to a single step of the walk. Images were generated by convoluting the trajectory of the walk with a Gaussian which is 3 times wider along the direction in between z-slices, mimicking an experimental point spread function (PSF) of a confocal microscope.

2.3 RESULTS

In this section we demonstrate how JFilament can be used to quantify static and dynamics properties of cytoskeletal filaments. We start by validating our analysis using simulated images of semiflexible polymers of known properties.

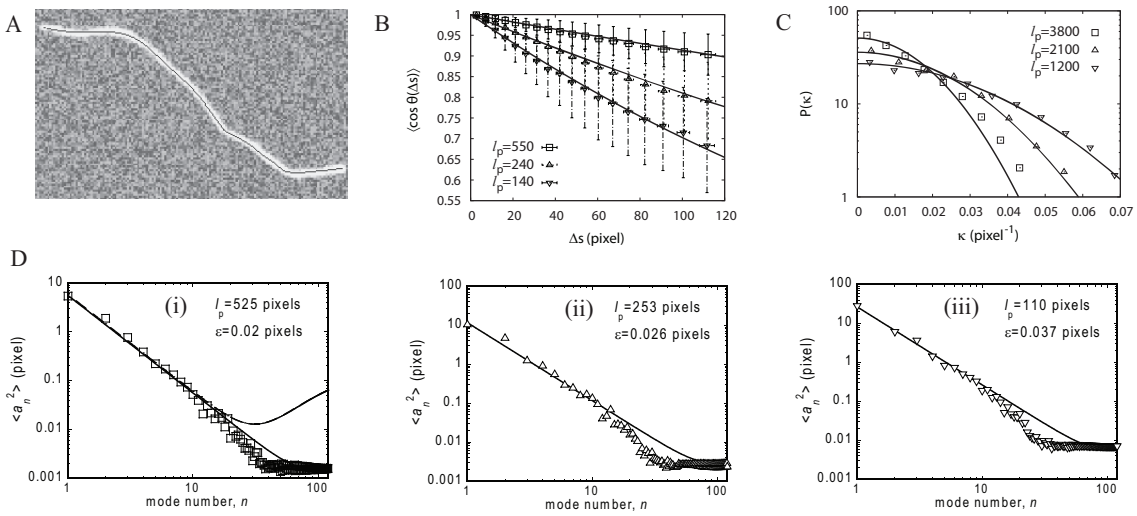

Figure 2.7: Analysis on 2D simulated filaments with known persistence lengths (l_p = 500, 222, and 125 pixels) and total length L=170 pixels. The coarse-graining length is $\Delta s_c = \Delta s_{\text{snake}} = 1$ pixel and 40 filaments were used. (A) Typical image with $l_p = 125$ pixels. (B) Plot of tangent correlations and fits to a single exponential. Error bars indicate standard deviation of individual measurements. The values of the extracted persistence length are shown on the panel. These values are close to the intrinsic persistence lengths of the WLCs. (C) Plot of curvature distribution and Gaussian fits [cf. Equation (2.21)]. The measured persistence lengths shown on the plot are much longer than the intrinsic persistence length of the WLCs (see main text for discussion). (D) Plots of mean square amplitude of Fourier modes versus mode number for intrinsic persistence length 500, 222, and 125 in panels (i)-(iii), respectively. Continuous lines are fits to Equation (2.24); the corresponding values of l_p and ϵ are shown in the panels. The dashed line in panel (i) shows the results of Equation (2.24) using $l_p = 500$ and $\epsilon = 0.14$ (see main text).

2.3.1 Validation using simulated 2D semiflexible polymers

I generated simulated images of 2D worm-like chains using walks of step size $\delta = 1/20$ pixel and total length 170 pixels, as described in the Methods section. The persistence length of these chains was varied by changing the parameter σ_θ, see Equation (2.25). The resulting trajectories were convoluted with a 2D Gaussian of variance 1 pixel to generate images such as those in Figure 2.7A.

We used JFilament to generate active contours that adapted to the bright ridges of the simulated image. The distance between successive points on the snake was set to $\Delta s_{\text{snake}} = 1$ pixel. The other parameters of the snakes (such as α, β and γ,

	l_p (WLC)	l_p (tangent correlation)	l_p (Fourier)
$\sigma_\theta = 0.01$	500	540	525
$\sigma_\theta = 0.015$	220	240	253
$\sigma_\theta = 0.02$	125	140	110

Table 2.1: Table showing agreement between intrinsic and measured persistence length of simulated 2D worm-like chains (units: pixels). The intrinsic persistence length was varied by changing parameter σ_θ. The measured persistence length was extracted from fits to the tangent correlation function and mean square Fourier amplitudes in Figure 2.7.

see Methods section) were adjusted manually until good agreement was achieved by visual inspection. The parametric curves of the snakes were then used to calculate the tangent correlation function, curvature distribution and amplitudes of Fourier modes (see Figures 2.7B,C,D).

Figure 2.7B shows the tangent correlation function for three different values of the WLC persistence length. After fitting to single exponentials, see Equation (2.19), we were able to obtain estimates of the persistence length that were within 10% of the value of the intrinsic persistence length of the WLCs. Fits to Fourier amplitudes in Figure 2.7D, using Equation (2.24), give similar estimates for the persistence length, see Table 2.1.

We found that the curvature distribution can also provide a good estimate of the persistence length, but this requires caution, as discussed in [58]. Figure 2.7C shows the curvature distribution for the same snakes as those used in Figure 2.7B,D. In this panel, a value for the curvature was calculated from each triplet of successive points of the snake; on average, the successive points were separated by distance $\Delta s_c = \Delta s_{\text{snake}}$. The resulting curvature distributions follow Gaussian profiles, as expected from Equation (2.21). However, fitting these curves to Equation (2.21) results in a predicted persistence length which is an order of magnitude higher than the intrinsic persistence length of the WLC.

The problem with the values obtained in Figure 2.7B is that they reflect the bending stiffness of the active contour, in addition to that of the WLC. Because of our choice of snake parameters, locally, i.e. on scales of order a pixel, the snake appears stiffer than the WLC. This behavior is also evident in downward trend of $\langle a_n^2 \rangle$ in Fig. 2.7D at mode numbers $n \sim 30$: the data deviate from the expected scaling of slope -2 and lie below the fit of Equation (2.24). This deviation indicates a stiffening

of the snake on short scales. Consistently, the slope of the tangent correlation function at $s = 1$ pixel in Figure 2.7B is somewhat smaller than the slope at $s = 20$, implying larger persistence length at small distances. However, since the relative decay of the tangent correlation over small distances is small, the exponential fit is dominated by the decay of the tangent correlation over distances much longer than a pixel; thus the correct persistence length is recovered by the fit.

It is useful to compare the results of Fig. 2.7D to the method of [60] who used a combination of thresholding and thinning to achieve an accuracy of pixel localization $\epsilon = 0.14$ pixels. The dashed line in Figure 2.7D(i) shows the predicted Fourier amplitudes using $l_p = 500$ (the intrinsic persistence length) and $\epsilon = 0.14$. This noise level in pixel localization causes a plateau of $\langle a_n^2 \rangle$ at $n \approx 20$. The noise plateau for SOACs, by contrast, is reached at $n \approx 50$. Thus SOACs achieve very low noise in pixel localization, $\epsilon = 0.02$ pixels, at the expense of snake stiffening. For the particular example in the figure, both methods would give equally good results for l_p as they are approximately equally accurate for $n < 20$ and exhibit deviations from a line of slope -2 for $n > 20$.

Figure 2.8 shows how a coarse graining analysis can be used to extract the true persistence length of the simulated filaments from the curvature distribution. A cartoon of a contour is depicted in Figure 2.8A. The distance between the dots in Figure 2.8A is the distance between sampling points of the contour in JFilament, $\Delta s_{\mathrm{snake}}$. For $\Delta s_{\mathrm{c}} = \Delta s_{\mathrm{snake}}$ the curvature at the i^{th} site is calculated from three successive points along the snake $i-1, i$, and $i+1$, as in Figure 2.7C. Figure 2.8A, illustrates how the curvature at the k^{th} site can be obtained from points $k-1, k$, and $k+1$. In this particular example the coarse graining length is $\Delta s_{\mathrm{c}} = 2\Delta s_{\mathrm{snake}}$.

We found that the value of the persistence length extracted from the curvature distribution depends strongly on the value of Δs_{c}. Figure 2.8C shows that with increasing Δs_{c}, the distribution narrows, as expected from Equation (2.21). In addition to this trend, the value of the measured persistence length after fitting changes as well. Figure 2.8D shows that the extracted l_{p} decreases with increasing Δs_c and approaches the intrinsic value of l_{p} around $\Delta s_c = 20$ pixels. Thus, as Δs_c becomes larger, the curvature distribution becomes independent of the local snake rigidity and eventually measures the true persistence length of the filament in the image.

Since the tangent correlation function already describes correlations over many scales, its shape is less sensitive to our choice of Δs_c, see Figure 2.8B and D. For

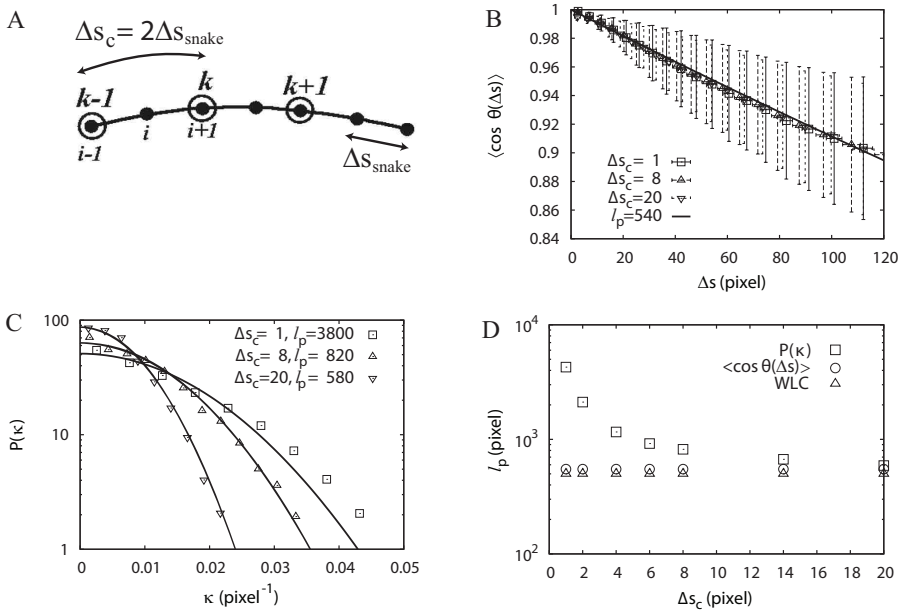

Figure 2.8: Coarse graining analysis of curvature reveals the true rigidity of WLCs. The calculations use WLCs with $l_p = 500$ pixels ($n = 40$ filaments). (A) Schematic of coarse graining. The black dots represent the sampling points of the active contour that are separated by Δs_{snake}. Without coarse-graining, the coordinates of $i-1, i$, and $i+1$ are used to calculate the tangent vectors and curvature. With coarse-graining, $\Delta s_c = 2$ in this example, sites $k-1, k$, and $k+1$ are used instead. (B) The tangent correlations are weakly dependent on coarse graining length Δs_c and follow single exponential decay (solid line). Error bars indicate standard deviation of individual measurements. (C) Plot of curvature distributions for different coarse-graining lengths Δs_c. The widths depend on Δs_c, as expected from Equation (2.21). In addition to this change, the value of the extracted persistence lengths (shown in the panel) change with Δs_c as well. (D) Measured persistence lengths as a function of Δs_c calculated from the tangent correlation (circles) and curvature distribution (squares) as compared to the intrinsic persistence length of WLCs (triangles). The accuracy of estimates of persistence length using the curvature distribution increases with increasing Δs_c.

all Δs_c, the tangent correlation function can be fit with exponentials of identical persistence length.

	l_p (pixel)	l_τ (pixel)
WLC	500	500
tangent correlation	530	-
curvature distribution	540	-
binormal correlation	-	510
torsion distribution	-	540

Table 2.2: The bending (l_p) and torsional (l_τ) persistence lengths as extracted from the analysis (see Figure 2.9) agree well with those of the simulated WLC.

2.3.2 Validation using simulated 3D semiflexible polymers

We tested JFilament's performance in 3D using simulated images of WLCs, similarly to 2D. The simulated WLCs had $l_\mathrm{p} = l_\tau = 500$ pixels, obtained using $\sigma_\theta = \sigma_\phi = 0.01$ and step size $\delta = 1/20$ pixels as described in Methods [see Equation (2.26)]. 3D image stacks were generated by convoluting the trajectories of the WLCs with a Gaussian distribution of variance 1 and 3 pixels in the xy and z directions, respectively (see Figure 2.9A). This mimics the anisotropy in the PSF in confocal microscopy experiments [103]. The spacing between images along the z direction was 1 x y pixel. JFilament was subsequently used to trace WLCs using a sampling interval $\Delta s_\mathrm{snake} = 1$ pixel. We then used the shapes of the snakes to calculate the tangent correlation, curvature distribution, binormal correlation, and torsion distributions in Figure 2.9.

We found that, similarly to the 2D case, an exponential fit to the tangent correlation function (Figure 2.9B) provides a good estimate of the bending persistence length. Our estimate of $l_\mathrm{p} = 530$ pixels from the fit is close to the actual value (see Table 2.2). This value was very weakly dependent on coarse-graining. Coarse-graining is however required in order to extract the correct l_p from the curvature distribution, similarly to 2D. We found that $\Delta s_c = 20$ pixels is adequate: using this value in Figure 2.9C, a fit to Equation (2.22) gives $l_\mathrm{p} = 540$ pixels, close to the actual value.

The calculated binormal correlation function and the torsion distribution, Figures 2.9D and 2.9E, agree with the expectations of the WLC model [cf., Eqs. 2.20 and 2.23. The measured torsional persistence lengths, $l_\tau = 510$ pixels (binormal) and $l_\tau = 540$ pixels (torsion), are within 10% of the intrinsic value (see Table 2.2). We found that the binormal correlation function is not sensitive to the choice of coarse-graining length Δs_c while for torsion distribution, $\Delta s_c = 20$ pixels is sufficient to obtain a good fit to a Gaussian profile and to produce the correct torsional persistence length.

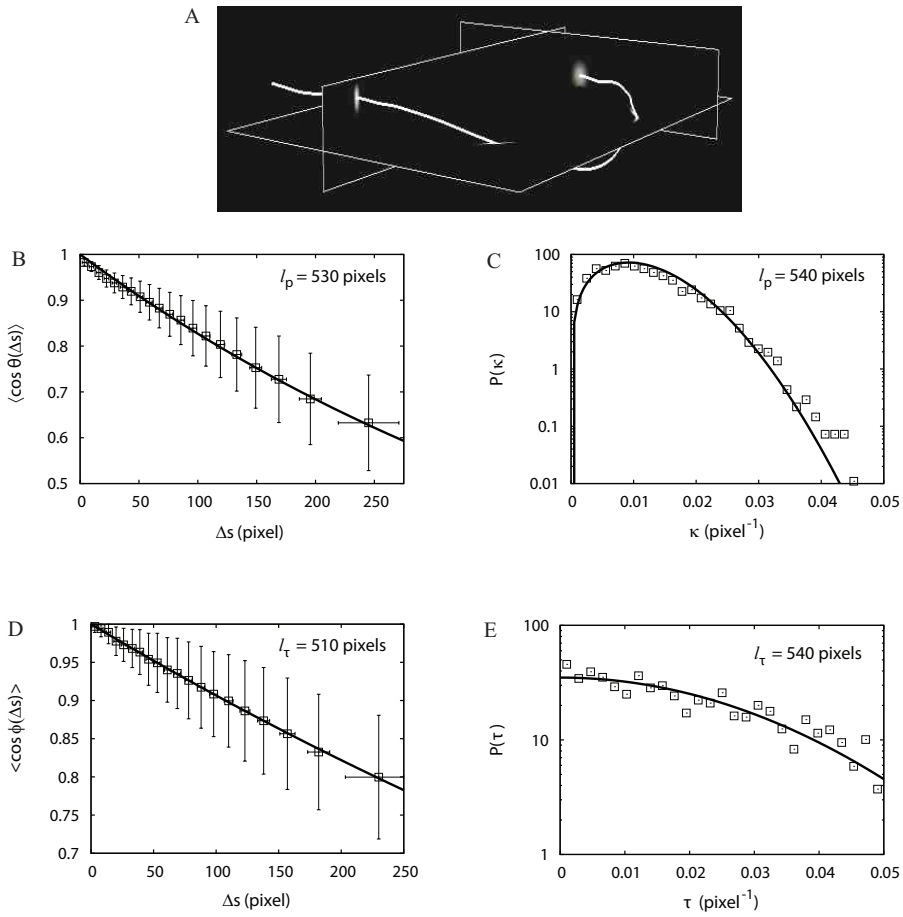

Figure 2.9: Analysis of simulated images of 3D filaments with known bending and torsional persistence lengths ($l_\mathrm{p} = l_\tau$ =500 pixels) demonstrates the validity of SOACs. Measured values from fits are shown in the panels. In all cases, these values are within 10% of the intrinsic values (see also Table 2.2). Coarse-graining length is $\Delta s_c = 20$ pixels and $n = 40$ filaments. Error bars indicate standard deviation of individual measurements. (A) Typical simulated 3D image. (B) The tangent correlation function and exponential fit. (C) Curvature distribution and fit to Equation (2.22). (D) Binormal correlation and exponential fit. (E) Torsion distribution and Gaussian fit.

In conclusion, similarly to the 2D case, the persistence lengths extracted by curvature and torsion distributions are influenced by local properties such as the rigidity of the active contours. This dependence is eliminated by coarse graining. In contrast, the tangent and binormal correlation functions are less sensitive to the degree of coarse graining.

2.3.3 Measurements of actin filaments in a TIRFM elongation assay

Having validated our methods using simulated 2D and 3D polymers, we now demonstrate the application of JFilament to experimental data. First we analyze the conformations of purified actin in a TIRFM polymerization experiment of 4μM Mg-ADP-actin in the presence of 15mM inorganic phosphate P_i [15].

Selecting filaments from a single frame in the movie, we calculated the tangent correlation function and curvature distribution, after coarse graining to $\Delta s_c = 8$ pixels (see Figure 2.10). We found that the tangent correlation function fits to a single exponential with a persistence length $l_p = 9\mu$m. The exponential shape is consistent with the statistics of equilibrium 2D semiflexible polymers, even though these filaments are not in strict equilibrium as they grow over time and attach to pivot points on the glass surface. The curvature distribution is well approximated byplat a Gaussian, also consistent with equilibrium statistics. A fit to the equilibrium WLC model [Equation (2.21)] leads to $l_p = 10\mu$m. Both these values of l_p are consistent with prior measurements of persistence length of native actin filaments (without phalloidin) [104, 105]. The value of l_p does not change appreciably upon further coarse-graining, indicating that it is not fd by image noise or snake stiffness.

Since active contours stretch, JFilament can also be used to measure filament elongation rates. We calculated the rate using $j = \langle L(t + \Delta t) - L(t)\rangle / \Delta t$, where L is length and $\langle\rangle$ denotes averaging over different times and different filaments. We found $j = 11 \pm 0.5$ monomers/s, consistent with the value reported in [15]. Since the pointed end polymerizes much slower than the barbed end, this rate is mostly due to the barbed end.

2.3.4 Measurements of actin cables in fission yeast imaged by confocal microscopy

As a second example of an application to experiments, we used images of fission yeast expressing Calponin Homology Domain fused to GFP (GFP-CHD) obtained by Jian-Qiu Wu in [94], see Figure 2.5. GFP-CHD binds to the sides of actin filaments and labels actin cables and actin patches. We used confocal microscopy images of strain JW1311 obtained with 45 nm/pixel along the xy plane and 125 nm between z slices. These cells are longer than normal fission yeast because they are *cdc25-22*

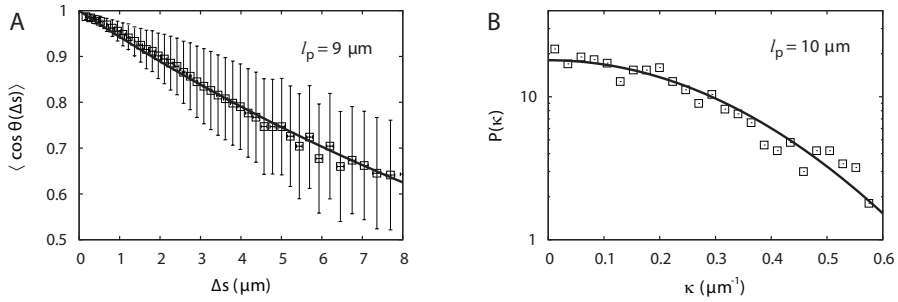

Figure 2.10: Analysis of actin filaments in a frame of a TIRFM movie from [15] (4 μM ADP-P_i-actin with 15 mM P_i), see Fig. 4A. Images of 30% Alexa green-labeled actin were captured by an ORCA-ER camera (Hamamatsu Corporation, Hamamatsu, Japan). The exposure time was 500ms and the pixel size 0.17 μm. We used $\Delta s_c = 1.3\mu$m, n=20 filaments. (A) Plot of tangent correlation function. Error bars indicate standard deviation of individual measurements. A fit to a single exponential gives persistence length 9μm. (B) Plot of curvature distribution. A Gaussian fit gives persistence length 10 μm.

cells arrested in the G2 phase so they keep elongating without entering mitosis.

We analyzed cables that have a clear trajectory across the cell, as in Figure 2.5. Figure 2.11A shows that the tangent correlation function can be described by a double exponential with two length scales: $l_1 = 2$ μm and $l_2 = 1$ mm. Thus, while l_1 is less than the persistence length of single actin filaments [104, 105], l_2 is of order the persistence length of microtubules [102]. The curvature distribution in Figure 2.11B changes upon coarse-graining and does not follow a distribution similar to that of Figure 2.9C. For $\Delta s_c = 0.9$ μm, the distribution appears to approach an exponential, $\exp(-\alpha\,\kappa)$, with $\alpha = 0.25$ μm.

Similarly to the tangent correlation function, the fit of the binormal correlation function to a double exponential gives a pair of short and long scales with similar values: $l_1 = 0.5$ μm and $l_2 = 1$ mm (see Figure 2.11C). Here, l_1 is less reliable as a numerical value since it is of order the width of the PSF in the z direction and Δs_c. Similarly to the curvature distribution, the shape of the torsion distribution depends on the degree of coarse-graining, see Figure 2.11D.

The above analysis shows that the conformations of actin cables are richer than those of 3D semiflexible polymers. The small value of l_1 could be due to deformations

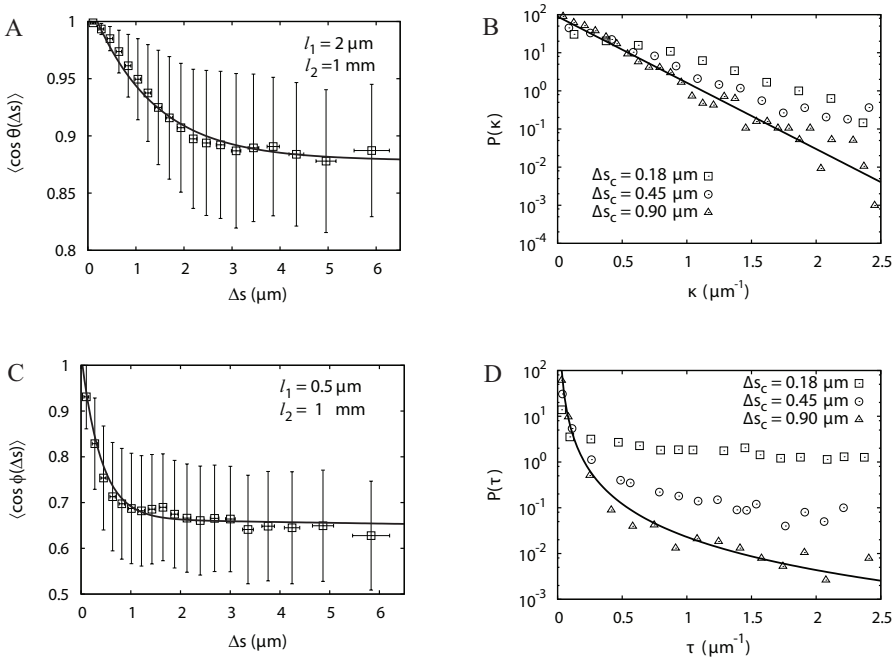

Figure 2.11: Analysis of actin cables in a fission yeast cell expressing GFP-CHD, average of 40 cables (see Figure 2.5 and main text). Error bars indicate standard deviation of individual measurements. (A) The tangent correlation function using $\Delta s_c = 0.9$ μm. Fit to a double exponential (continuous line) leads to length scales $l_1 = 2$ μm and $l_2 = 1$ mm. (B) Plot of the curvature distribution for different Δs_c. (C) Plot of the binormal correlation function using $\Delta s_c = 0.9$ μm. Fit to a double exponential leads to $l_1 = 0.5$ μm and $l_2 = 1$ mm. (D) Plot of the torsion distribution for different Δs_c. A power law fit (exponent -2.4) is shown for $\Delta s_c = 0.9\mu$m.

on short scales such as motor pulling or buckling [59, 62], interaction of cables with patches [106], fixed fluctuations that occur during actin cable assembly at the tips of the cell [61, 107]. The large value of l_2 could reflect the stiffness of the bundles and the fact that the actin cables are confined within a rigid tube, i.e. the whole cell [108]. The existence of different scales generates curvature and torsion distributions whose shape depends on the extent of coarse-graining. These data motivate future work with yeast mutants that will shed light on the origin of the observed statistics.

2.4 DISCUSSION

We presented a tool for segmentation of cytoskeletal filaments in images based on the SOACs method. The software allows both automated segmentation and tracking of the images as well as full manual controls, such as trimming, stretching, and cropping parts of the active contours, to obtain accurate results. Properties such as length changes and curvature can be easily extracted from the coordinates of the active contour.

Compared to other implementations that segment linear structures, the SOACs have the advantage of using parametric curves of fixed topology to represent filaments, and they are particularly good at preserving topology at intersections and growing over faint elements that are otherwise hard to detect. Many previous methods such as point-and-click, skeletonization by thresholding, level-set and MRF-based methods [58, 60, 63, 88, 109, 110] produce pixel-wise segmentation results; the curve has to be reconstructed in a separate step and this may be problematic in noisy images or in images involving complex features. Active contours, however, are continuous curves by construction. They naturally deform and align with the central bridge ridges of filaments, are robust to noise, and can capture dynamical features such as deformation and elongation. User-interaction and the ability to change the properties of active contours through a few basic set of parameter values allows the analysis of images of varying complexity in 2D and 3D. While in its present form our method does not describe network structures, such an extension is possible. Strategies can also be introduced to handle crossed filaments—for instance, in [49], we proposed two strategies, greater tip stiffness and tip "jump", to solve the filament intersection problem using SOACs.

We further showed how the traces of the SOACs can be used to measure the intrinsic properties of semiflexible polymers with high accuracy. We argued that care has to be exerted when analyzing features that rely on accurate measurements at the scale of order one pixel or of order the width of the point spread function. Noise, intrinsic snake stiffness, PSF anisotropy may influence quantities that depend on precise local contour shape. One example was the distribution of curvature: for stiff filaments, the average curvature is small so it can be influenced by these factors. Depending on the particular case, a careful analysis, such as the coarse-graning analysis of Fig. 7, may be required [57, 58, 60, 102]. Similarly, the physical significance of quantities such

as torsional and bending persistence lengths may depend on the system in consideration: bending, torsion and twist are generally coupled. JFilament provides a means to extract quantitiative information in order to examine, for example, correlations between bending and torsion. Such measurements could help clarify the biophysical properties of cytoskeletal filaments and bundles of filaments.

Chapter 3

Tracking of speckle trajectories in fluorescence microscopy: application to actin polymerization and membrane fusion

This chapter describes another software tool I wrote for tracking point-like particles. I originally wrote this tool for tracking speckles (see Fig. 3.5) in XTC Fibroblasts in images collected by Naoki Watanabe and a post doc in his lab, Hiroki Mizuno. This work proved useful for tracking point like features in other systems, and led to a collaboration with Erdem Karatekin and Andrea Gohlke at Yale School of Medicine who performed experiments using supported lipid bilayers. The following contains the algorithms of this software, and results obtained through it's application. This work was published in Biophysical Journal [6].

3.1 INTRODUCTION

Advances in microscopic imaging continues to create unique demands for particle tracking in biological systems [111–114]. Examples of tasks that involve tracking of bright spots include virus trafficking in live cells [115], motion of transmembrane proteins on the cell membrane [116], cell microrheology [114, 117], dynamics and fusion of secretory and synaptic vesicles [118–121], and tracking of cytoskeletal proteins [40, 41, 122, 123].

The field of algorithm development for particle tracking has a rich history. There are three approaches to apply these algorithms to biological systems. Firstly, close collaboration of biologists, computer scientists and physical scientists to develop specialized software [113]. Secondly, many labs resort to commercial software. The latter, however, have the disadvantage that they are expensive, often require additional modules, and need to be modified by the vendor. Finally, a third possibility is to use open-source software tools that may be directly applied, or depending on the flexibility of the program, modified for a specific system.

One of the first freely-available particle tracking tools was developed in IDL [117, 124] to track the positions of colloidal particles. This algorithm involved image restoration followed by detection of particle positions and linking of positions into trajectories. This code has been converted to the MATLAB (The Mathworks, Inc.) and C++ languages and extended in 3D [125, 126]. It has also been adapted in the MATLAB program PolyParticleTracker [127]. GMimPro is a detection and tracking software available as a compiled Windows program [128, 129]. Freely-available MATLAB code for particle tracking further includes u-track [42], MTT [130] and plusTipTracker [131] (optimized for tracking microtubule plus ends). u-track and MTT, developed for tracking dense particle systems, use various criteria for deciding the likelihood of particle merging, starting, stopping and gaps in detection failure. Since the MATLAB platform is not always available, many researchers have contributed tracking algorithms as plugins for the open-source image analysis program ImageJ. Some open-source plugins are MTrack2, Manual Tracking, and Particle Tracker [132]. The latter is based on the MATLAB code and methods developed in [133]. Free ImageJ plugins, available as jar files (compiled code), include MTrackJ [134] and SpotTracker [135].

All tracking algorithms start failing at low signal-to-noise (STN) ratio and at high particle mobility during camera exposure. These challenging situations are common in single molecule studies in live cells [39, 41]. Another challenge occurs when one is interested in a small subset of particles within a heterogeneous population, such as single vesicles that fuse with the plasma membrane or with supported bilayers [118–121, 136]. The challenge is to track only that subset. In all those cases the primary question is whether valid single particle tracks can be obtained at all.

To address the above challenges we developed an open-source particle-tracking tool, Speckle TrackerJ, as an ImageJ plugin [137], with the following two-tier strategy.

First, tracks are obtained with rough positioning accuracy, using user assistance and supervision when needed. The user can control which of the candidate particles to track over time with the aid of tracking models. We designed models that use the expected behavior of particles to improve detection and tracking. A modular construction allows modification and design of new tracking models. In a second step, the positioning accuracy and precision of the existing tracks are improved. This iterative approach is much more efficient than trying to achieve the best tracking performance in a single step in the challenging cases described above. Our method is particularly useful when measuring particle lifetimes (trajectory length) in the presence of noise and blinking where user input is required to distinguish broken trajectories from real appearance and disappearance events.

We demonstrate that Speckle TrackerJ compares well with related software in control synthetic image sequences that cover a range of noise levels and particle mobilities. We then proceed to demonstrate the successful application of our method to four different challenging experimental situations: dynamics of single capping proteins at the leading edge of motile cells, single-molecule actin speckle lifetimes in lamellipodia, release and diffusion of single fluorescent lipids from vesicles upon fusion with supported, planar bilayers, and docking-to-fusion lifetimes of vesicles fusing with planar supported bilayers mediated by *soluble N-ethylmaleimide-sensitive factor attachment protein receptor* (SNARE) proteins. In none of these situations could other existing software be used satisfactorily.

3.2 MATERIALS AND METHODS

3.2.1 Particle representation

Trajectories of particles through time are recorded as speckle tracks. A speckle track records the position of a particle in time. Each point of a track is represented by a speckle mark. Tracks can be created and modified by a user or through computer assisted techniques.

Computer assisted tracking is divided into three steps: Detection of speckle mark candidates; tracking through time to create a speckle track using a model; and refinement of speckle mark positions. These steps can be repeated manually or using batch tracking. At any point during this process the speckle tracks can be modified (see "User Interface" in Supporting Materials).

3.2.2 Detecting particles

We implemented two detection methods. (1) "Locate Speckles," uses a threshold value to create a binary image. A two-pass connected components algorithm is then applied to find speckle mark candidates. (2) "Template Locate," performs the same operation as the "Locate Speckles" method except that it uses existing speckle marks to create a Normalized Cross Correlation (NCC) filtered copy of the image. The NCC template is created by averaging a square region of adjustable size centered at existing speckle marks.

3.2.3 Tracking the tracker

Tracking has been separated into two components: models and the tracker algorithm (see Fig. 3.1). Models modify speckle tracks by adding new marks (some only refine their position). The tracker algorithm applies the selected model successively from frame to frame and records which speckle tracks are being modified.

Before the tracker starts, it initializes the selected model with existing speckle tracks (which tracks are used depends on the model). After initialization, the tracker creates a tracking list, a list of speckle tracks to be updated. The tracking loop begins by passing a speckle track and the current time frame to the model, which then determines how to continue to the track. If the model determines that a track ends, the track is removed from the list. After the model finishes, the tracker checks the tracking list for speckle tracks that overlap. Overlap occurs if two tracks have a speckle mark on the same frame and the distance between those marks is less than a user-adjustable minimum distance parameter. If the tracking list is not empty, the tracker will move to the next frame and start the tracking loop again.

3.2.4 Tracking models

We implemented tracking models that use fixed and adaptable parameters (see Supporting Material and [137]). Adaptable-parameter models "learn" as tracking proceeds.

"Diffusing Spots" is an adaptable-parameter model that adds a new mark to the speckle track in the frame immediately after the last frame that has already been marked. It searches for a new mark within a square region centered at the previous mark. The model is initialized by calculating the average intensity, $< I >$,

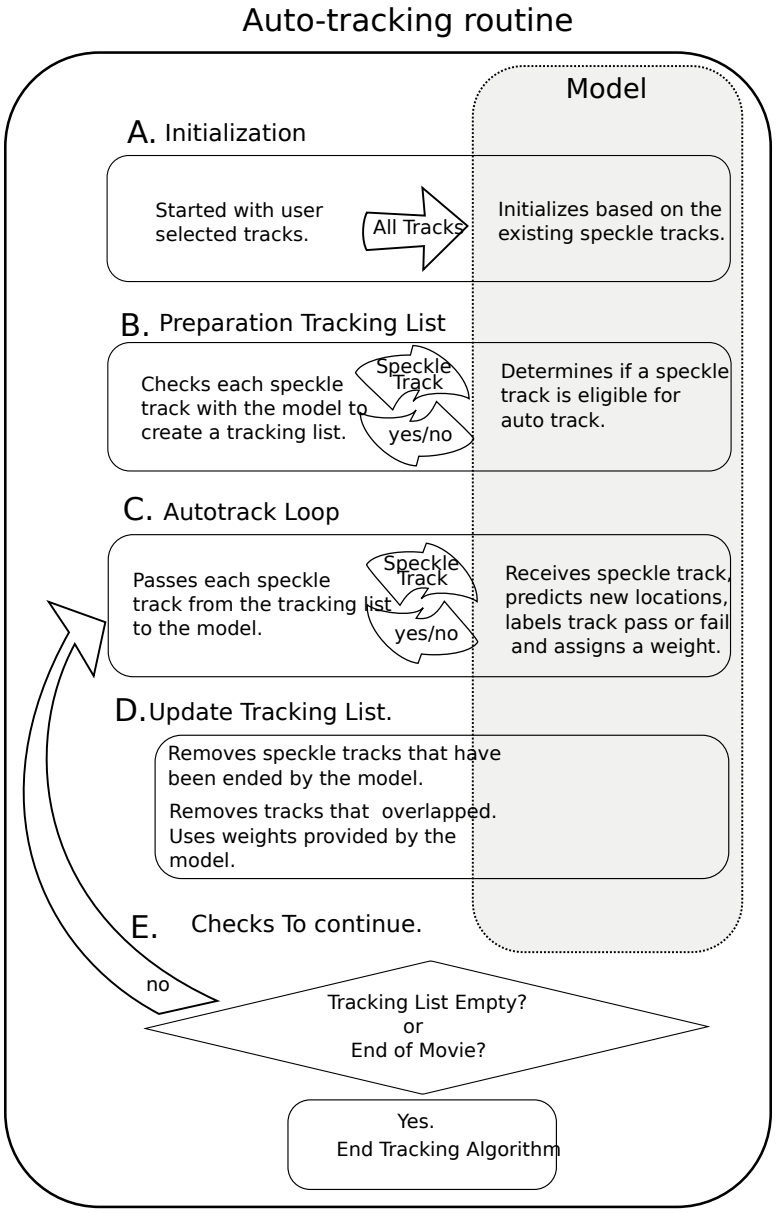

Figure 3.1: Flow chart of automated tracking algorithm. Actions in the grey region are performed by the model and all other actions are performed by the tracking algorithm.

the variance in intensity, $\sigma^2_{\delta I}$, and the variance in frame to frame displacement, σ^2_d, calculated using all speckle marks from either the selected speckle track, if "Auto-Track" was used to start the tracker, or all existing tracks, if Auto-Track All was used. The intensity measurements are made by integrating the pixel intensity over a circle centered at the position of each speckle mark. The radius is a user-adjustable

parameter. To predict the position of the next speckle mark, the model finds all pixels that are local maxima within the square search region. For each candidate location, the intensity, I, change in intensity from the previous frame,δI, and the displacement from the previous frame, d, is measured and used to generate weights:

$$w_i = e^{(I-<I>)/(<I>-I_m)}, w_{\delta I} = e^{-\delta I^2/(2\sigma_\delta^2 I)}, w_d = e^{-d^2/(2\sigma_d^2)}, \tag{3.1}$$

where I_m is the mean value of the intensity in all frames of the movie. If I is greater than $< I >$, w_i is set to one. The weights are summed with user-adjustable factors, f_i, $f_{\delta I}$, f_d, to get a combined weight:

$$w = w_i f_i + w_{\delta I} f_{\delta I} + w_d f_d, f_i + f_{\delta I} + f_d = 1. \tag{3.2}$$

The best candidate is accepted if $w > w_{min}$. If no candidate satisfies this condition, the track stops.

"Diffusing NCC" is similar to Diffusing Spots but it takes into account NCC values. Initialization consists of measuring the average intensity I over a circle and NCC value at every speckle mark position using a square template made from all speckle marks. To find a new candidate location, the model checks the square search region for the location with the maximum NCC value. Then the intensity and NCC value are measured at that location and used in a weighting function

$$w = e^{-(I-<I>)^2/(2\sigma_i^2)} e^{-\alpha(NCC-<NCC>)^2/2\sigma_{NCC}^2} \tag{3.3}$$

where averages and standard deviations are over all existing speckle marks and α is an adjustable parameter. If w is smaller than a threshold w_{min}, the track ends.

"Constant Velocity NCC" model is the same as Diffusing NCC but the search for the best candidate occurs over a square whose center is displaced from the position of the previous speckle mark. This method is useful in cases where particles move with constant velocity.

3.2.5 Refine position

Speckle tracks can be refined to improve the position of existing speckle marks (see Supporting Material). The "Adjustment Model" modifies existing speckle tracks by moving them to the center of intensity. The "Gaussian Fit" model refines the position of speckles with sub-pixel accuracy by fitting a 2D Gaussian to the intensity near a speckle mark.

3.2.6 Experiments

Details of experimental protocols can be found in Supporting Materials. In summary, live cell imaging of XTC cells was carried out as described [39]. Fluorescent speckle microscopy was carried out by observing cells expressing a low amount of EGFP-tagged proteins. Imaging acquisition was carried out at 21-23 °C using Olympus oil objectives, PlanApo 100 (NA 1.40) or 150 (NA 1.45).

Single-vesicle docking and fusion experiments were performed as described in detail in ref. [138]. Synaptic/exocytic vesicle-associated v-SNARE proteins VAMP2/synaptobrevin and the target membrane associated t-SNAREs syntaxin and SNAP25 were reconstituted into small unilamellar vesicles (SUVs) and planar, supported bilayers (SBLs), respectively. The SUVs carry a small fraction of fluorescently labeled lipids. We used total internal reflection fluorescence microscopy (TIRFM) at 31 frames/s full-frame (512x512 pixels) or at 57 frames/s from a 400x256 pixel region of interest using a back-thinned EM-CCD camera (iXon DU897E, Andor technology).

3.3 RESULTS

Speckle TrackeJ was designed with the ability to correctly follow multiple moving particles over their lifetimes in the presence of inhomogeneous backgrounds, noise, particle crossings, and multiple sources of intensity fluctuations. We have however, implemented standard methods for sub-pixel particle localization, such as 2D Gaussian fitting. In Fig. 3.2 we demonstrate how the localization accuracy ϵ of our program depends on STN and pixel size [133, 139](see Supporting Material). We find ϵ scales approximately linearly with σ/λ and 1/STN, as in other algorithms [117, 140].

Below, we describe tests of our program, starting from simulated images of diffusing particles. We compare to other tracking tools in images of increasing complexity such as very high dynamic error and low STN. We proceed to demonstrate the application of our method to experimental systems in which other free tools were unable to provide us with results due to additional complexities.

3.3.1 Single molecule diffusion simulations

A common task in particle tracking is measuring the diffusion coefficient, D. To validate and test the software, we generated simulated images of diffusing particles

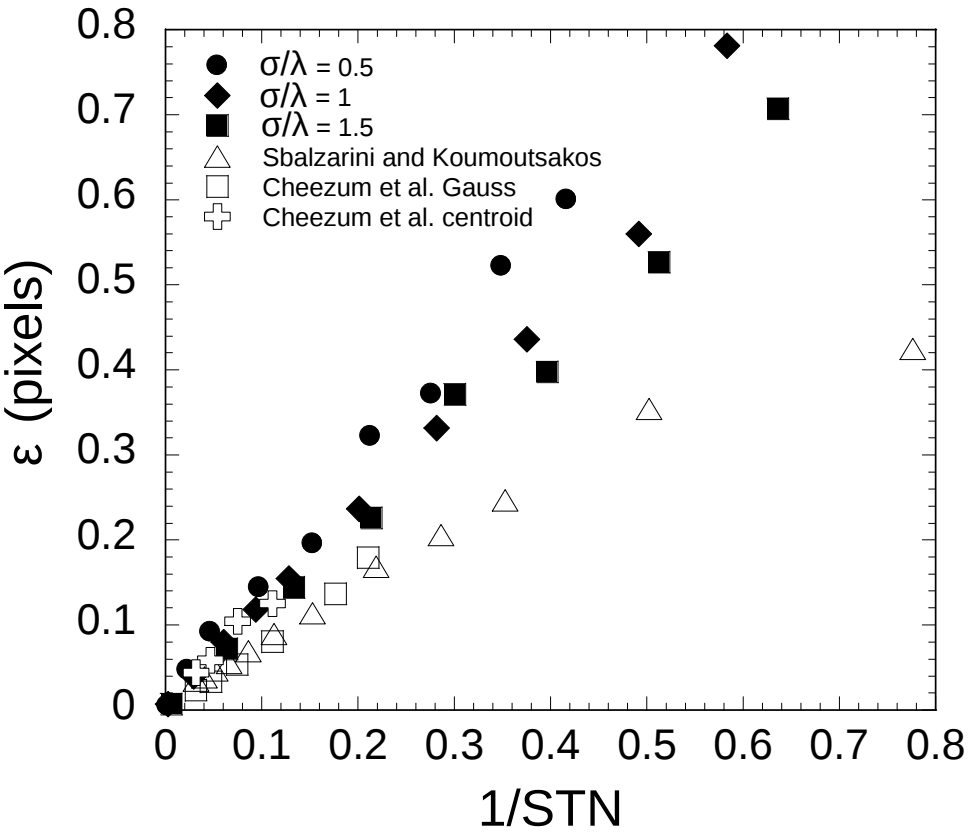

Figure 3.2: Standard deviation of the difference between particle position and speckle mark after refining with Gaussian Fit, ϵ, versus 1/STN. Plot for different ratios of PSF width to pixel size, σ/λ. Simulated particles were tracked as described in section 5 of Supporting Material. The graphs shows data from Fig. 4 of [139]($\sigma/\lambda = 1$ and Fig. 6 of [](${\sigma/\lambda \approx 1}$) who compared Gaussian fit and centroid algorithms. We did not include the lowest STN data in [139]since some of these data points fall outside of the graph.

with different background noise levels (Fig. 3.3A). We simulated point particles that perform random walks, contributing to the intensity to the image as they move during the exposure time, t_{exp}. The simulated camera exposure time was 50 ms and a pixel (px) represented 100 nm, similar to the experiments below. The time step $dt = 0.0001\text{px}^2/(4D)$ was adjusted such that the diffusion distance per dt is much less than a pixel. At each time step, particles were displaced by a distance selected from the 2D diffusion propagator probability distribution. The intensity of each particle was convolved with a Gaussian kernel of standard deviation 2 px, representing the point spread function.

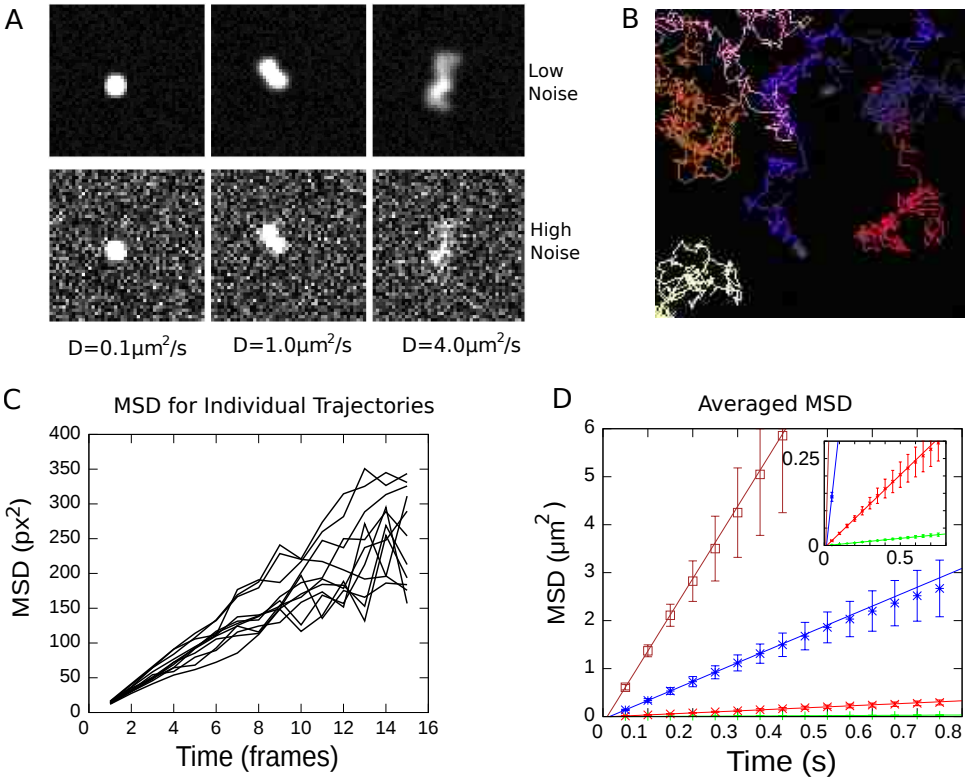

Figure 3.3: Tracking simulated diffusing particles. (A) Simulated images with increasing diffusion coefficients left to right. Bottom row shows same images with increased noise. (B) Marked trajectories. (C) MSD for individual tracks for D =1 μm^2/s2/s (low noise). (D) Averaged MSD plots for different diffusion coefficients in Table 1. Error bars are one standard deviation of the mean. Inset is an enlarged version.

Further we simulated the effects of camera noise, by adding normally distributed noise. We define the signal to noise ratio, STN = I/σ_{noise} , where I is the average intensity (above the background) at the position of the speckle mark and σ_{noise} is the standard deviation of the intensity at the same position [133, 139]. These simulations did not include other sources of error such as fixed pattern noise, vibrations, drift or fluctuations in the intensity of the fluorescent marker being tracked [111], see Discussion.

In Fig. 3.3A, slowly diffusing particles appear as small bright spots. With increasing D, diffusing particles appear as dimmer and more spread out clouds due to diffusion during the exposure. This contributes to "dynamic error" [140, 141]. In addition, fast-moving particles move farther so there are more crossed paths which

			u-track		Particle Tracker		Speckle TrackerJ	
D (μm^2/s)	STN	$4/3Dt_{exp} + 2\epsilon^2$ (px^2)	s^2 (px^2)	D (μm^2/s)	s^2 (px^2)	D (μm^2/s)	s^2 (px^2)	D (μm^2/s)
0.01	22.6	0.071	0.071 ± 0.001	0.011	0.071 ± 0.001	0.011	0.071 ± 0.001	0.011
0.01	4.4	0.17	0.186 ± 0.003	0.011	0.266 ± 0.006	0.010	0.236 ± 0.004	0.011
0.1	20.4	0.67	0.68 ± 0.012	0.10	0.68 ± 0.011	0.11	0.68 ± 0.012	0.11
0.1	3.7	0.82	0.79 ± 0.013	0.11	0.85 ± 0.07	0.068	0.8 ± 0.013	0.10
1	6.3	6.8	6.9 ± 0.12	0.99	6.8 ± 0.12	1.0	6.9 ± 0.12	0.98
1	2.9	6.8	7.1 ± 0.13	1.01	7.5 ± 0.4	0.91	7.7 ± 0.13	1.0
4	3.4	27	33.8 ± 0.9	3.4	35.7 ± 2.0	4.3	36 ± 1.0	3.7
4	2.1	27	28 ± 1.1	3.5			47 ± 2.1	3.6

Table 3.1: Results of tracking particles in simulated images using three different software tools. First two columns show simulated diffusion coefficient and STN value. The third column shows the theoretical value for s^2, a sum of dynamic error and static error. The latter was calculated using the value of STN and Fig. 3.2. The remaining columns show calculated s^2 and D. Empty boxes: we were unable to find good tracking parameters.

greatly hinders auto-tracking. The presence of noise especially limits the ability to detect clouds of fast-moving particles.

We tracked the particles in these images with our software and with two other software suites that have well-developed interfaces to handle complex tracking problems: Particle Tracker [133], which is based on the method developed by Crocker and Grier [117] and u-track [113]. We tracked particles with our program using the Diffusing Spots model and refined their positions using the Adjustment model followed by Gaussian Fit (Fig. 3.3B). To evaluate the accuracy, we measured the variance, s^2, of the distance between the speckle mark and the position of the simulated particle at the end of each exposure.

For low diffusion coefficients, 0.01 to 0.1 μm^2/s, all three particle trackers performed well, even at STN below 4, see Table 3.1. We were able to track the majority of the particles in the images through the end of the movie (301 frames), with little need to fine tune the program parameters (see Table 3.2). The calculated value of s^2 was consistent with the theoretical limit $s^2 > 4/3Dt_{exp} + 2\epsilon^2$, where ϵ is the static error in the absence of motion and $4/3Dt_{exp}$ represents dynamic error [140]. The calculated diffusion coefficients from plots of MSD vs lag time achieved an accuracy better than 10% in most cases. These results suggest that our software is comparable to the existing tools under conditions that demand sub-pixel accuracy, where particles move of order one or less pixels per frame.

At the larger diffusion coefficients, 1 and 4 μm^2/s, high dynamic error and low STN makes tracking particles more challenging. Due to motion during exposure the

		u-track		Particle Tracker		Speckle TrackerJ	
D (μm^2/s)	STN	N_{tracks} > 20 frames	Mean track lenth (frames)	N_{tracks} > 20 frames	Mean track lenth (frames)	N_{tracks} > 20 frames	Mean track lenth (frames)
0.01	22.6	12	301	11	301	12	301
0.01	4.4	12	301	22	96	12	301
0.1	20.4	14	247	12	278	11	299
0.1	3.7	14	251	6	24	12	289
1	6.3	20	174	30	109	13	274
1	2.9	46	75	16	26	29	118
4	3.4	47	29	12	27	10	144
4	2.1	24	29			5	101

Table 3.2: Results of tracking particles in simulated images using three different software tools. First two columns show simulated diffusion coefficient and STN value. Each movie had 12 particles and was 301 frames long. The table shows the number of particle tracks longer than 20 frames and mean track length from the runs we used to calculate the diffusion coefficients in Table 3.1. At low STN, bits of the same particle trajectory appear as different tracks as particles are lost and found, so the number of tracks is more than 12 in many cases. For Speckle TrackerJ we switched from batch auto-tracking to a combination of auto-tracking and manual interaction at $D = 4$ μm^2/s. Empty boxes: we were unable to find good tracking parameters.

intensity of a particle can be so low that it is not discernable from the background.

For the high D cases, tuning the parameters in u-track and Particle Tracker leads to a tradeoff between broken tracks, due to missed particles, and many short-lived false positives (see Tables 3.1 and 3.2). While the performance can be optimized through tracking and linking parameters, manually pruning and merging tracks is not provided by the software. To address this issue we limited our analysis to tracks that are longer than 20 frames. In this manner the calculated diffusion coefficients were within 15% of the actual values. At high diffusion coefficients particles cross frequently, and during fully automated detection we could not exclude regions with clusters of particles. Some longer tracks were generated by switching from particle to particle.

An advantage of Speckle TrackerJ is the ability to track particles selectively. We were able to achieve the same accuracy in measuring high D values by seeding candidate speckle marks in regions with isolated particles and then auto-tracking. Even when auto-track failed after 10 frames, multiple tools allowed us to quickly find and

manually join broken tracks and thus continue the track. For the highest noise and diffusion, both Speckle TrackerJ and u-track produced a similar number of total marks and a similar diffusion coefficient but the resulting tracks are quite different. Speckle TrackerJ yielded a few long tracks (see Table 3.2), which is an important aspect of particle tracking.

Each tracker required a similar amount of time to track particles. For problems that were tractable, the automated solutions for all three programs offered an advantage. For the more complicated scenarios, where it was impossible to automatically track all of the particles, Speckle TrackerJ quickly produced representative tracks. Selecting valid tracks is the main rate limiting step in the analysis of the following experiments where a significant number of bright features such as clumps of immobile fluorophores need to be excluded from analysis.

3.3.2 Single molecule diffusion capping proteins at the leading edge of motile cells

Capping protein (CP) plays a critical role in regulation of actin-based structures, such as lamellipodial protrusions and actin patches in yeast [47, 54]. The α and β CP subunits bind to free barbed ends of actin filaments, blocking access to the barbed end and preventing polymerization. CP also interacts with phosphatidylinositol 4,5-bisphosphate [142]. CP binding to membranes near the leading edge of motile cells may play a role in recruitment of CP protein to the leading edge [143, 144]. CP bound to the actin meshwork in lamellipodia dissociates from the network approximately 25-fold faster than actin subunits [39]. These findings suggested that cofilin-mediated actin filament severing triggers CP dissociation from the actin network by frequent severing. Fast severing and annealing reactions may contribute to structural reorganization of the actin network from the highly branched brushwork at the leading edge to the less branched network along the direction of retrograde flow [47].

To better understand why CP dissociates so fast in lamellipodia, we inspected diffuse CP which would be separate from the actin network. We expect the diffusion coefficient of CP to represent the size of the protein, or protein complex to which they are attached. We performed experiments on XTC cells expressing EGFP-CP β 1 at low amounts and acquired images of the cell edge showing single CPs (Fig. 3.4A, B). CP associated with the actin meshwork has a diffraction-limited spot appearance while the faster diffusing species are more spread out clouds, see Fig. 3.4A, B, similar

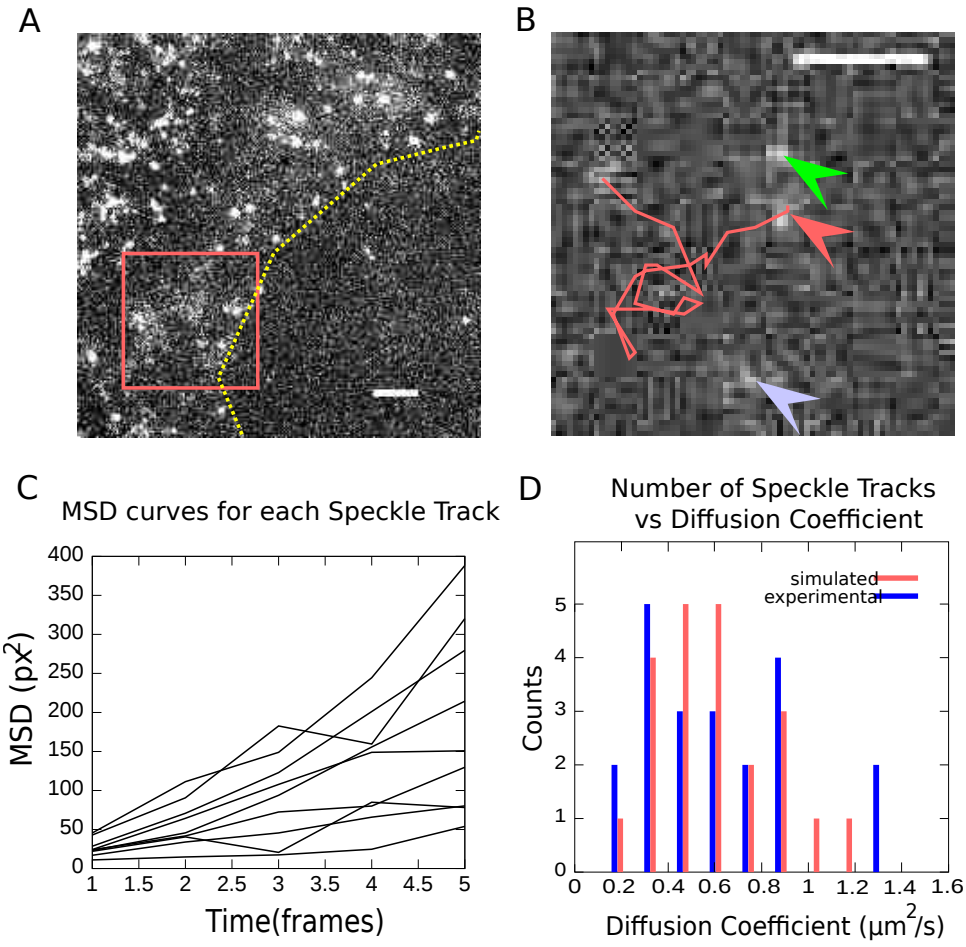

Figure 3.4: Tracking diffusing CPs at the leading edge of XTC cells. (A) Maximum intensity projection from a movie of GFP-labeled CP at the leading edge. Dashed line shows outline of leading edge. Exposure time was 66 ms and 1 pixel = 80 nm. Diffuse structures are diffusing molecules. Bright speckles are CP proteins bound to the actin meshwork. (B) Enlarged section of box of panel A, single frame. Line: trace of a speckle track. Middle arrow: start of track. Top arrow: another diffusing speckle. Bottom arrow: cloud too mobile to track for enough frames. (C) MSD plots for individual speckle tracks from the movie. (D) Distribution of diffusion coefficients found by fitting individual MSD curves with straight lines. Experimental: 22 tracked CPs. Simulated: results of tracking simulated particles for 10 frames with comparable conditions to the experiment: $D = 0.6\ \mu\text{m}^2/\text{s}$, 66ms exposure, 1 px = 80 nm. Bin sizes are $0.14\ \mu\text{m}^2/\text{s}$. Scale bars, $2\mu\text{m}$.

to the simulated images in Fig. 3.3A.

Tracking clouds of diffusing CP in Fig. 3.4 is challenging because of low STN, high dynamic error, the presence of many static speckles and, occasionally, organelles

that happen to contain fluorophores. The flexibility of our software allowed us to successfully track several of those diffusing molecules for 8-30 frames and calculate their individual MSD vs lag time curves (Fig. 3.4C). Fitting each MSD plot to a line, we calculated a distribution of diffusion coefficients, D (Fig. 3.4D). The measured D values are in the range 0.2 - 2 μm^2/s. Because we only tracked the CP speckles for as few as 10 frames, this range may represent measurement error: the accuracy in the measurement of D is lower when using shorter tracks. To evaluate this effect, we tracked particles in simulated images for 10 frames, with same exposure time and pixel size as in the experiment [145]. Each particle had $D = 0.6$ μm^2/s, and low noise was added to the image, same as in Fig. 3.3A. We found a spread of D values similar to the spread of values in experiments (Fig. 3.4D). We also note that the experimental images may include a population (we estimated no more than 50%) of CP with $D > 1$ μm^2/s, that could not be tracked.

The D values in Fig. 3.4D are much lower than those of proteins of similar molecular weight, e.g. actin monomers that are near 5 μm^2/s[146]. An intriguing hypothesis is that these slowly diffusing CPs are short severed actin filament oligomers. This would be consistent with the suggestion of Miyoshi et al. [39] that short CP lifetimes represent rapid actin filament severing near the barbed end. Future work is required, however, to test alternative mechanisms such as slow diffusion due to association of CP with the cell membrane.

3.3.3 Actin speckle lifetimes in lamellipodia

An important application of particle tracking involves measurements of lifetimes of actin monomers and tubulin dimers incorporated into filaments [39, 41, 122, 147]. When labeled actin or tubulin are in sufficiently low abundance compared to the unlabeled pool, polymerized labeled subunits appear as discrete speckles (Fig. 3.5B) [41]. Signals from diffusing subunits are much weaker since their intensity is distributed over several pixels (Fig. 3.3A). Depending on the marker concentration, the speckles may represent single molecules [39, 41, 122, 147] or groups of few labeled molecules [37, 40]. Single molecule speckle microscopy has shown that the dynamics of the cytoskeleton are characterized by continuous remodeling, involving constant assembly and disassembly that corresponds to speckle appearance and disappearance events in the images. Measurements of speckle lifetimes (time interval between speckle appearance and disappearance) have shown a broad distribution of lifetimes of actin

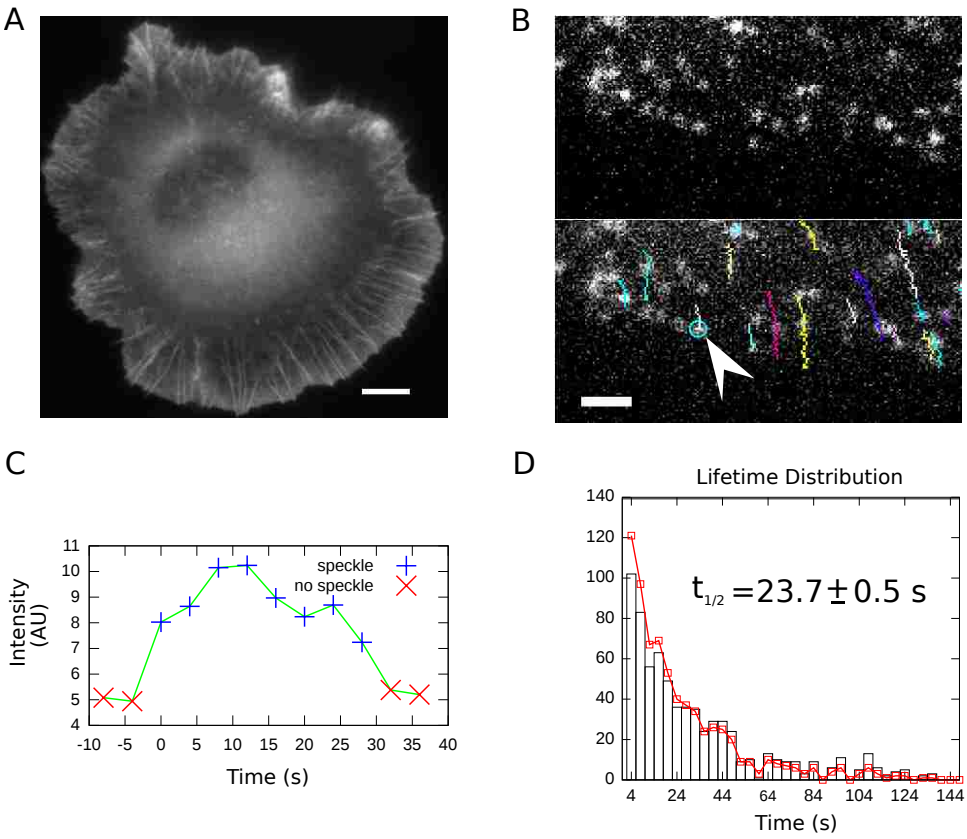

Figure 3.5: Speckle lifetime measurements. (A) XTC cell expressing EGFP-actin at high concentrations in which actin filaments in the lamellipodia appear as a continuous field. Scale: 8 μm. (B) Leading edge of lamellipodium with very dilute concentration of EGFP-actin. Single EGFP-actin monomers appear as speckles. Bottom: tracked speckles. Scale: 2.65 μm. (C) Intensity profile of speckle marked by arrow in panel B. (D) Histogram of speckle lifetimes (n = 709). Squares: raw data. Columns: data normalized for photobleaching. Normalization and half-life estimation as in [41].

in lamellipodia and tubulin in spindles[39, 41, 122]. Tracking of speckle motions also provides information on filament transport [37, 39–41, 122, 147].

We expressed EGFP-actin in XTC cells [39, 41], see Fig. 3.5A. We used cells with low EGFP-actin concentration (Fig. 3.5B). In this panel, each speckle is a single actin monomer bound to the actin meshwork of the lamellipodium. During the course of the video (4 s intervals at 2 s exposure/frame), the actin speckles move away from the leading edge due to retrograde flow, as shown by the tracks in Fig. 3.5B. Using the Constant Velocity NCC model, we tracked 900 actin speckles within 5 μm of the leading edge in 3-6 hrs, much faster compared to more than 12 hours with the

previous method [41]. Each track was carefully checked: the automatic tracking still needed to be monitored to make sure of false positives and speckle tracks that end prematurely due to gross changes in the background or blinking.

Fig. 3.5C shows a typical graph of the intensity of a speckle through its lifetime. Measurements of speckle lifetimes demonstrate the rapid turnover of actin in the lamellipodium (Fig. 3.5D). To calculate the half-life of actin monomers we adjusted the lifetimes to account for photobleaching and fit the cumulative number of speckles with an exponential [41]. The measured half-life of 24 s is close to the previously measured value of 30 sec [41].

3.3.4 SNARE-mediated fusion of single liposomes with supported bilayers, with single-molecule sensitivity Introduction

With few exceptions, intracellular fusion reactions are mediated by SNARE proteins; fusion is driven by pairing of vesicle-associated v-SNAREs with cognate t-SNAREs on the target membrane, resulting in a four-helix bundle (SNAREpin) that brings bilayers into close proximity [148, 149]. Much of our current mechanistic understanding of SNARE-mediated fusion has come from a bulk fluorescence dequenching assay in which small unilamellar vesicles containing v-SNAREs (v-SUVs) are mixed with SUVs containing t-SNAREs (t-SUVs) [149]. Recently, several researchers [150–153], including some of my co-authors [6, 138], have developed assays in which docking and fusion of single-vesicles with planar, supported bilayers (SBLs) can be detected. Unlike other single-vesicle approaches [150–153], this assay recapitulates the requirement for SNAP25, one of the essential t-SNARE components *in vivo*, without need for an artificial peptide [151]. Using this assay, it was demonstrated previously that SUVs reconstituted with the synaptic/exocytic v-SNAREs VAMP/synaptobrevin fused rapidly with planar SBLs containing the synaptic/exocytic t-SNAREs syntaxin 1-SNAP25, with single fusion events occurring 130 ms after docking, and requiring 5-10 SNARE complexes per fusion event [138]. Vesicles are continuously flown over the SBL. They dock at a constant rate and a small subset of docked vesicles fuse with the underlying SBL after a certain delay.

3.3.5 Diffusion of single fluorescent lipids from fused vesicles in supported bilayers

We used TIRFM to visualize for the first time the release and diffusion of single fluorescently labeled lipid molecules that initially reside in the SUV and become released into the SBL upon fusion of the two membranes. Because the SUV size is small (50 nm in diameter [138]), SUVs labeled with the fluorescent lipid LR-PE appear as diffraction-limited bright spots. After fusion, the LR-PE molecules diffuse away from the fusion site and become discernible as single speckles that can be tracked with 17 ms time resolution (Fig. 3.6A, B). More than 90% of the spots bleach in a single step, strongly suggesting they correspond to single-fluorophores. The challenge for tracking here is that the background at any time is filled with docked and unfused vesicles with a very broad range of intensities (due to different vesicle sizes and bleaching times), as well as with single molecules that have survived from other fusions. After visually identifying and seeding single molecules released from single fusion events, we tracked 33 single LR-PEs diffusing in the SBL that lasted more than 30 frames and calculated their MSD vs lag time (Fig. 3.6C). The averaged MSD (Fig. 3.6D), increases linearly with time, indicating a Brownian process. This suggests that the lipids that anchor the polymer cushion between the glass support and the SBL or membrane defects are dilute enough that they do not perturb LR-PE diffusion [154]. We find, in close agreement with the diffusivity estimated previously from the increasing spread of the overall fluorescence signal as a function of time after fusion [138].

3.3.6 Analysis of vesicle docking and fusion events

A crucial information, only obtained by single-vesicle docking and fusion assays, is the lag time for fusion after a vesicle docks onto the SBL. This time reflects molecular mechanisms required for vesicles to become fusion-ready (e.g. by recruitment of proteins via lateral diffusion to the fusion site [138]) or rearrangements of the lipids/proteins leading to membrane fusion. Docking of a vesicle onto the supported bilayer is characterized by the sudden appearance of a vesicle speckle, since TIRFM selectively visualizes only those vesicles very close to the surface. In contrast, fusion events are characterized by the spread of the fluorescence intensity (initially concentrated within a SUV which appears as a diffraction-limited spot) within the SBL after

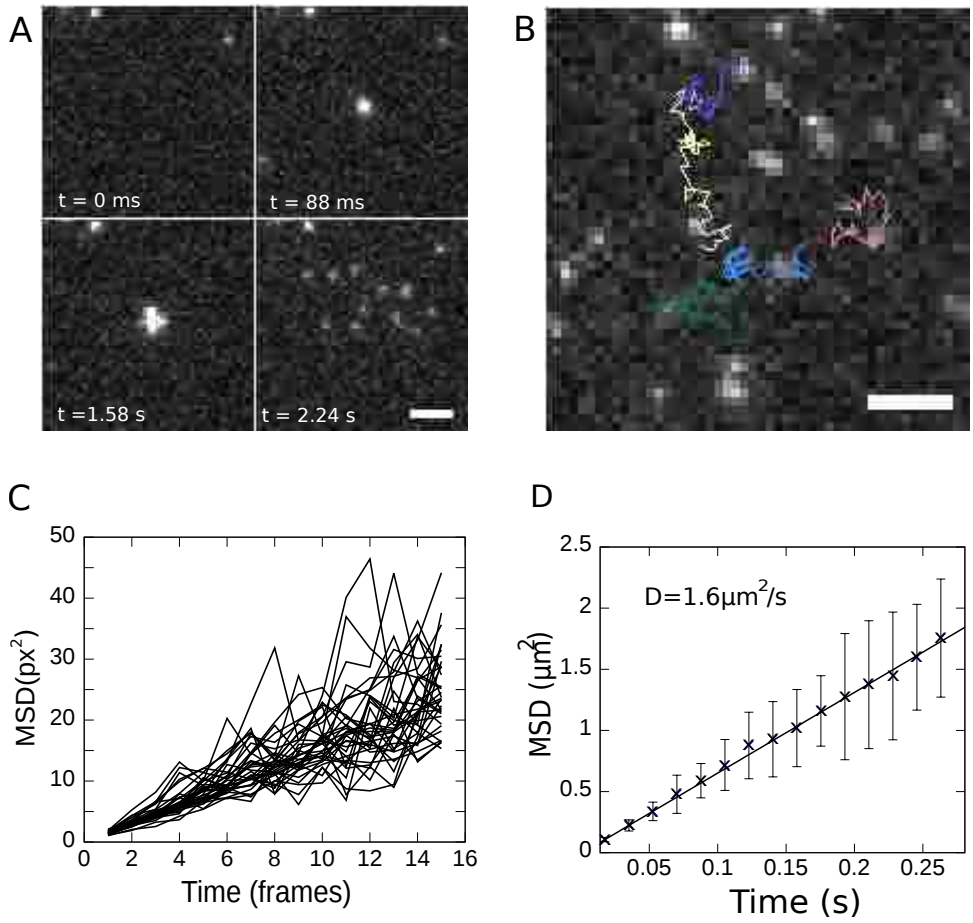

Figure 3.6: Single lipid tracking following vesicle fusion on a supported bilayer. (A) Montage of TIRFM images. Top left: before docking; top right: docking; bottom left: shortly after fusion; bottom right: more time after fusion. Released lipids diffuse on the membrane. Residual lipids from prior fusion events can be seen in the first frame. (B) Image of tracked lipids. Movie taken at 67 frames/s. (C) MSD for individual lipid trajectories. (D) Averaged MSD plots and linear fit from 33 lipids tracked for at least 30 frames. Error bars are one standard deviation of the mean. Scale: 2.67 μm (10 pixels).

merging of the SUV and SBL membranes.

Measuring docking-to-fusion delays is challenging, because: (i) the small subset of docked vesicles that fuse need to be identified, (ii) broken trajectories and false detections distort the lifetime of the docked state, (iii) docked vesicles have a broad intensity distribution, (iv) the vesicle disintegrates into numerous small speckles rapidly after fusion. Several algorithms have been designed for automated or lightly supervised detection of exocytosis events in live-cell TIRFM studies [120, 155, 156]. These

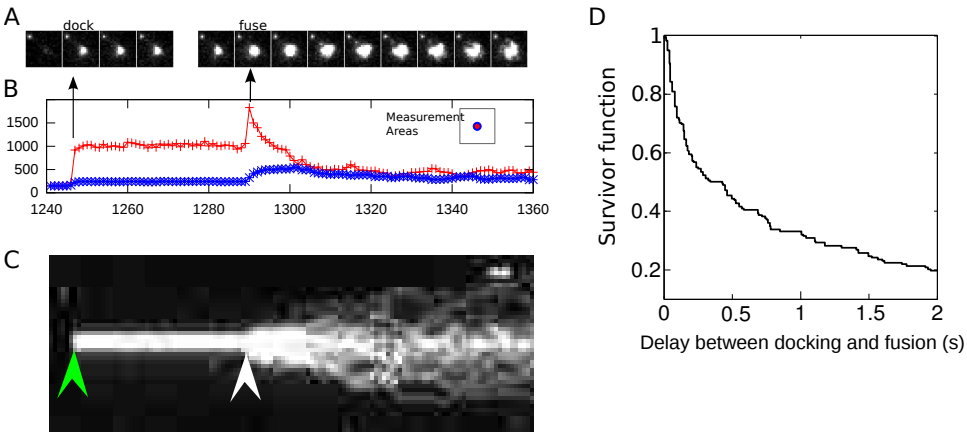

Figure 3.7: Detection and analysis of fusion events. (A) Successive frames of image sequence of a vesicle that docked (frame 1246) and fused (frame 1289). (B) Average intensities within an inner circle of 2.5 px radius centered at the position of the vesicle (top curve) and a surrounding ring 2.5 px wide (bottom curve). (C) y-t projection of an image sequence. Docked vesicle appears as a thin band (left arrow). Fusion results in formation of comet-tail appearance (right arrow). (D) Probability that a vesicle survived without fusion beyond a given delay after docking (178 fusion events from 10 different acquisitions).

dedicated programs work well in specific applications, but are not completely reliable when conditions (cell type, marker properties, STN) are changed. We have tested the program by Sebastian et al. [155] and a similar one written by E. Karatekin for SUV-SBL fusion, but have found that user input is required for the most reliable analysis of docking-to-fusion delays.

Two tools in Speckle TrackerJ assisted in identifying fusion events. The first is based on tracing the intensities within a small circle around a vesicle and a ring just outside the circle. When fusion occurs, the average intensity in the inner circle initially increases sharply, within one frame: fluorophores come closer to the glass-buffer interface where the evanescent field intensity is higher, as well as due to polarization and possible dequenching effects [118, 153, 157]. As the fluorophores leave the inner circle they enter the ring enclosing it. Thus, as the intensity in the inner circle drops, the intensity in the annulus increases (Fig. 3.7B). This simple criterion was used in the past for assisting detection of fusion events [121].

The second tool is based on the projection of a sequence of images (xyt) onto the y-t plane. A docked vesicle appears as a bright line in such a projection, with the start of the line corresponding to the frame in which the vesicle docked. If the

vesicle undocks, the line ends at the frame when undocking occurred. In contrast, if the vesicle fuses, then the dispersion of the fluorophores within the SBL results in a comet-like appearance of the projected profile (Fig. 3.7C).

Fusing vesicles were identified as described above, and were tracked from the first frame in which they docked until the frame in which fusion occurred. A sample sequence is shown in Fig. 3.7A. From these trajectories, we calculated the probability that a v-SUV survived beyond a delay t after docking (the survivor function), see Fig. 3.7D. The delay time distribution matches closely the distribution obtained previously using mainly manual analysis [138].

3.4 DISCUSSION

Speckle TrackerJ is most suited to situations where (i) STN is very low and/or particle mobility during camera exposure is high, (ii) the particles of interest constitute only a subset of all particles, (iii) particle lifetimes in addition to mobilities are desired, (iv) particle densities are not too high so that the user supervision/assistance during tracking is feasible.

The program can achieve sub-pixel resolution depending on the background noise and size of the pixel. Interpreting results that rely on sub-pixel resolution, however, requires careful consideration of additional issues, such as camera fixed pattern noise, vibration, shot noise, sample drift and dynamic error. We refer the reader to extensive discussions in the literature on the relative importance of these factors and for recommendations on how to select experimental conditions for optimal tracking accuracy [111, 114, 125, 140, 141, 158–161].

Tracking errors often lead to distorted MSD curves [111, 125, 140]. The ability to control the quality of the acquired data in Speckle TrackerJ can help avoid possible artifacts due to the assumptions of tracking algorithms. Of course manual editing could also introduce errors: manual filling of "gaps" in particle tracks could distort the resulting MSD curves over the timescales related to the size of these gaps. Various tools in Speckle TrackerJ allow for easier testing and control of these issues.

There is a general trend toward fully automated, unsupervised detection, tracking and analysis of larger and larger sets of data. However, at the forefront of single-molecule or single-vesicle biological research there are many situations where the STN is very low, particle mobility is high during detection, a small sub-population needs

to be selectively analyzed, and/or both the particles and the background have broad intensity variations. Careful supervision of all tracks is required in such challenging situations, especially if the experimental approaches are new. The development of SpeckleTrackerJ grew out of the need for a flexible tool combining supervised/assisted tracking with efficient automated algorithms. When imaging conditions are sufficiently good, SpeckleTrackerJ allows unsupervised tracking with performance comparable to other, existing tools. In extremely difficult situations, with light user assistance, it allows obtaining and supervising tracks where existing tools fail.

3.5 SUPPLEMENTARY MATERIAL

3.5.1 Additional information on particle detection methods

"Locate Speckles," has three parameters: threshold, size, and minimum distance. Using the threshold value, a binary image is generated. A two-pass connected components algorithm [162] is then applied to find speckle mark candidates. The position of a candidate is the center of mass of the connected component. Candidates are then removed if the number of pixels of the connected component is less than the size parameter. If the distance two candidates is smaller than the minimum distance parameter, the candidate with the smaller size is removed. "Template Locate," performs the same operation as the "Locate Speckles" method except that it uses existing speckle marks to create a Normalized Cross Correlation (NCC) [139] filtered copy of the image. The NCC template is made by averaging a square region of adjustable size centered at existing speckle marks. Thus the program can be trained simply by clicking to define a template.

3.5.2 Additional information on tracking models

"Static." The Static Model places speckle marks on all frames preceding the first frame of the speckle track, at the position of the first speckle mark. In a similar fashion, it places speckle marks on all frames following the last mark of the track at the position of the last mark.

"Extend Linear Refine." The Extend Linear Refine Model is similar to the Static model but it additionally tries to account for a small constant velocity during the movie. In this model, each additional mark at the beginning or the end of the speckle

track is adjusted using the "center of intensity" algorithm described in Eq. 3.4 below (around the position of the first or last existing mark, respectively). Once a speckle track that spans the whole movie is constructed, this model performs a weighted least squares fit to positions of the speckle track. Each point is weighted proportionally to the local intensity to obtain a velocity. Finally, all marks are updated to lie on a straight line trajectory determined by this velocity.

"Constant Velocity NCC" model is the same as Diffusing NCC but the search for the best candidate occurs over a square whose center is displaced from the position of the previous speckle mark. To estimate v, a linear least squares fit on each existing speckle track is performed during initialization. The velocities from the fit are averaged to calculate v.

3.5.3 Additional information on refine position models

Speckle tracks can be refined to improve the position of existing speckle marks. A technique used to refine positions moves the speckle mark to the center of intensity of an area of size 5x5 pixels:

$$\Delta x = \frac{\sum_{i=-2}^{2}\sum_{j=-2}^{2}(x+i)I(x+i,y+j)}{\sum_{i=-2}^{2}\sum_{j=-2}^{2}I(x+i,y+j)}, \Delta y = \frac{\sum_{i=-2}^{2}\sum_{j=-2}^{2}(y+j)I(x+i,y+j)}{\sum_{i=-2}^{2}\sum_{j=-2}^{2}I(x+i,y+j)} \quad (3.4)$$

This process is applied iteratively until the change in position is small (less than 0.01 px) or five iterations have occurred. The background noise will have a center at the center of the square but by iterating, the bright feature will 'pull' the center towards it.

The "Adjustment Model" modifies existing speckle tracks by using the above refine technique for every speckle mark. The Refine Model performs the operation of the Adjustment Model, then it applies a least squares fit to the positions of the existing marks as in the Extend Linear Refine Model. It also fills in missing speckle marks between the first and last frame of the speckle track.

The "Gaussian Fit" model refines the position of speckles with sub pixel accuracy. It fits a 2D Gaussian to the intensity of a 11x11 px^2 square near a speckle mark as follows using a least squares fit. The fit is started with a user-defined standard deviation of the Gaussian, σ (1 px is the default value). The position of the center of the Gaussian is varied using a variant of the simplex method as follows. Four points

are picked along the x and y axes with a distance of 0.75 px from the originally-estimated position. The amplitude and background of a 2D Gaussian centered at each point is found using a linear least squares fit, and the error is calculated. The results are sorted according to the error, which is the sum of the squares of residuals. The point with the highest error is moved toward the point with the lowest error, at the midpoint position. The process of moving the point with the highest error is iterated and continues until the largest difference in error among the points is below a threshold value (10^{-6}). This results in an estimate of the best position. The whole process is repeated for different σ, using a 1D golden section algorithm [163] with initial step $d\sigma = 0.1$ px to select for the sigma that minimizes the error. The fit is finished when the change $d\sigma$ is sufficiently small (less than 0.02 px). While this is perhaps the most accurate model when the particles are Gaussian spots, it is also the most computationally intensive.

3.5.4 User interface

Users can manually create and modify speckle tracks by clicking on the image (Fig. S1A), and by moving, trimming and merging of tracks. Further tools to aid in the users judgment are the Profiler, the Selection Table and the Reslice Control. The Profiler (Fig. 3.8C) graphs the intensity of the speckle over a circle with user-adjustable radius, r_{in}, and over an annulus with inner radius r_{in} and outer radius, r_out. The Selection Table (Fig. 3.8B) shows speckle track values such as maximum displacement per frame and distance of closest approach to neighboring tracks. The table allows users to sort and select speckle tracks, navigate the image stack and find problematic cases. The Reslice Control (Fig. 3.8D) makes a y-t projection of the original image stack to facilitate viewing the intensity through time.

3.5.5 Tracking precision

To evaluate the accuracy of our Gaussian Fit and tracking algorithm, we used a previously described method [133, 139]. Simulated particles that were stationary during exposure were displaced by a small distance (0.27 px) between exposures. We generated images of 12 such simulated particles for 101 frames using the method described in the Single Molecule Diffusion Simulations section of the main text. To check the effect of pixel size, λ, the intensity of each particle was convolved with a

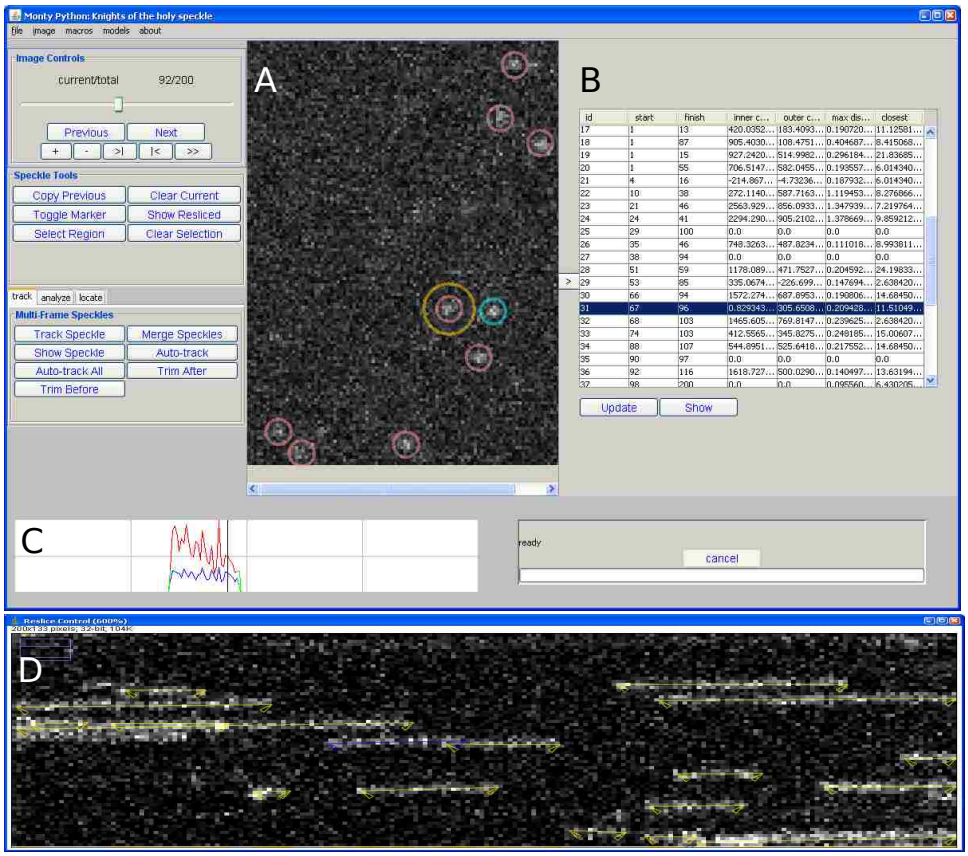

Figure 3.8: Speckle TrackerJ, user interface. (A) Image with marked speckles. (B) Selection Table shows data about tracked particles; it can be used to select speckle tracks. (C) Profiler shows the selected speckle intensity in different frames. (D) Reslice Control shows a projection of the movie with time as horizontal axis and the start and end points of speckle tracks.

Gaussian kernel of standard deviation $\sigma = 0.5$, 1, or 1.5 px. To study the effect of STN we varied the standard deviation, σ_N, of the added Gaussian noise.

Here, we define the signal to noise to be STN $= I/\sigma_N$ where I is the average intensity (above the background) at the position of the speckle mark. To better compare with previous studies we divide with σ_N instead of the standard deviation of the noise at the position of the particle (as was done in Table 3.1): otherwise fluctuations in the distribution of particle intensity among the pixels near the particle position leads to an absolute maximum STN value, even without added noise.

For each set of images, speckles were seeded, and tracked automatically using the Constant Velocity NCC model followed by the Adjustment and Gaussian Fit models.

Fig. 3.2 shows the dependence of the precision, ϵ, equal to the standard deviation of the difference between particle position and speckle mark, on STN and σ/λ. We find ϵ scales approximately linearly with σ/λ and 1/STN, as in other algorithms [117, 140]. The magnitude of our precision is comparable to those of previous tracking studies [133, 139], with small differences that are likely due to small differences in STN calculations and type of noise (the authors of [133] simulated Poisson noise). Because our tracking algorithm scans a large region of space before placing a speckle mark, the "bias" [133, 139], i.e. the average distance between speckle mark and particle position, was negligible.

3.5.6 Additional information on single-molecule imaging of fluorescent actin and capping protein

Live cell imaging was carried out as described in [39] by Naoki Watanabe. Cells were transiently transfected using Superfect (Qiagen) and maintained after passage into fresh flasks. Before experiments, cells were trypsinized and allowed to spread on a poly-L-lysine (PLL)-coated glass coverslip attached to a flow cell in 70% L-15 medium without serum for 30-60 min. The flow cell was then placed on the stage of an Olympus BX51 microscope equipped with Cascade II:512 (Roper Scientific). Fluorescent speckle microscopy was carried out by observing cells expressing a low amount of EGFP-tagged proteins. A restricted area near the cell edge was illuminated using a 75 W xenon illumination system. Imaging acquisition was carried out at 21-23 °C using the Metamorph software (Molecular Devise) and Olympus oil objectives, PlanApo 100 (NA 1.40) or 150 (NA 1.45).

3.5.7 Additional information on single-vesicle docking and fusion experiments

Experiments described below were performed by Erdem Karatekin. The following lipids were purchased from Avanti Polar Lipids, Inc. (Alabaster, Alabama): *1,2- dioleoyl-sn-glycero-3-phosphocholine* (DOPC), *1,2-dioleoyl-sn-glycero-3-phospho-L-serine* (sodium salt) (DOPS), *1,2-dioleoyl-sn-glycero-3-phosphoethanolamine-N-[methoxy(polyethy*

glycol)-2000] (ammonium salt) (mPEG2000PE), *1,2-dioleoyl-sn-glycero-3-phosphoethanolamine-N-(7-nitro-2-1,3-benzoxadiazol-4-yl)* (ammonium salt) (NBD-PE), *1,2-dioleoyl-sn-glycero-3-phosphoethanolamine-N-(lissamine rhodamine B sulfonyl)* (ammonium salt) (LR-PE). Expression, purification and reconstitution of the synaptic/exocytic vesicle-associated v-SNARE (soluble N-ethylmaleimide-sensitive factor attachment protein receptor) proteins VAMP2/synaptobrevin and the target membrane associated t-SNAREs syntaxin and SNAP25 were described previously [138]. Reconstitution of the SNARE proteins into small unilamellar vesicles (SUVs) was also done following ref. using the following lipid composition, in mole %: DOPC/DOPS/LR-PE/mPEG2000K =79.2/15/0.8 for the v-SNARE vesicles (v-SUVs) and DOPC/DOPS/NBD-PE/mPEG2000K=79.5/15/0.5/5 for the t-SNARE containing supported bilayers (t-SBLs). To have a relatively clean background, in this study we reduced the LR-PE label density on the v-SUVs to 0.8 mole %, whereas 1-2 % were used previously [138].

Planar, supported bilayers decorated with t-SNAREs were made to cover the bottom of microfluidic channels by bursting and fusion of t-SUVs onto clean, hydrophilic glass coverslip substrates. The NBD-PE label in the supported bilayer is used to assess the fluidity and quality of the t-SBL before introducing the v-SUVs into the channel.

The microscopy setup, the formation and characterization of the t-SBLs are described in ref. [138]. Importantly, two modifications here allowed us to detect single fluorescent lipids to be detected in the SBL after fusion for the first time: (i) to reduce the background signals, we reduced the LR-PE label density on the v-SUVs to 0.8 mole %, whereas 1-2% were used previously [138], and (ii) we used total internal reflection fluorescence microscopy (TIRFM) instead of far-field epifluorescence that was employed previously, allowing image acquisition at 31 frames/sec full-frame (512x512 pixels) or at 57 frames/s from a 400x256 pixel region of interest using a back-thinned EM-CCD camera (iXon DU897E, Andor technology). We used custom-made, high quality filters (clean-up: zet532/10x, dichroic: zt532rdc on custom 2 mm thick substrate, emission: hhq545lp and et605/70m) from Chroma Technology Corp. (Bellows Falls, VT). The fastest acquisition rates here are about 7 times faster than in ref. [138]

Chapter 4

Actin turnover in the lamellipodium: A model of FRAP using single molecule statistics

This chapter describes a model I developed to study actin turnover in the lamellipodium. The work has been submitted to Biophysical Journal and is awaiting review.

4.1 INTRODUCTION

4.1.1 Lamellipodium and related proteins

Lamellipodia are flat protrusions that allow cells to attach, and move across on flat surfaces (see Fig. 4.1A, B). This machinery for motility is used by a variety of cells such as white blood cells in the immune system or epithelial cells during wound healing and cell migration [47, 54]. The lamellipodium is characterized by a brushlike network of actin filaments, with their barbed ends located towards the leading edge of the cell [164]. Regulating proteins such as capping protein (CP), Arp2/3 complex, SCAR/WAVE, tropomyosin, and cofilin are also characteristic of lamellipodia. The regulators are controlled through signaling pathways that steer cells from external cues.

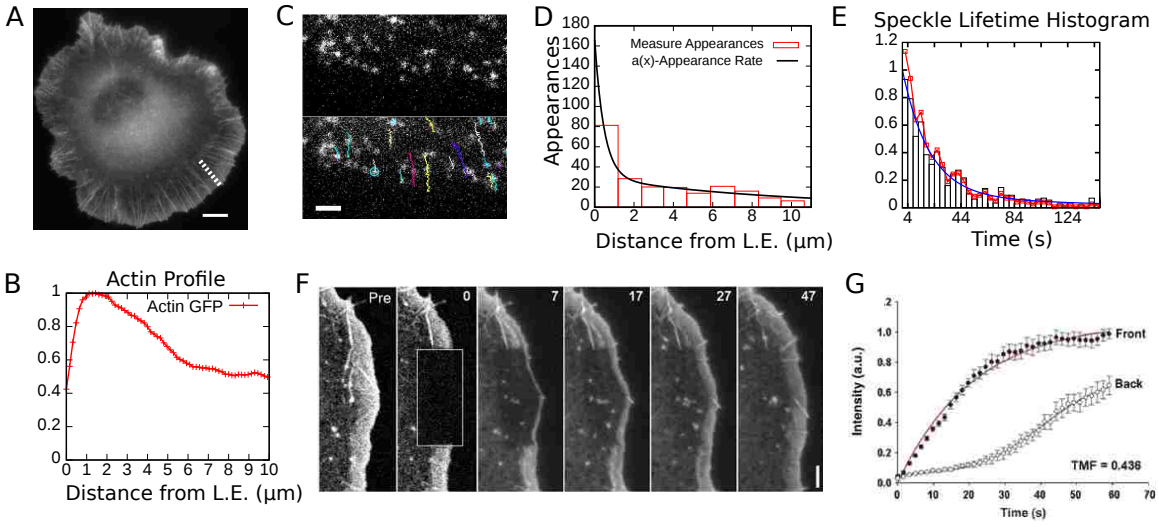

Figure 4.1: Prior experimental results to develop and validate model. (A) XTC cell expressing EGFP-actin at high concentrations [6]. Scale bar, 8 μm. (B) Intensity profile measurement from cell in A (along dashed line). (C) Cell expressing EGFP-actin at low concentrations [6]. Top: Individual speckles indicate single actin proteins. Bottom: same as top showing speckle tracks in time. The beginning and end of track (speckle appearance and disappearance) corresponds to polymerization and depolymerization. Scale bar, 2.65 μm. (D) Appearance events versus distance from leading edge (10) and double exponential fit. (E) Speckle lifetime distribution [6]. (F) FRAP experiment using a B16-F1 melanoma cell from [43] shows rapid recovery near leading edge and slow recovery away from leading edge. Scale bar, 2 μm. The average retrograde flow rate in [43] was 0.062 0.025 μm/s. (G) Measurement of FRAP kinetics at front and back halves of bleached regions.

4.1.2 Experimental work on lamellipodium

Many of the actin regulatory proteins have been characterized *in vitro*, but precisely how they control actin polymerization and depolymerization across the lamellipodium has not been completely resolved. The majority of actin polymerization in lamellipodia occurs near the leading edge (here we do not distinguish between lamellipodium and lamella [45]). Growing actin filaments push against the lipid membrane while the whole actin network undergoes retrograde flow [54, 165]. As the network moves toward the body of the cell, F-actin is depolymerized and recycled to be used again. Numerous experiments provide evidence that actin polymerization and depolymerization also occurs throughout the lamellipodium [47]: photoactivated labeled actin

showed turnover during retrograde flow [50]; microinjected fluorescent actin and electron microscopy experiments show barbed ends throughout the lamellipodium [36, 51]; phaloidin-stabilized neuron growth cones incubated with Alexa-488-G-actin shows incorporation of actin at barbed ends within a 2-3 μm band [52]; Single Molecule Speckle (SiMS) Microscopy demonstrates single molecules of actin polymerizing throughout the lamellipodium [41] (Fig. 4.1C); Quantitative Fluorescent Speckle Microscopy shows turnover of clusters of actin proteins far from the leading edge [40]; cells that are permeabilized and introduced with fluorescent CP demonstrate free barbed ends, or CP binding sites well into ($\sim 5\mu$m) the lamellipodium [39].

4.1.3 Models of actin turnover in the lamellipodium

The studies in the preceding paragraph indicate an extended distribution of barbed ends across the lamellipodium. However, fluorescent recovery after photobleaching (FRAP) experiments show that significant fluorescence recovery occurs fast near at the leading edge, while recovery away from the leading edge occurs with a delay followed by a more rapid increase [43, 44, 166] (Fig. 4.1F,G). A computational model by Lai et al. [43] reproduced the experimental FRAP observations assuming actin polymerization occurrs only very close to the leading edge. In this picture recovery at the back relies on retrograde flow of unbleached monomers from the very front [43, 167].

It has been proposed that reassociation of the bleached actin within the bleached area may slow down recovery [47]. This has been demonstrated by a reaction diffusion model of actin turnover in a spatially homogenous system without retrograde flow [146, 168, 169]. But the FRAP kinetics in a model that combines actin remodeling throughout the lamellipodium and retrograde flow have not been calculated.

Many previous models of actin in the lamellipodium have considered actin polymerization occurring exclusively at the leading edge [170–173]. The G-actin distribution has been studied considering populations of bound or sequestering actin monomers, assuming various combinations of sinks and sources of G-actin (representing polymerization and depolymerization) throughout the lamellipodium [174]. Other workers have implemented models that account for well known reactions at the leading edge, including assembly and disassembly away from leading edge and G-actin diffusion [175–177]. However the authors of [174–177] did not model FRAP curves. A three dimensional PDE model [173] was used to model FLAP, which is

similar to FRAP. This model treated actin monomers and polymers in a solvent but it did not include the effects of actin polymerization away from the leading edge. Another group studied FRAP of CP at the leading edge [178].

4.1.4 Overview

In the current chapter we consider models with turnover distributed throughout the lamellipodium. We demonstrate that the FRAP measurements are not clandestine to contradict experiments that indicate turnover throughout the lamellipodium. We compare two different models and show that turnover can occur without causing rapid FRAP recovery away from the leading edge. The first model uses diffuse actin that polymerizes and depolymerizes as monomers. FRAP curves simulated with this model are similar to, but not completely consistent with prior experimental observations. For the second model we consider two species of diffuse actin that can polymerize and depolymerize throughout the lamellipodium, monomers and oligomers (O-actin). Oligomers are slowly diffusing actin that can anneal to the F-actin network. The presence of a small amount of oligomers significantly reduces the amount of recovery away from the leading edge in simulated FRAP. The results of this model are consistent with both FRAP and SiMS microscopy.

The following models use speckle appearance rates and speckle lifetimes from SiMS microscopy [6, 41] to compute the steady state F-actin profile. The F-actin profile is then used to calculate the steady-state G- and O-actin profiles and the corresponding polymerization rates as function of distance from leading edge. Using these rate constants in a 2D stochastic simulation, we compute the predicted FRAP curves.

4.2 RESULTS

4.2.1 F-Actin profile based on speckle statistics

We used the statistics of single molecules of labeled actin obtained in previous studies of XTC cells (Fig. 4.1C) [6, 41] as an input to our model. The location of speckle appearance events correspond to polymerization and yield an appearance rate, $a(x)$, as function of distance from leading edge x (Fig. 4.1D) [41]. The units of a are $\mu\mathrm{M}/s$. To obtain an analytical form for $a(x)$, we fit the appearance curve with a

double exponential:

$$a(x) = G_\infty K \left(A_1 e^{-x/\lambda_1} + A_2 e^{-x/\lambda_2} \right). \tag{4.1}$$

The shorter length, λ_1, corresponds to polymerization at the leading edge while the longer length scale, λ_2, corresponds to basal polymerization that occurs throughout the lamellipodium. The total rate of appearance is scaled in proportion to the cytoplasmic concentration of labeled actin monomers far from the leading edge, G_∞. For convenience we pick $A_1 + A_2 = 1$ so K can be used as a parameter that adjusts the total rate of polymerization and the resulting F-actin/G-actin ratio ("F:G ratio"). The fit gives $A_1 = 0.82, A_2 = 0.18, \lambda_1 = 0.48\mu\text{m}, \lambda_2 = 9.1\mu\text{m}$. (How appearance events are distributed in space within the first 0.5 μm of the leading edge is not crucial for the present study).

Measurements of the speckle lifetime distribution in Fig. 4.1E, $p(t_l)$, give the probability distribution of the amount of time t_l that each actin subunit spends as F-actin. The lifetime distribution is approximately constant as function of distance from the leading edge [41]. We fit the lifetime distribution with a double exponential:

$$p(t_l)/p(0) = C_1 e^{-t_l/\tau_1} + C_2 e^{-t_l/\tau_2}, \tag{4.2}$$

where $C_1 = 0.904, C_2 = 0.096, \tau_1 = 20$ s, $\tau_2 = 128$ s. The velocity of retrograde flow v_r, (that ranges between 20-80 nm/s in XTC cells [179]) provides the remaining parameter necessary to construct an F-actin profile represented by the speckle statistics. Using the appearance rate $a(x)$ as a source of F-actin yields the steady state concentration profile:

$$F(x) = \int_0^\infty Y(x, x') a(x') dx'. \tag{4.3}$$

The profile $Y(x, x')$ generated by a point source at x' is obtained by considering the amount of subunits that have a longer lifetime than the time it took to travel from x' to x via retrograde flow:

$$Y(x, x') = \Theta(x - x') \frac{1}{v_r} \int_{\frac{x-x'}{v_r}}^\infty p(t_l) dt_l, \tag{4.4}$$

where the prefactor is found by balancing the amount due to retrograde flow out of with amount created by the point source.

The resulting F-actin profile in Fig. 4.2B is similar to the experimental profile shown in Fig. 4.1B. The profile in the figure becomes wider for larger values of the

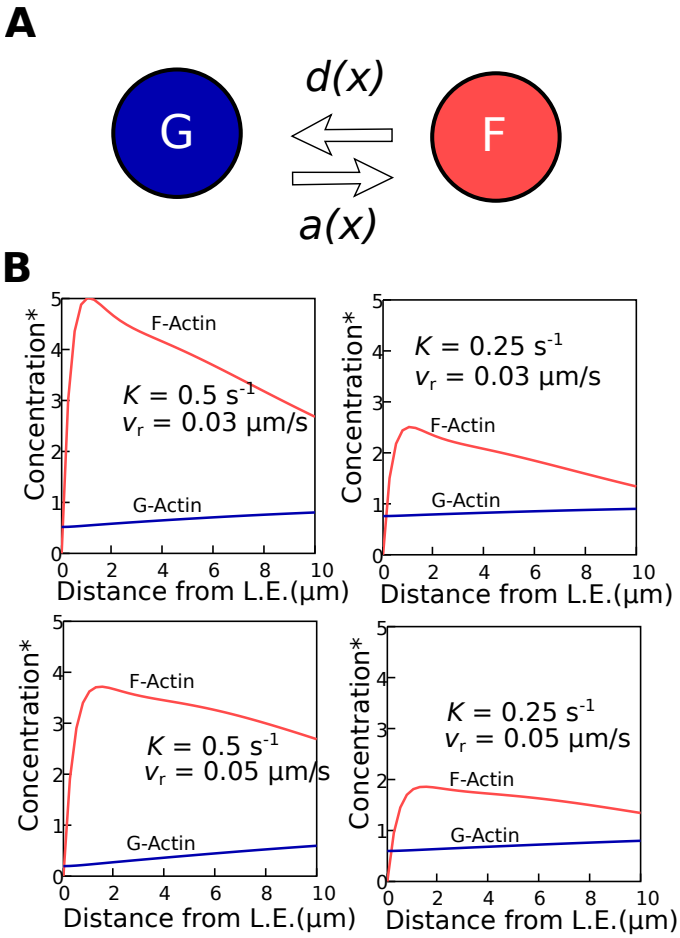

Figure 4.2: Speckle statistics used to create a steady state profile in a model with G-actin monomers as only diffuse actin species. (A) F- and G-actin states and transition rates. (B) Steady state profiles of F- and G-actin. Columns indicate different K values, which determine the F:G ratio. Rows are for different retrograde flow values. Concentration is normalized to G_∞ In this work we do not try to capture the exact position of the maximum of the F-actin profile that occurs within the first 1 μm from leading edge; this feature depends on the precise value of parameter λ_1.

retrograde flow rate. Plots of the disappearance rate $d(x)$, namely the rate with which F-actin becomes G-actin at steady state, show a peak between 1 and 2 μm away from the leading edge (Fig. 4.12C), similar to [175, 176]. The F-actin profile and $d(x)$ are the same for the two models we consider in this paper because they are determined by the measured appearance rate, retrograde flow, and speckle lifetimes.

Retrograde flow changes with distance from the leading edge, becoming slower for $x > 5$ μm in XTC cells [179]. We are interested in FRAP recovery within the first 5

μm so we do not consider this x-dependence.

4.2.2 G-Actin profile considering monomers as only diffuse actin species.

As a first model we consider that actin exists in two states: F-actin that undergoes retrograde flow, and G-actin with diffusion coefficient D = 4 μm^2/s[38, 168, 180, 181] (we also varied the value of D in Fig. 4.4). G-actin diffuses freely, polymerizing to become F-actin with rate a(x) (Fig. 4.2A). At steady state the exchange between F- and G-actin can be written as a function of position:

$$v_r \frac{\partial F(x)}{\partial x} = -D \frac{\partial^2 G(x)}{\partial x^2} = a(x) - d(x) \tag{4.5}$$

where $G(x)$ is the G-actin concentration. Knowing $F(x)$ from Eq. 4.3, we can solve Eq. 4.5 for the G-actin profile:

$$G(x) = G_\infty - \frac{v_r}{D} \int_x^\infty F(x')dx' \tag{4.6}$$

The resulting steady state profiles are plotted in Fig. 4.2B, normalized to the G-actin concentration far from the leading edge, G_∞. The value of parameter K determines the F:G ratio since it changes the magnitude (but not the shape) of the F-actin profile (see Eq. 4.1-4.3 and Section 4.4.2). By increasing K, the G-actin depletion near the leading edge is increased, see graphs from the left to right in Fig. 4.2B. Increasing the value of the retrograde flow velocity causes a greater depletion of G-actin shown by comparing the graphs vertically in Fig. 4.2B. The requirement that $G(x)$ remains positive restricts the possible values of K, v_r, and G_∞ and the maximum possible value of the F:G ratio $\int_0^L F(x)dx / \int_0^L G(x)dx$, where L is characteristic lamellipodium width. Measured values of the F:G ratio are in the rage 2-10 [35, 47, 182, 183] and the graphs in Fig. 4.2 show that the model can account for these F:G measurements.

4.2.3 Particle simulation with monomers as only diffuse actin species.

To calculate FRAP recovery curves in the monomer-only model we assume the transition rate monomers convert to F-actin is:

$$r_{G \to F}(x) = a(x)/G(x) \tag{4.7}$$

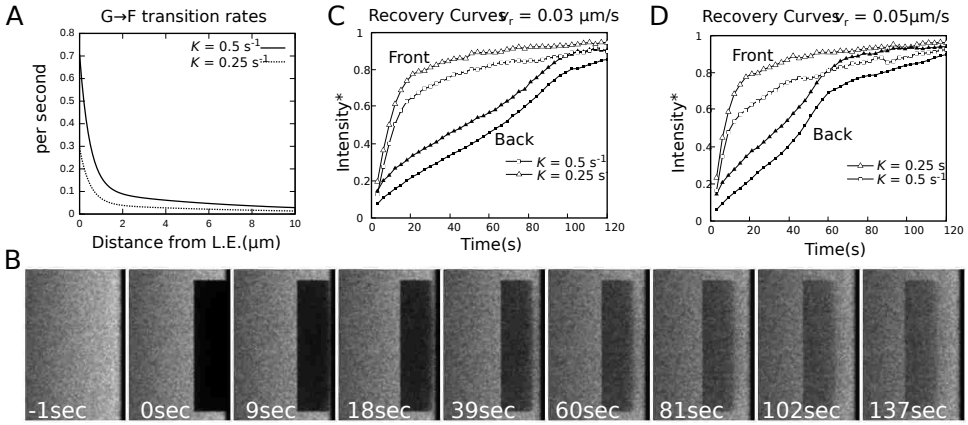

Figure 4.3: Simulated FRAP results in model with monomers as only diffuse actin species. (A) Calculated monomer transition rate as a function of distance from the leading edge for two different F:G ratios ($v_r = 0.05$ μm/s). (B) Example image of simulated FRAP. Size of bleached region 5 x 20 μm and $K = 0.5\text{s}^{-1}$,$v_r = 0.03\mu$m/s. Simulated exposure 500 ms/frame with 2500 ms lag between frames. (C) Normalized recovery curves at 0-0.5 μm (hollow symbols) and 2.5-3 μm (filled symbols) from leading edge, for two different K values. Intensities are normalized to the steady state value at the bleached position and approach 1 at sufficiently long times. (D) As B, for different value of retrograde flow.

Fig. 4.3B shows the calculated $G \to F$ transition rate using the measured $a(x)$ and $G(x)$ from Eqs. 4.1 and 4.6. Estimated values for the concentration of barbed ends are [B] ≈ 1 μM [47]. Using $r_{G\to F} = k^+[B]$, we find the rate constant close to the leading edge is $k^+ \approx 0.5\text{M}^{-1}\text{s}^{-1}$, consistent with previous estimates [47].

Eq. 4.7 contains an implicit relationship between polymerization rate constant, F:G ratio, retrograde flow rate and G_∞. This is a condition required for self-consistency of the model at steady state. It should not be used to infer a dependency between only two variables. For example, reducing cofilin concentration by shRNA decreases the retrograde flow rate [44] but Eq. 4.7 cannot be used in isolation to infer that this must also change the polymerization rate; such a perturbation may also decrease the G-actin pool and modify the F-actin lifetimes.

We used the transition rate, $r_{G\to F}(x)$, in an off-lattice 2D Monte Carlo simulation to simulate the reaction and diffusion of individual actin subunits in the lamellipodium (a rectangle extending 60 μm into the cell and 40 μm wide, with reflecting boundaries). Each subunit is either diffusing (G-actin) or undergoing retrograde flow

(F-actin). Subunits are updated every time step Δt, chosen to be sufficiently small, 1 ms or smaller. The distance traveled by diffusing monomers within Δt is picked from the 2D Gaussian diffusion propagator. After the monomer is moved, it is checked for association to the F-actin in the lamellipodium, which occurs with probability $r_{G\to F}(x)\Delta t$. When a monomer transitions to F-actin, its lifetime is picked from the lifetime distribution $p(t_l)$, see Section 4.4.3. The positions of F-actin subunits are updated by moving them in the direction of retrograde flow by distance $v_r\Delta t$. If they reach the boundary, they are converted back into G-actin (the size of the system was chosen large enough such that this is a rare event). After an F-actin subunit is moved, its lifetime is compared to the time elapsed since polymerization to check if it should depolymerize and become G-actin.

The system was initialized at steady state by using the concentration profiles obtain from the above analytical calculations (Eqs. 4.3 and 4.6). The lifetimes of the particles in the initial distribution were picked by applying Bayes rule (see Section 4.4.3). The resulting initial distributions of F- and G-actin subunits maintain the calculated steady state distributions, validating the simulations (see Fig. 4.13).

To simulate images, the particles are treated as diffraction-limited spots that diffuse during camera exposure [6]. The position of each particle is updated and exposed throughout the exposure time, $\sim 10^6$ times per exposure, to produce a simulated lamellipodium image. Bleached particles are removed from the simulation and do not contribute to intensity.

4.2.4 FRAP recovery in model with monomers as only diffuse actin species.

A simulated FRAP image is shown in Fig. 4.3B where a region of size 5x20 μm is bleached near the leading edge. Fig. 4.3C, D show the recovery of intensity at two strips between 0-0.5 μm, and 2.5-3 μm ("Front" and "Back" respectively) from the leading edge. Overall, the recovery curves are similar to the recovery curves seen in experiments (Fig. 4.1G), with fast recovery at the front and slower recovery at the back.

Recovery at the front involves three stages. First, unbleached G-actin diffusion to the leading edge within about 2 sec, assuming free diffusion (see discussion on inhibited diffusion below). Second, the F-actin increases until a balance is established between polymerization of G-actin and removal of F-actin by both retrograde flow

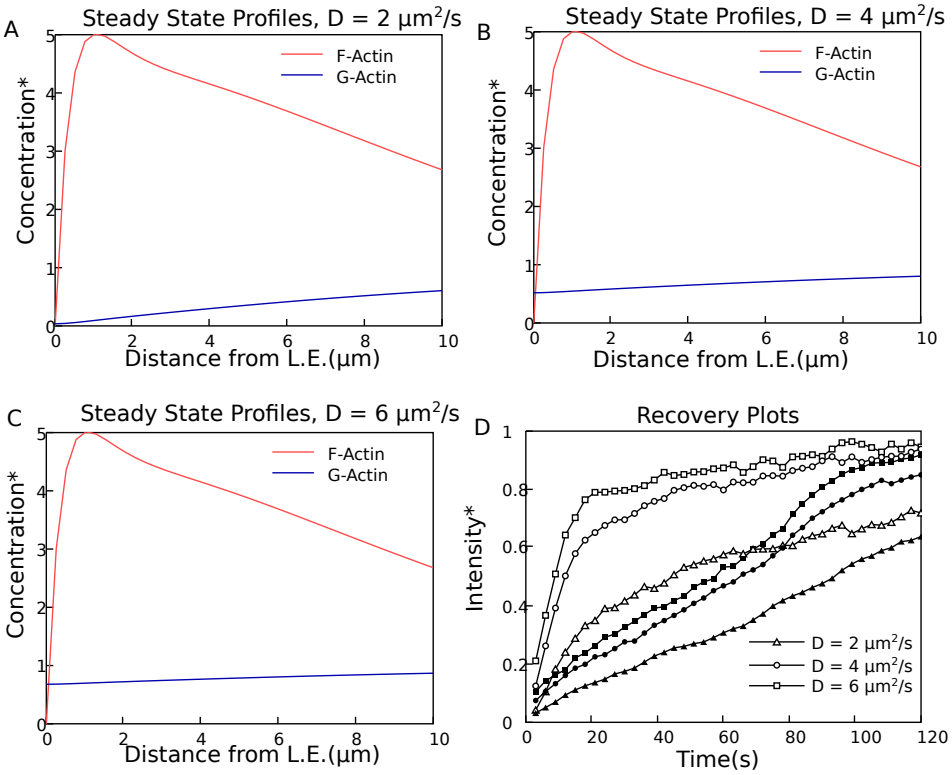

Figure 4.4: Effects on profile and FRAP due to changing the diffusion coefficient in monomer-only model. The other parameters remain the same, $K = 0.5$ s^{-1} and $v_r = 0.03$ μm/s. Steady state profiles for (A) $D = 2$ μm^2/s, (B) $D = 4$ μm^2/s, and (C) $D = 6$ μm^2/s. (D) Comparison of FRAP recovery results for different values of D (front: empty symbols; back: filled symbols). Decreasing D increases the gradient of the G-actin profile and slows down FRAP recovery at both the front and the back of the lamellipodium. Some studies have suggested D values as large as 14 μm^2/s[54]. For such large values of D the G-actin profile becomes flat and the FRAP curves approach a limit that is similar to those of $D = 6$ μm^2/s.

away from the leading edge region and depolymerization. Since the time it takes for an F-actin subunit to be carried away from the front region, 0.5 μm/vr, is within 10-15 s, and since the average speckle lifetime is 60 s (see Eq. (S11) and Eq. 4.2), retrograde flow is the dominant removal mechanism of F-actin close to the leading edge. Thus this second stage completes in about 10-15 sec. Third, there is a slow recovery due to algebraic tail of the G-actin diffusion (see also Fig. 4.4) while the local F:G ratio remains approximately constant.

Recovery at the rear is slower than at the front. There is a qualitative difference

between the shapes of the simulated (Fig. 4.3C,D) and experimental (Fig. 4.1G) recovery curves. In the experimental data there is little recovery until 35 sec, which is about the time retrograde flow carries fresh monomers from very close to the leading edge into the region. Recovery at the back involves G-actin diffusion into the bleached region, G-actin transitioning to F-actin (that occurs over $1/r_{G\to F} \approx 13$ sec, see Fig. 4.3A), and retrograde flow carrying unbleached subunits to the rear. In the simulations, retrograde flow carries unbleached monomers from the very front to the back in 30 s and 50 s in Fig. 4.3C, D, respectively, and causes an abrupt increase in slope. However, the intensity at the back has already started to recover at earlier times due to the basal polymerization.

It has been shown that a high F:G ratio can cause a delay in FRAP since association of G-actin into F-actin hinders the diffusion of G-actin into the bleached region [168]. This effect becomes important when the typical distance travelled by G-actin before reassociation to F-actin [174], , $s = \sqrt{4D/r_{G\to F}}$ becomes comparable to the size of the bleached region. In Fig. 4.3A, increasing K increases $r_{G\to F}$. To estimate s, we use $r_{G\to F}$ at the mid-point of the bleached region. For $K = 0.25$ s^{-1}, we find $s = 19$ μm and for $K = 0.5$s^{-1}, s = 12 μm, which are larger than the width of the bleached region. Thus while hindered diffusion has an effect on the recovery in Fig. 4.3, it cannot fully account for slow recovery at the back in experiments. To explore this concept further we look at the consequence of changing the diffusion coefficient, D, see Fig. 4.4. Changing D changes the G-actin distribution, causing a larger G-actin depletion near the leading edge for smaller D values. When $D = 6$ μm^2/s, $s = 16\mu$m and the shapes of the recovery curves in Fig. 4.4D are qualitatively similar to Fig. 4.3C. When $D = 2$ μm^2/s, $s = 4.8\mu$m and we see a much stronger delay in both front and back recovery. A remarkable feature of the $D = 2$ μm^2/scase is that the recovery at the front is slowed much more than the recovery at the rear. This indicates that hindered diffusion cannot explain the slow recovery at the rear in Fig. 4.1F while still allowing the fast recovery at the front.

We also considered the effects of having a longer lifetime, τ_2 (Fig. 4.5) and found that it slows recovery, but does not have enough of effect within values close the measured values (Fig. 4.1E). The factor that changed the shape of the back recovery the most was λ_2, which determines how far into the lamellipodium polymerization occurs. By reducing λ_2 close to λ_1 we get recovery curves more similar to a treadmilling model, but this is equivalent to assuming negligible polymerization away from

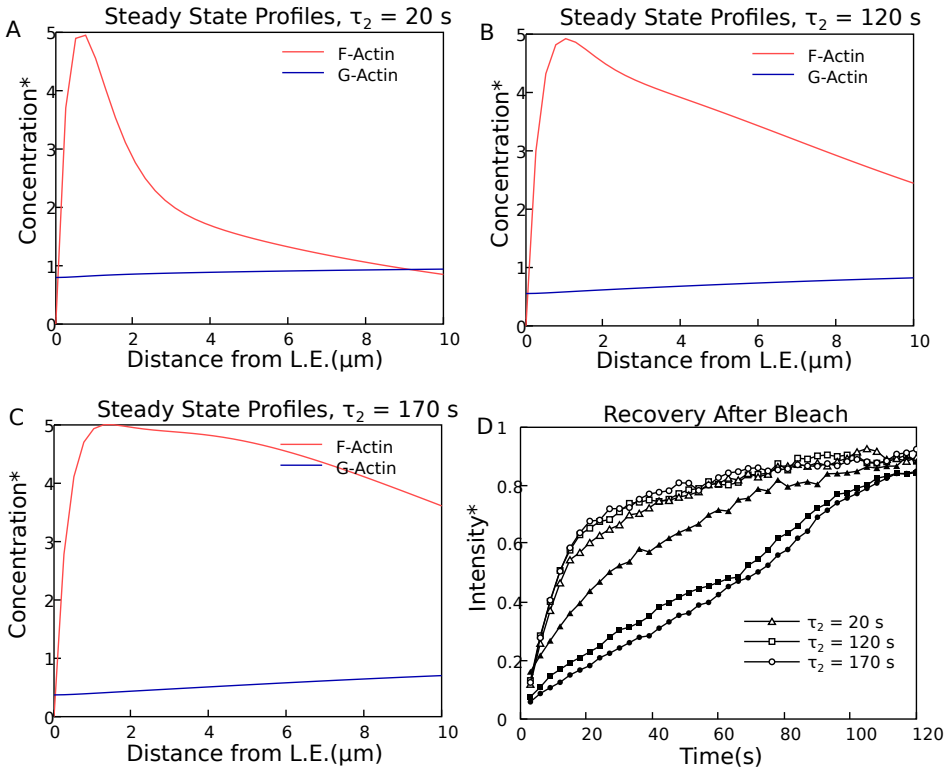

Figure 4.5: Effects on concentration profile and FRAP in monomer-only model due to changing value of parameter τ_2 that describes the lifetime of the "long-lived" F-actin subunits, see Eq. 4.2. The value of τ_2 used in the main text was 128 s. Steady state profiles for (A) $\tau_2 = 20$ s, $K = 0.67$ s$^-$1, (B) $\tau_2 = 120$ s, $K = 0.5$ s$^-$1, and (C) $\tau_2 = 170$ s, $K = 0.45$ s^{-1}. The value of K is also changed to keep the F:G ratio about the same. (D) Comparison of FRAP recovery results for different values of τ_2 (front: empty symbols; back: filled symbols). The other parameters remain the same and $v_r = 0.03$ μm/s, for all three values of τ_2.

the leading edge (Fig. 4.6).

We did not explicitly account for the fact that G-actin monomers can carry different types of nucleotide (ADP or ATP), or that monomers can be bound to profilin, thymosin or cofilin. We assumed that the reactions among these different states occur fast enough to be considered quasi-static and also do not modify the diffusion coefficient of bound G-actin [174]. Thus, the values of rate constants represent the average behavior of the G-actin pool. If there is a time that must elapse before a depolymerized monomer is able to repolymerize, this delay would not modify the shape of the FRAP curves qualitatively (this would be similar to using a higher K, see Fig. 4.3C, D and also Fig. 4.11 below).

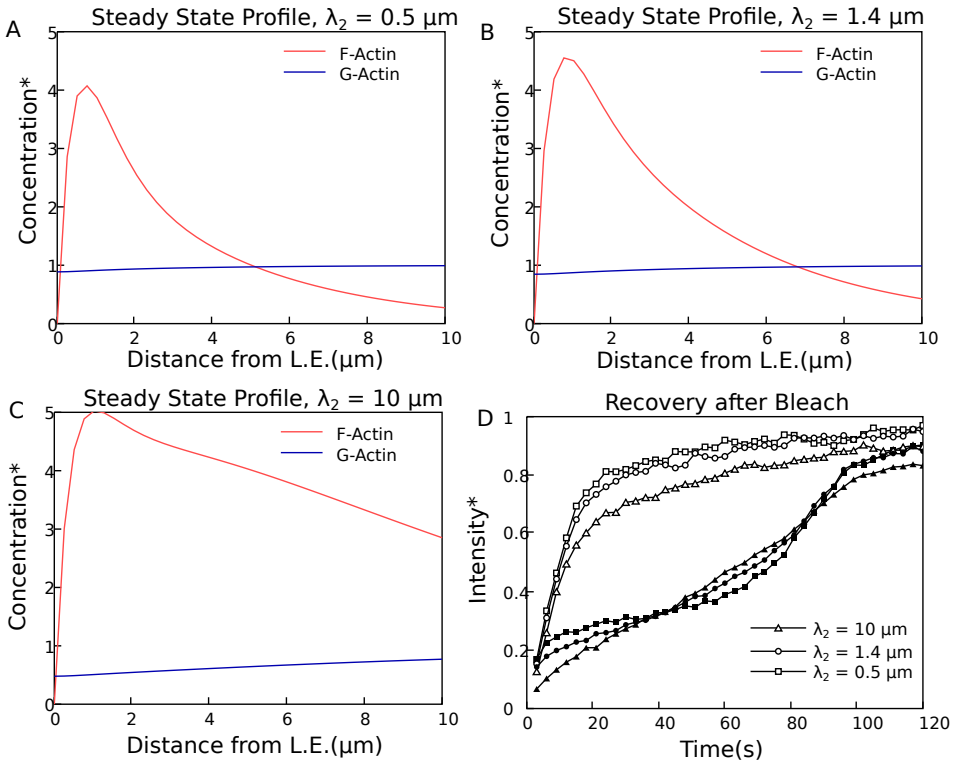

Figure 4.6: Effects on concentration profile and FRAP in monomer-only model due to changing value of parameter λ_2 in Eq. 4.1, which determines how far into the lamellipodium polymerization occurs. The value of λ_2 used in the main text was 9.1 μm. (A) λ_2 =0.5 μm (B) λ_2 = 1.4 μm (C) λ_2 = 10.0 μm all other parameters kept the same: $K = 0.5$ s^{-1}, $\lambda_1 = 0.5$ μm, $v_r = 0.03$ μm/s. (D) Recovery plot comparing three different recovery curves for the different λ_2 (front: empty symbols; back: filled symbols).

The discrepancy in the back recovery curves between model and experiment is small, but it illustrates the difference between a treadmilling type model and a model with remodeling further away from the leading edge. A smaller discrepancy is that the simulated recovery at the front has a slow tail, unlike experiment, for $K = 0.5\text{s}^{-1}$ that corresponds to realistic F:G ratios. These results indicate that a model which only includes monomers as the diffuse actin species cannot fully account for both SiMS and FRAP results. In the next section we examine the possibility that appearance events in SiMS microscopy are caused by both G-actin and slowly diffusing actin oligomers.

4.2.5 Model with both monomers and oligomers contributing to appearance events.

Several works suggest actin oligomers are present in the lamellipodium. Cofilin causes severing of actin filaments [184–187] and the Arp2/3 complex nucleates actin filaments that can debranch in vitro [19, 188]. The short lifetimes of CP speckles in lamellipodia, which depend on cofilin-catalyzed, jasplakinolide-sensitive actin disassembly, indicate severing of capped filaments [39]. Oligomer annealing [189, 190], possibly involving Aip1-capped filaments [191–193] could be a mechanism for structural reorganization of actin filaments in the lamellipodium [39, 191]. This could assist the change from a densely branched network near the leading edge to a network of longer filaments further away [164]. However, a different picture has been discussed after recent cryo EM experiments [194–197].

Oligomer generation and annealing would be consistent with SiMS observations. Oligomers with diffusion coefficient $D_O \approx 0.5\mu\text{m}^2/\text{sand}$ a fluorescent subunit would appear as background noise during exposure in SiMS experiments [6]. If they anneal to the network, they would contribute to speckle appearance events in SiMS experiments. When they dissociate from the network (via severing or debranching) they would contribute to speckle disappearances. Since the diffusion coefficient in the cytoplasm decreases with increasing molecular weight of protein complex [198], such D_O values may represent fragments of order 10 actin subunits or less.

In the model shown in Fig. 4.7A, G-actin monomers can associate into F-actin and F-actin subunits depolymerize into O-actin. Subunits of O-actin can become F-actin or disassemble to G-actin with an average lifetime τ_O. O-actin is a slowly diffusing species of actin with a different appearance profile than G-actin (Fig. 4.7B). The total appearance rate is separated into oligomers, $a_O(x)$, and monomers, $a_G(x)$, with $a(x) = a_O(x) + a_G(x)$. We assume O-actin accounts for a majority of appearance events away from the leading edge while G-actin polymerization contributes to most events close to the leading edge. Given the evidence for barbed ends throughout the lamellipodium, we expect both O- and G- actin to associate away from the leading edgehere we examine a limiting case to illustrate how much of an effect oligomer-based remodeling changes FRAP. The relative G- and O-actin contribution to appearances is considered in the Discussion.

We use the speckle appearance rates and lifetime distributions to calculate the

steady state profiles. At steady state, similar to Eq. 4.5:

$$v_r \frac{\partial F(x)}{\partial x} = a_O(x) + a_G(x) - d(x), \tag{4.8}$$

$$D_G \frac{\partial^2 G(x)}{\partial x^2} = a_G(x) - \frac{1}{\tau_O} O(x), \tag{4.9}$$

$$D_O \frac{\partial^2 O(x)}{\partial x^2} = a_O(x) - d(x) + \frac{1}{\tau_O} O(x), \tag{4.10}$$

where $D_G = 4$ μm^2/sand D_O are the G- and O-actin diffusion coefficients. The F-actin profile is given by the same expression as in Eq. 4.3, so we can substitute in Eq. 4.8 to solve for $d(x)$, which leads to $O(x)$ through Eq. 4.10:

$$O(x) = \tau_O \cosh(\frac{x}{\sqrt{D_O \tau_O}}) \int_0^\infty f(x') \exp(\frac{-x'}{\sqrt{D_O \tau_O}}) dx' - \tau_O \int_0^x f(x') \sinh(\frac{x - x'}{\sqrt{D_O \tau_O}} dx'. \tag{4.11}$$

The G-actin profile can then be solved similar to the monomer model, using Eq. 4.9:

$$G(x) = G_\infty - \frac{D_O}{D_G} O(x) - \frac{v_r}{D_G} \int_x^\infty F(x') dx'. \tag{4.12}$$

Examples of calculated profiles are shown in Fig. 4.7C, where we used $D_O = 0.5$ μm^2/sand $\tau_O = 20$ s. The total amount of O-actin is quite low compared to the amount of F and G-actin, while still making a contribution to the total appearance rate. Provided $D_O < 1$ μm^2/sand $\tau_O > 2$ s, these parameters do not affect the shape of the FRAP recovery curves significantly (Fig. 4.9, 4.10).

4.2.6 FRAP simulations using O-, G- and F-actin.

The O- and G-actin binding rates were obtained from the steady state profiles, $r_{G \to F} = a_G(x)/G(x)$ and $r_{O \to F} = a_O(x)/O(x)$ (Fig. 4.8A). Using these rates we performed stochastic particle simulations to produce images of simulated FRAP (Fig. 4.8B), as in the monomer-only model. The new model captures two features of the experiment in Fig. 4.1G that the monomer-only model did not contain:

(1) Recovery away from the leading edge (Fig. 4.8C and 4.8D) is slower than the recovery in the monomer-only model (Fig. 4.3C and 4.3D), which is more consistent with the experimental results. The resulting FRAP curve at the back does not show significant recovery until retrograde flow carries monomers from the leading edge into the back region. For the chosen parameters, oligomers do not diffuse into the bleached region before retrograde flow transports monomers from the leading edge into the region. Two factors contribute: (i) the time required to travel distance

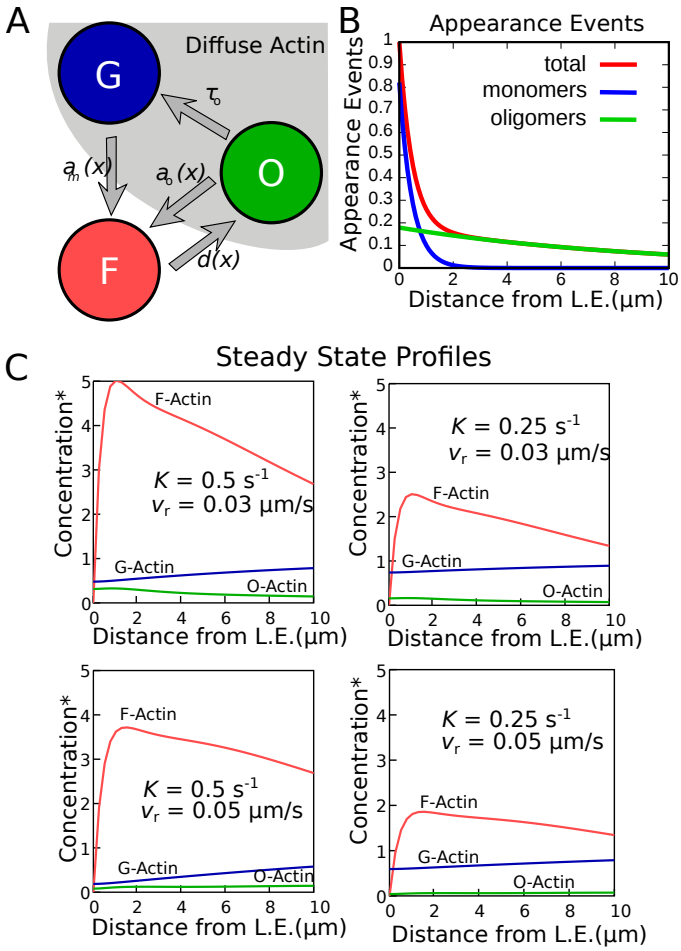

Figure 4.7: Speckle statistics used to create a steady state profile in a model with both G-actin and actin oligomers (O-actin) as diffuse species. (A) F-, G- and O-actin states and transition rates. (B) Appearance events broken into monomers and oligomers. We consider the limit where speckle appearance events far from the leading edge are mostly due to oligomers. (C) Steady state profiles for two different K values and two different retrograde flow velocities ($\tau_O = 20$ s, $D_O = 0.5$ μm^2/s). Concentration is normalized to G_∞

of order 3 μm by free oligomer diffusion is about 4.5 s but this is slowed down by rebinding of O-actin within the bleached region [168] since 2.5 μm; (ii) generation of a new O-actin subunits from unbleached monomers that polymerize at the leading edge requires times of order the average speckle lifetime.

(2) The recovery at the leading edge (Fig. 4.8C and 4.8D) does not have a significant long tail and is similar to Fig. 4.1G, even with the higher K value. The tail in the front recovery curve in Fig. 4.3C for $K = 0.5$ s^{-1} was due to hindered diffusion

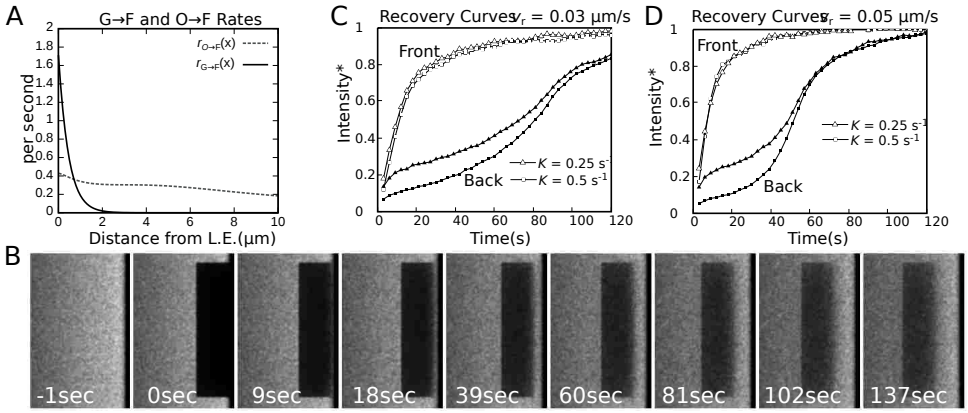

Figure 4.8: FRAP in model with both G-actin and O-actin as diffuse species ($\tau_O = 20$ s, $D_O = 0.5$ μm^2/s) shows better agreement with experiment in Fig 1. (A) Calculated transition rates as function of distance from the leading edge ($K = 0.5$ s^{-1}, $v_r = 0.05$ μm/s). (B) Example image of simulated FRAP. Size of bleached region 5 x 20 μm and $K = 0.5$ s^{-1}, $v_r = 0.03$ μm/s. (C) Normalized recovery curves at 0.5 μm (hollow symbols) and 3 μm (filled symbols) from leading edge, for two different K values. The shape of the recovery at the back is similar to the experiments in Fig. 4.1G. (D) Same as B, for different value of retrograde flow.

[168]. In the model with oligomers, the region of G-actin polymerization is narrow, and this effect is reduced in magnitude.

The above results support models that include annealing and severing in the lamellipodium [172, 176]. They indicate that SiMS results may be consistent with FRAP data, and reveal the kinetics of a population of actin not previously characterized in cells.

4.3 DISCUSSION

We used modeling to show how the combination of SiMS and FRAP experiments provides information on the actin remodeling kinetics at the lamellipodium. A model in which all diffuse actin species are identical and have a single diffusion coefficient predicts a slow, continuous recovery at the back of the lamellipodium, different to the experiment in Fig. 4.1G that shows a two-stage recovery process. Possible contributors to this apparent discrepancy are: differences between experimental systems

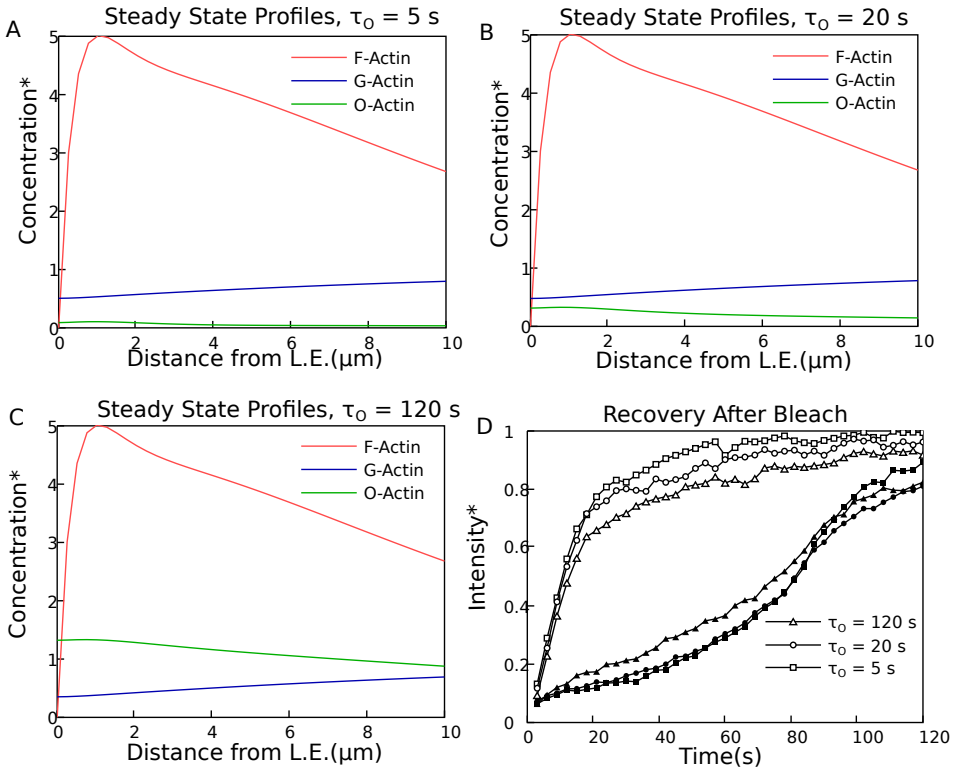

Figure 4.9: Effects on concentration profile and FRAP in model with oligomers due to changing oligomer lifetimes. All other parameters are kept the same as in Fig. 4.8. Profile plots for all three species with (A) $\tau_O = 5$ s, (B) $\tau_O = 20$ s, and (C) $\tau_O = 120$ s. (D) Recovery plot comparing three different recovery curves for the different τ_O (front: empty symbols; back: filled symbols).

(XTC cells versus B16-F1 melanoma cells); the bright illumination required for photobleaching changes the kinetics of the actin in the lamellipodium (for example our preliminary experimental observations show that bright illumination sometimes triggers cell edge retraction); or the protruding or retracting activity of the lamellipodium could affect the turnover.

Here we showed another possibility: a model with both monomers and oligomers (G- and O-actin) agrees with both basal remodeling and two-stage FRAP recovery at the back of the lamellipodium. This agreement requires that O-actin has diffusion coefficient about 10 times smaller than G-actin, which can occur if they consist of a few actin monomers or if they are associated with proteins such as Arp2/3 complex, Aip1, CP protein or VASP tetramers, which bind to multiple actin monomers and to the sides of filaments [199, 200].

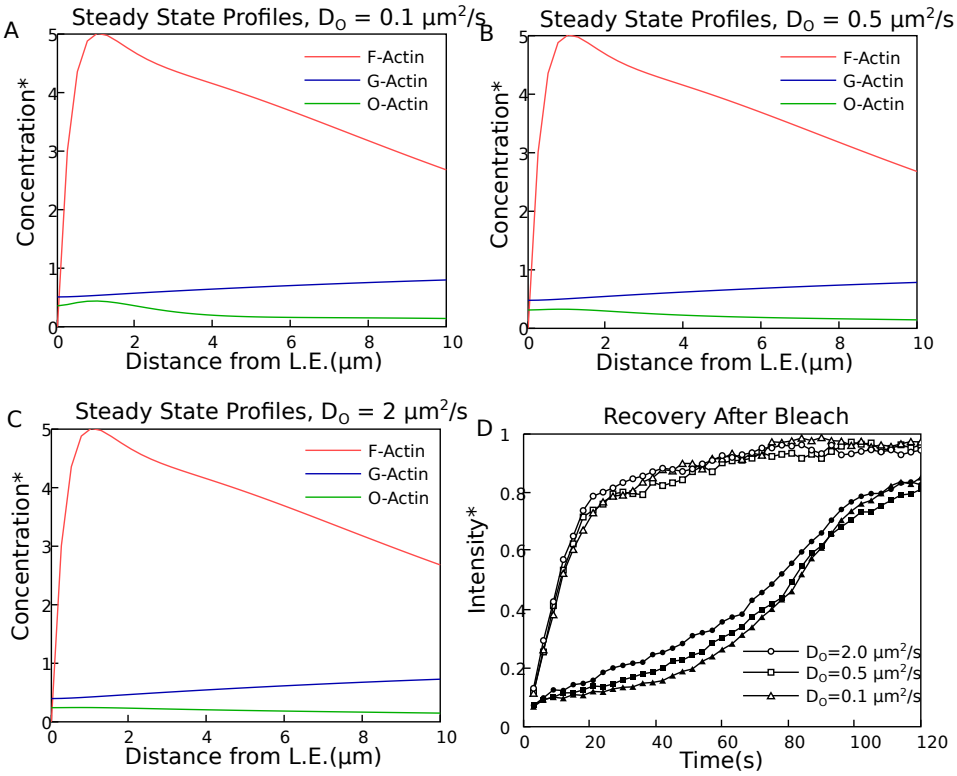

Figure 4.10: Effects on concentration profile and FRAP in model with oligomers due to changing oligomer diffusion coefficients. All other parameters are kept the same as in Fig. 4.8. Profile plots for all three species with (A) $D_O = 0.1$ μm^2/s, (B) $D_O = 0.5$ μm^2/s, and (C) $D_O = 2$ μm^2/s. (D)Recovery plot comparing three different recovery curves for the different D_O (front: empty symbols; back: filled symbols).

In the model with oligomers we assumed that the speckle appearance rate $a(x)$ within 1 μm of the leading edge is mostly coming from monomers (Fig. 4.7B). The appearance rate is the sum of the products of the G→F and O→F transition rates with the local G- and O-actin concentrations. For the parameters of Figs. 4.7 and 4.8 we found that this leads to O-actin to assemble with smaller rate constants (Fig. 4.8A) and to have smaller concentration than G-actin at the very front (Fig. 4.7). This is a reasonable result since it may be harder for O-actin to assemble at barbed ends pushing against the membrane. Although a recent experimental study suggests oligomer polymerization occurs at the leading edge [201]. In some simulations where the O→F and G→F rate constants at the leading edge were similar, as in Fig. 4.9A where $\tau_O = 5$ s, the resulting FRAP recovery was similar to Fig. 4.8C.

In the model with oligomers we also assumed the speckle appearance rate $a(x)$ away from the leading edge is primarily due to O-actin (Fig. 4.7B). We have explored the contribution of both G- and O-actin to the appearances in the basal region by breaking the second term of Eq. 4.1 into two parts, $A_2 = (1-f)A_2 + fA_2$ in Fig. 4.11. The $(1-f)A_2$ term is the portion of G-actin appearances while fA_2 corresponds to the O-actin contribution. Reducing the appearance rate of oligomers causes an accumulation of oligomers, which cannot polymerize; to balance this effect τ_O was adjusted to maintain a similar O-actin concentration. The predicted recovery curves as a function of f are shown in Fig. 4.11. This figure demonstrates that G-actin appearance events away from the leading edge increase the rate of recovery away from the leading edge. Since both monomers and oligomers would bind to free barbed ends, most likely, the real system corresponds to an intermediate f value.

A possible origin for differences between G- and O-actin association rates might be that O-actin has more binding sites away from the leading edge (eg. filament sides). Also, free barbed ends of severed filaments away from the leading edge could be protected by Aip1 that exists at 1.8 μM at the leading edge [191]. Experiments using cells permeabilized by CP have demonstrated an abundance of free barbed ends throughout the lamellipodium [39]. These experiments might label free barbed ends that were protected by Aip1 that dissociated during preparation. This would be consistent with the live cell observations that show Aip1 speckles dissociating at 1 s^{-1} [191] and CP in a narrow region close to the leading edge. A maximal estimated rate of Aip1 capping, 1.8 μM/s, may however fall short of the anticipated oligomer generation rate of order $0.2 \sim G_\infty K$ 10 μM/s in the basal region (see Fig. 4.12C). Another reason G-actin might associate slower in the basal region is because of sequestering proteins, such as thymosin-β4.

Oligomers in the lamellipodium could serve multiple purposes. Control of actin assembly relies on nucleating proteins activated at the leading edge. This leads to autocatalytic polymerization regulated by capping. While this mechanism allows fast response, it consumes energy and may result in misoriented branches. Rather than disassembling branches into monomers, it may be energetically efficient to recycle these segments. Annealing those segments to filaments growing in the preferred direction may provide a geometrical feedback to turn a random branched structure into a polarized network. Another function could be regulation of soluble actin. Due to their slow diffusion coefficient, oligomers may accumulate near the leading edge (Fig.

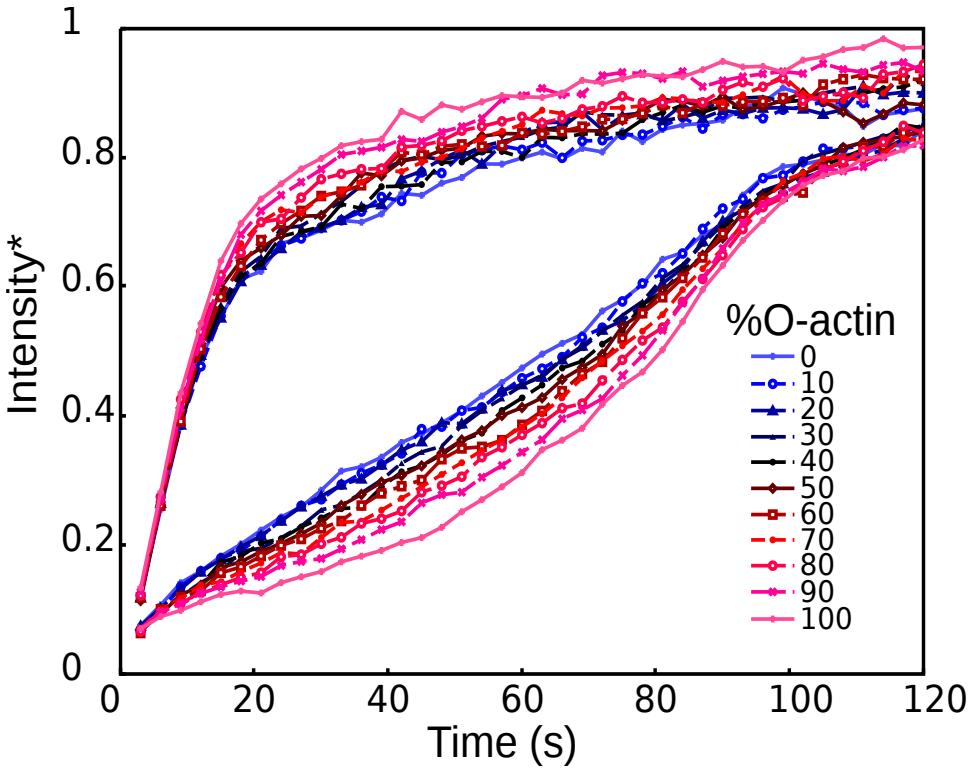

Figure 4.11: Recovery curves for different contributions of O-actin to the appearances away from the leading edge (fraction of A_2 term of Eq. 4.1). The recovery curves for low percentages of O-actin contribution are similar to the monomer-only model. The limit of 100% oligomer contribution is the case of Fig. 4.8. Zero contribution is similar to the monomer-only model (Fig. 4.3) but includes slowly-diffusing O-actin that does not associate. Parameters: $K = 0.5$ s^{-1}, $v_r = 0.03$ μm/s, $D_O = 0.5$ μm^2/s, $D = 4$ μm^2/s. Parameter τ_O was adjusted to keep the F-, G- and O-actin concentrations similar to those in Fig. 4C (top left panel). The value of τ_O was 3.3, 5.7 and 20 s^{-1} at 0%, 50% and 100% O-actin appearances, respectively.

4.9C). Recent experiments showed higher G-actin concentration at the leading edge of growth cones, measured by DNAse1 binding [52]. Our work suggests a possible explanation for this increase, in addition to convective flow [34, 180, 202].

Our model motivates experiments to look for the presence of oligomers and measure their characteristics, for example τ_O and D_O. These parameters influence the amount of blurring of the edges at the boundary of the bleached region. This blurring is hard to detect (see Fig. 4.7B), however, because oligomers are predicted to be a small fraction of the total actin. Fast acquisition (10 ms/frame) SiMS experiments

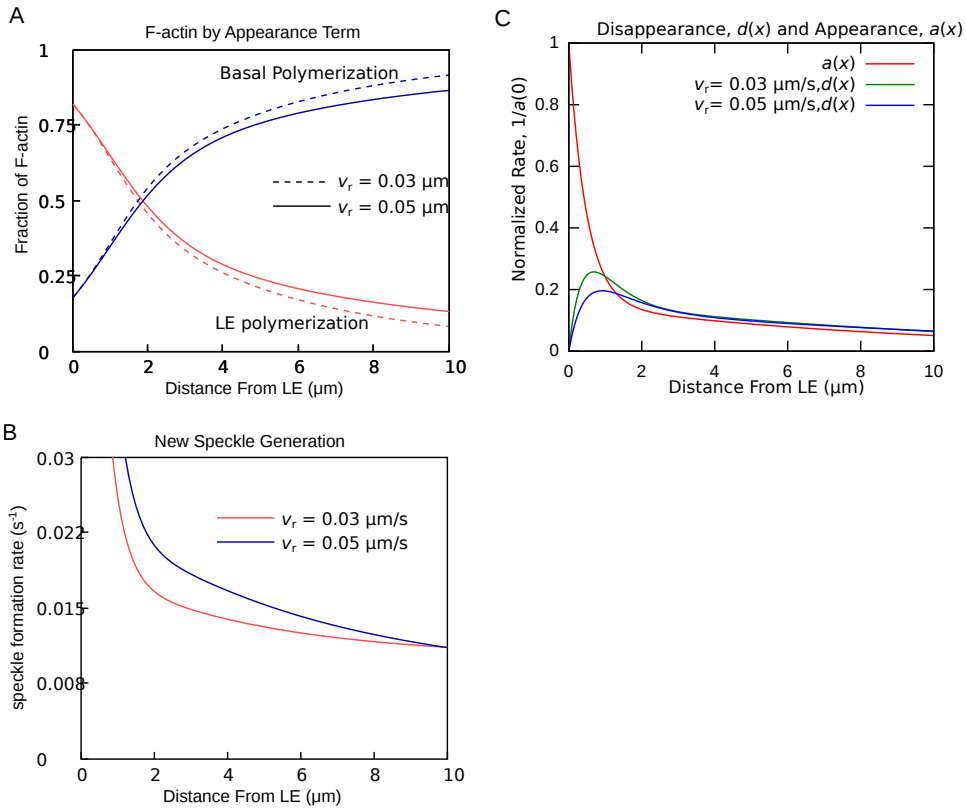

Figure 4.12: Calculations based on single molecule speckle statistics to compare with results in [41]. (A) Analytical results showing the amount of F-actin due to leading edge (LE) or the basal polymerization, using Eq. 4.13. Here we define LE polymerization to be the polymerization events due to the first term in Eq. (1) (the term proportional to A1). Basal polymerization corresponds to the second term (proportional to A_2). The resulting curves are similar to Fig. 4B of Ref. [41]. (B) Plot of relative new speckle formation rate vs distance from LE. This is the rate of speckle appearance, $a(x)$, divided by the amount of F-actin at each location, $F(x)$, calculated using Eq. 4.13. The graph is similar to the experimental measurements in Fig. 3B of Ref. [41] where the value of the new speckle formation rate was around 0.03 s^{-1}. (C) Disassembly rate (Eq. 4.5) as a function of distance from the leading edge normalized to the appearance rate, $a(x)$, at $x = 0$.

could provide some of these details by tracking actual diffusing particles to measure their lifetime and diffusion coefficient [6].

4.4 SUPPLEMENTARY MATERIAL

4.4.1 Calculation of the steady state F-actin profile based on single molecule speckle statistics

To obtain an analytical expression for the F-actin profile based on SiMS data, we substitute Eqs. 4.1 and 4.2 into 4.3 and 4.5 of the main text to obtain

$$F(x) = \frac{G_\infty K}{v_r} \sum_{i=1}^{2} \sum_{j=1}^{2} F_{ij}(x), \tag{4.13}$$

and when $v_r \tau_j \neq \lambda_i$:

$$F_{ij}(x) = \frac{A_i C_j \tau_j}{1/(v_r \tau_j) - 1/\lambda_i} \left(e^{-x/\lambda_i} - e^{-x/(v_r \tau_j)} \right), \tag{4.14}$$

or if $v_r \tau_j = \lambda_i$:

$$F_{ij}(x) = A_i C_j \tau_j e^{-x/(v_r \tau_j)} x. \tag{4.15}$$

For both cases when we solve for the total amount of F-actin, we get the same result,

$$\int_0^\infty F(x) dx = G_\infty K \sum_{i=1}^{2} \sum_{j=1}^{2} A_i C_j \tau_j^2 \lambda_i. \tag{4.16}$$

This result demonstrates that the F-actin concentration is directly proportional to parameter K.

4.4.2 Condition on model parameters to generate positive G-actin profile.

The G-actin profile can be calculated analytically by substituting Eq. 4.13 into Eq. 4.6 of the main text. By using Eq. 4.16 to calculate G-actin at the leading edge, the G-actin will go to zero when

$$\frac{G(0)}{G_\infty} = 1 - \frac{v_r}{D} K \sum_{i=1}^{2} \sum_{j=1}^{2} A_i C_j \tau_j^2 \lambda_i. \tag{4.17}$$

This yields the following inequality that should be satisfied such that G(0) does not become negative:

$$D > v_r K \sum_{i=1}^{2} \sum_{j=1}^{2} A_i C_j \tau_j^2 \lambda_i. \tag{4.18}$$

4.4.3 Picking speckle lifetimes and initializing steady state in stochastic simulations

When a G-actin or O-actin subunit associates to become F-actin, its lifetime as F-actin is picked from the double exponential lifetime distribution of Eq. 4.2, a sum of "long-life" and "short-life" exponentials. We first pick which of the exponential distribution to choose from based on the following probabilities.

$$p(2) = \frac{\tau_2 C_2}{\tau_2 C_2 + \tau_1 C_1}, p(1) = 1 - p(2). \tag{4.19}$$

Then we pick the actual lifetime from the respective exponential distribution.

To initialize the simulations, we distribute particles in space according to the analytically-calculated F-, O- and G-actin distributions. When choosing the lifetime of an F-actin subunit at distance x from the leading edge in the initial state, we must be careful to recognize the possible paths this subunit could have taken to arrive at x. Consider a subunit that converts to F-actin at x whose lifetime belongs to either the long- or short-lived population ($i = 1$ or 2). The probability that the subunit will still exist at x is based on the time it needs to get there:

$$p(x|i, x') = e^{-\frac{x-x'}{v_r \tau_i}} \tag{4.20}$$

Knowing the distribution of appearances, $a(x)$, we can calculate the probability of finding a subunit of type i at x:

$$p(x|i) = \Lambda \int_0^x a(x') e^{-\frac{x-x'}{v_r \tau_i}} dx, \tag{4.21}$$

where Λ is a normalization constant that does not depend on i. Thus we can apply Bayes theorem to determine the probability that a subunit found at x belongs to the long-life population:

$$p(2|x) = \frac{p(x|2)p(2)}{p(x|2)p(2) + p(x|1)p(1)} \tag{4.22}$$

and similarly for $p(1|x)$. During initialization, when a subunit is placed at x, the above probability was used to determine if the lifetime of the subunit is picked from the long-life exponential distribution or the short-life distribution. This expression also gives a way to calculate an effective time constant as a function of position.

$$\tau_{eff}(x) = \tau_2 p(2|x) + \tau_1 p(1|x) \tag{4.23}$$

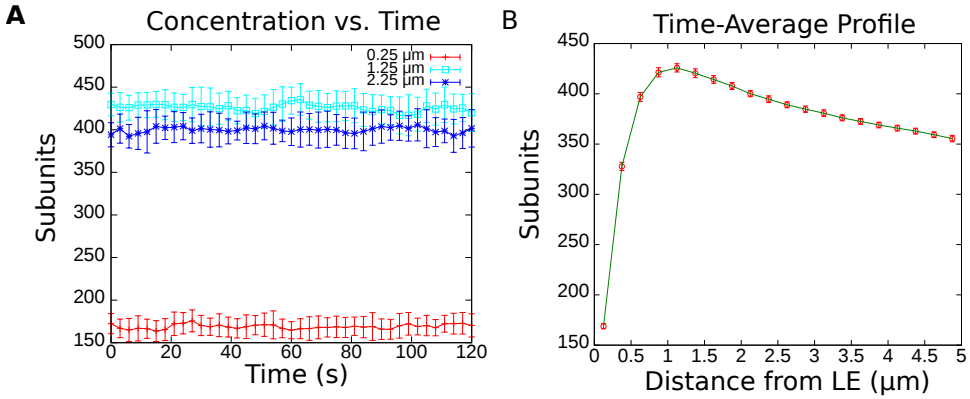

Figure 4.13: Stochastic particle simulation maintains steady state initialized according to analytical expressions for steady state profiles and Eq. 4.22. Example showing monomer-only model with $K = 0.5$ s^{-1}, $v_r = 0.03$ μm/s. (A) 100 simulations with an area of 55 μm x 40 μm were started with the system in steady state. Each system was divided into strips of width 0.25 μm and the number of particles in the strip was measured every 3 s. The values plotted are the average measured value for strips at three different positions. Error bars are the standard deviation among simulations. (B) All of the 0.25 μm strips from 0 to 5 μm were averaged over time from 0 to 120 s to create a profile. The size of the error bars are the standard deviation of the average value sampled every 3 s for 120 s.

The O-actin lifetimes were picked from a single exponential distribution with average lifetime τ_O.

We tested that the simulations maintain the initial steady state over time, thus validating our procedure. Fig. 4.13A shows that the values of local concentrations do not change significantly, and Fig 4.13B shows that the shape of the concentration profile is the same over time.

Chapter 5

Conclusion

The purpose of this research has been to further the study actin dynamics in cells. To achieve this end I have developed image analysis tools to aid in extracting data from fluorescent microscopy images, and I have developed a model for interpreting the data. More specifically, I presented methods used in two programs for improving data collection from fluorescence microcsopy experiments. In the presentation of these techniques I analyzed some of the errors associate with extracting data from images and I described analysis techniques for measuring properties such as: diffusion coefficients, persistence lengths and growth rates. I also developed a model that improves the ability to compare results from two different experimental techniques, SiMS and FRAP. The model showed that there is not enough information to claim SiMS and FRAP experiments contradict each other. Some questions that were not explored yet, but should be seen as possible future work are as follows.

The two experiments, SiMS and FRAP, are performed on different organisms. Each organism could have a different amount of turnover away from the leading edge, which suggests SiMS microscopy should be performed on B16-F1 cells to test for similar speckle appearance profiles and speckle lifetimes. Another contribution that could be important for this analysis is the state of the leading edge during FRAP. If the cell is protruding or retracting during recovery, it could change the amount of turnover that occurs. While we have not excluded the fact that the systems behave differently, we have shown that they are compatible and actually my be capturing different features of the lamellipodium.

Another type of experiment that could be important would be fast acquisition speckle movies, so that diffusing particles could be imaged as they diffuse. This

would be similar to the CP movies in Chapter 3 applied to labeled actin. If oligomers are present then we should see a slowly diffusing population of actin, and preliminary results by Naoki Watanabe's lab suggest this. This would help to identify the type of speckle appearance events that we have assumed in the model of Chapter 4.

Future modeling work should include refining parameters and conditions. For example the retrograde flow and speckle lifetimes are considered space invariant, but there is evidence for variation in these values. The diffusion coefficient was split into two values, but we expect there to be a range of diffusion coefficients corresponding to the length of oligomers. Another variation that should be considered is the protrusion and retraction of the leading edge. Can the same polymerization profile can work for a moving edge or would patterns form that should be experimentally observable?

Bibliography

[1] Min, T. L., Mears, P. J., Golding, I. & Chemla, Y. R. Chemotactic adaptation kinetics of individual escherichia coli cells. *Proc. Natl. Acad. Sci. U.S.A.* **109**, 9869–9874 (2012).

[2] Heinrich, V. & Lee, C. Y. Blurred line between chemotactic chase and phagocytic consumption: an immunophysical single-cell perspective. *J. Cell. Sci.* **124**, 3041–3051 (2011).

[3] Ridley, A. J. Life at the leading edge. *Cell* **145**, 1012–22 (2011).

[4] Sun, S. X., Walcott, S. & Wolgemuth, C. W. Cytoskeletal cross-linking and bundling in motor-independent contraction. *Curr. Biol.* **20**, R649–654 (2010).

[5] Pollard, T. D. Mechanics of cytokinesis in eukaryotes. *Curr. Opin. Cell Biol.* **22**, 50–56 (2010).

[6] Smith, M. B. *et al.* Interactive, computer-assisted tracking of speckle trajectories in fluorescence microscopy: application to actin polymerization and membrane fusion. *Biophys. J.* **101**, 1794–1804 (2011).

[7] Svitkina, T. M. & Borisy, G. G. Arp2/3 complex and actin depolymerizing factor/cofilin in dendritic organization and treadmilling of actin filament array in lamellipodia. *J. Cell Biol.* **145**, 1009–26 (1999).

[8] Huxley, H. E. Electron microscopic studies of the structure of natural and synthetic protein filaments from striated muscles. *J. Mol. Biol.* **7**, 281–308 (1963).

[9] Kondo, H. & Ishiwata, S. Uni-directional growth of F-actin. *J. Biochem.* **79**, 159–171 (1976).

[10] Pollard, T. D. Regulation of actin filament assembly by Arp2/3 complex and formins. *Annu Rev Biophys Biomol Struct* **36**, 451–477 (2007).

[11] Pollard, T. D. Rate constants for the reactions of ATP- and ADP-actin with the ends of actin filaments. *J. Cell Biol.* **103**, 2747–54 (1986).

[12] Pollard, T. D. & Borisy, G. G. Cellular motility driven by assembly and disassembly of actin filaments. *Cell* **112**, 453 – 465 (2003).

[13] Graceffa, P. & Dominguez, R. Crystal structure of monomeric actin in the ATP state. Structural basis of nucleotide-dependent actin dynamics. *J. Biol. Chem.* **278**, 34172–34180 (2003).

[14] Pollard, T. D. & Cooper, J. A. Actin and actin-binding proteins. A critical evaluation of mechanisms and functions. *Annu. Rev. Biochem.* **55**, 987–1035 (1986).

[15] Fujiwara, I., Vavylonis, D. & Pollard, T. D. Polymerization kinetics of ADP- and ADP-Pi-actin determined by fluorescence microscopy. *Proc. Natl. Acad. Sci. U. S. A.* **104**, 8827–8832 (2007).

[16] Bugyi, B. & Carlier, M. F. Control of actin filament treadmilling in cell motility. *Annu Rev Biophys* **39**, 449–470 (2010).

[17] Amann, K. J. & Pollard, T. D. Direct real-time observation of actin filament branching mediated by Arp2/3 complex using total internal reflection fluorescence microscopy. *Proc. Natl. Acad. Sci. U.S.A.* **98**, 15009–15013 (2001).

[18] Nolen, B. J., Littlefield, R. S. & Pollard, T. D. Crystal structures of actin-related protein 2/3 complex with bound ATP or ADP. *Proc. Natl. Acad. Sci. U. S. A.* **101**, 15627–15632 (2004).

[19] Mahaffy, R. E. & Pollard, T. D. Kinetics of the formation and dissociation of actin filament branches mediated by Arp2/3 complex. *Biophys. J.* **91**, 3519–28 (2006).

[20] Boczkowska, M. *et al.* X-ray scattering study of activated Arp2/3 complex with bound actin-WCA. *Structure* **16**, 695–704 (2008).

[21] Wen, K. K., McKane, M., Houtman, J. C. & Rubenstein, P. A. Control of the ability of profilin to bind and facilitate nucleotide exchange from G-actin. *J. Biol. Chem.* **283**, 9444–9453 (2008).

[22] Galkin, V. E. *et al.* Remodeling of actin filaments by ADF/cofilin proteins. *Proc. Natl. Acad. Sci. U.S.A.* **108**, 20568–20572 (2011).

[23] Kim, T., Cooper, J. A. & Sept, D. The interaction of capping protein with the barbed end of the actin filament. *J. Mol. Biol.* **404**, 794–802 (2010).

[24] Weber, A. Actin binding proteins that change extent and rate of actin monomer-polymer distribution by different mechanisms. *Mol. Cell. Biochem.* **190**, 67–74 (1999).

[25] Blanchoin, L., Pollard, T. D. & Mullins, R. D. Interactions of ADF/cofilin, Arp2/3 complex, capping protein and profilin in remodeling of branched actin filament networks. *Curr. Biol.* **10**, 1273–1282 (2000).

[26] Brieher, W. M., Kueh, H. Y., Ballif, B. A. & Mitchison, T. J. Rapid actin monomer-insensitive depolymerization of Listeria actin comet tails by cofilin, coronin, and Aip1. *J. Cell Biol.* **175**, 315–324 (2006).

[27] Wiesner, S. *et al.* A biomimetic motility assay provides insight into the mechanism of actin-based motility. *J. Cell Biol.* **160**, 387–98 (2003).

[28] Kueh, H. Y., Charras, G. T., Mitchison, T. J. & Brieher, W. M. Actin disassembly by cofilin, coronin, and Aip1 occurs in bursts and is inhibited by barbed-end cappers. *J. Cell Biol.* **182**, 341–53 (2008).

[29] Auinger, S. & Small, J. V. Correlated light and electron microscopy of the cytoskeleton. *Methods Cell Biol.* **88**, 257–272 (2008).

[30] Gawlitta, W., Stockem, W., Wehland, J. & Weber, K. Organization and spatial arrangement of fluorescein-labeled native actin microinjected into normal locomoting and experimentally influenced Amoeba proteus. *Cell Tissue Res.* **206**, 181–191 (1980).

[31] Yumura, S. Spatial distribution of fluorescently labeled actin in living Dictyostelium amoebae. *Cell Struct. Funct.* **21**, 189–197 (1996).

[32] Tsien, R. Y. The green fluorescent protein. *Annu. Rev. Biochem.* **67**, 509–544 (1998).

[33] Dickson, R. M., Cubitt, A. B., Tsien, R. Y. & Moerner, W. E. On/off blinking and switching behaviour of single molecules of green fluorescent protein. *Nature* **388**, 355–358 (1997).

[34] Keren, K., Yam, P. T., Kinkhabwala, A., Mogilner, A. & Theriot, J. A. Intracellular fluid flow in rapidly moving cells. *Nat. Cell Biol.* **11**, 1219–24 (2009).

[35] Abraham, V. C., Krishnamurthi, V., Taylor, D. L. & Lanni, F. The actin-based nanomachine at the leading edge of migrating cells. *Biophys. J.* **77**, 1721–32 (1999).

[36] Bailly, M. *et al.* Relationship between Arp2/3 complex and the barbed ends of actin filaments at the leading edge of carcinoma cells after epidermal growth factor stimulation. *J. Cell Biol.* **145**, 331–45 (1999).

[37] Danuser, G. & Waterman-Storer, C. M. Quantitative fluorescent speckle microscopy of cytoskeleton dynamics. *Annu. Rev. Biophys. Biomol. Struct.* **35**, 361–87 (2006).

[38] Engelke, H., Heinrich, D. & Radler, J. O. Probing GFP-actin diffusion in living cells using fluorescence correlation spectroscopy. *Phys. Biol.* **7**, 046014 (2010).

[39] Miyoshi, T. *et al.* Actin-turnover dependent fast dissociation of capping protein in the dendritic nucleation actin network: evidence of frequent filament severing. *J. Cell Biol.* **175**, 947–955 (2006).

[40] Ponti, A. *et al.* Periodic patterns of actin turnover in lamellipodia and lamellae of migrating epithelial cells analyzed by quantitative fluorescent speckle microscopy. *Biophys. J.* **89**, 3456–3469 (2005).

[41] Watanabe, N. & Mitchison, T. J. Single-molecule speckle analysis of actin filament turnover in lamellipodia. *Science* **295**, 1083–1086 (2002).

[42] Jaqaman, K. *et al.* Robust single-particle tracking in live-cell time-lapse sequences. *Nat. Methods* **5**, 695–702 (2008).

[43] Lai, F. P. *et al.* Arp2/3 complex interactions and actin network turnover in lamellipodia. *The EMBO journal* **27**, 982–92 (2008).

[44] Ohashi, K. *et al.* Lim kinase has a dual role in regulating lamellipodium extension by decelerating the rate of actin retrograde flow and the rate of actin polymerization. *J. Biol. Chem.* **286**, 36340–51 (2011).

[45] Ponti, A., Machacek, M., Gupton, S. L., Waterman-Storer, C. M. & Danuser, G. Two distinct actin networks drive the protrusion of migrating cells. *Science* **305**, 1782–6 (2004).

[46] Carrero, G., McDonald, D., Crawford, E., de Vries, G. & Hendzel, M. J. Using FRAP and mathematical modeling to determine the in vivo kinetics of nuclear proteins. *Methods* **29**, 14–28 (2003).

[47] Watanabe, N. Inside view of cell locomotion through single-molecule: fast F-/G-actin cycle and G-actin regulation of polymer restoration. *Proc. Jpn. Acad. Ser. B* **86**, 62–83 (2010).

[48] Kuhn, J. R. & Pollard, T. D. Real-time measurements of actin filament polymerization by total internal reflection fluorescence microscopy. *Biophys. J.* **88**, 1387–1402 (2005).

[49] Li, H. *et al.* Automated actin filament segmentation, tracking, and tip elongation measurements based on open active contour models. In *ISBI'09: Proceedings of the Sixth IEEE international conference on Symposium on Biomedical Imaging*, 1302–1305 (2009).

[50] Theriot, J. A. & Mitchison, T. J. Actin microfilament dynamics in locomoting cells. *Nature* **352**, 126–31 (1991).

[51] Chan, A. Y. *et al.* EGF stimulates an increase in actin nucleation and filament number at the leading edge of the lamellipod in mammary adenocarcinoma cells. *J. Cell Sci.* **111 (Pt 2)**, 199–211 (1998).

[52] Van Goor, D., Hyland, C., Schaefer, A. W. & Forscher, P. The role of actin turnover in retrograde actin network flow in neuronal growth cones. *PloS one* **7**, e30959 (2012).

[53] Smith, M. B. *et al.* Segmentation and tracking of cytoskeletal filaments using open active contours. *Cytoskeleton (Hoboken)* **67**, 693–705 (2010).

[54] Pollard, T. D. & Cooper, J. A. Actin, a central player in cell shape and movement. *Science* **326**, 1208–1212 (2009).

[55] Margolin, W. Sculpting the bacterial cell. *Curr. Biol.* **19**, R812–R822 (2009).

[56] Dumont, S. & Mitchison, T. J. Force and length in the mitotic spindle. *Curr. Biol.* **19**, R749–R761 (2009).

[57] Janson, M. E. & Dogterom, M. A bending mode analysis for growing microtubules: evidence for a velocity-dependent rigidity. *Biophys. J.* **87**, 2723–2736 (2004).

[58] Bicek, A. D., Tzel, E., Kroll, D. M. & Odde, D. J. Analysis of microtubule curvature. *Methods Cell Biol.* **83**, 237–268 (2007).

[59] Bicek, A. D. *et al.* Anterograde microtubule transport drives microtubule bending in LLC-PK1 epithelial cells. *Mol. Biol. Cell* **20**, 2943–2953 (2009).

[60] Brangwynne, C. P. *et al.* Bending dynamics of fluctuating biopolymers probed by automated high-resolution filament tracking. *Biophys. J.* **93**, 346–359 (2007).

[61] Brangwynne, C. P., MacKintosh, F. C. & Weitz, D. A. Force fluctuations and polymerization dynamics of intracellular microtubules. *Proc. Natl. Acad. Sci. U. S. A.* **104**, 16128–16133 (2007).

[62] Brangwynne, C. P., Koenderink, G. H., MacKintosh, F. C. & Weitz, D. A. Nonequilibrium microtubule fluctuations in a model cytoskeleton. *Phys. Rev. Lett.* **100**, 118104 (2008).

[63] Danuser, G., Tran, P. T. & Salmon, E. D. Tracking differential interference contrast diffraction line images with nanometre sensitivity. *J. Microsc.* **198**, 34–53 (2000).

[64] Kas, J. *et al.* F-actin, a model polymer for semiflexible chains in dilute, semidilute, and liquid crystalline solutions. *Biophys. J.* **70**, 609–625 (1996).

[65] Ausmees, N., Kuhn, J. R. & Jacobs-Wagner, C. The bacterial cytoskeleton: An intermediate filament-like function in cell shape. *Cell* **115**, 705–713 (2003).

[66] Chiu, S.-W., Chen, S.-Y. & chung Wong, H. Dynamic localization of MreB in vibrio parahaemolyticus and in the ectopic host bacterium escherichia colitriangledown. *Appl. Environ. Microbiol.* **74**, 6739–6745 (2008).

[67] Kumar, S. *et al.* Viscoelastic retraction of single living stress fibers and its impact on cell shape, cytoskeletal organization, and extracellular matrix mechanics. *Biophys. J.* **90**, 3762–3773 (2006).

[68] Hotulainen, P. & Lappalainen, P. Stress fibers are generated by two distinct actin assembly mechanisms in motile cells. *J. Cell Biol.* **173**, 383–394 (2006).

[69] Hayakawa, K., Tatsumi, H. & Sokabe, M. Actin stress fibers transmit and focus force to activate mechanosensitive channels. *J. Cell Sci.* **121**, 496–503 (2007).

[70] Helmke, B. P., Thakker, D. B., Goldman, R. D. & Davies, P. F. Spatiotemporal analysis of flow-induced intermediate filament displacement in living endothelial cells. *Biophys. J.* **80**, 184–194 (2001).

[71] Luck, S., Sailer, M., Schmidt, V. & Walther, P. Three-dimensional analysis of intermediate filament networks using SEM tomography. *J. Microsc.* (2009).

[72] Mickel, W. *et al.* Robust pore size analysis of filamentous networks from three-dimensional confocal microscopy. *Biophys. J.* **95**, 6072–6080 (2008).

[73] Hadjidemetriou, S., Toomre, D. & Duncan, J. Motion tracking of the outer tips of microtubules. *Med. Image Anal.* **12**, 689–702 (2008).

[74] Saban, M. *et al.* Automated tracking and modeling of microtubule dynamics. In *ISBI'06: Proceedings of IEEE international conference on Symposium on Biomedical Imaging*, 1032–1035 (2006).

[75] Jiang, M., Ji, Q. & McEwen, B. F. Model-based automated extraction of microtubules from electron tomography volume. *IEEE Trans. on Information Technology in Biomedicine* **10**, 608–617 (2006).

[76] Altinok, A. *et al.* Activity analysis in microtubule videos by mixture of hidden markov models. *IEEE Computer Society Conference on Computer Vision and Pattern Recognition* **2**, 1662–1669 (2006).

[77] Hadjidemetriou, S., Duncan, J. S., Toomre, D. & Tuck, D. Automatic quantification of microtubule dynamics. In *ISBI'04: Proceedings of the IEEE international conference on Symposium on Biomedical Imaging*, 656–659 (2004).

[78] Li, H., Shen, T., Vavylonis, D. & Huang, X. Actin filament tracking based on particle filters and stretching open active contour models. In *Medical Image Computing and Computer-Assisted Intervention - MICCAI 2009*, vol. 5762, 673–681 (2009).

[79] Zana, F. & Klein, J. C. Segmentation of vessel-like patterns using mathematical morphology and curvature evaluation. *IEEE Trans. Image Processing* **10**, 1010–1019 (2001).

[80] Hoover, A. D., Kouznetsova, V. & Goldbaum, M. Locating blood vessels in retinal images by piecewise threshold probing of a matched filter response. *IEEE Trans. Medical Imaging* **19**, 203–210 (2000).

[81] Masutani, Y., Schiemann, T. & Hohne, K. H. Vascular shape segmentation and structure extraction using a shape-based region-growing model. In *Proc. Int'l Conf. Medical Image Computing and Computer-Assisted Intervention - MICCAI 1998*, 1242–1249 (1998).

[82] Yuan, X., Trachtenberg, J., Potter, S. M. & Roysam, B. MDL constrained 3-D grayscale skeletonization algorithm for automated extraction of dendrites and spines from fluorescence confocal images. *J. Neuroinformatics* **7**, 213–232 (2009).

[83] Florin, C., Paragios, N. & Williams, J. Particle filters, a quasi-monte carlo solution for segmentation of coronaries. In *Medical Image Computing and Computer-Assisted Intervention - MICCAI 2005*, 246–253 (2005).

[84] Cohen, L. D. & Kimmel, R. Global minimum for active contour models: A minimal path approach. *Int'l Journal of Computer Vision* **24**, 57–78 (1997).

[85] Law, M. W. K. & Chung, A. C. S. A deformable surface model for vascular segmentation. In *Proc. Int'l Conf. Medical Image Computing and Computer-Assisted Intervention - MICCAI 2009*, 59–67 (2009).

[86] Yim, P. J., Cebral, J. J., Mullick, R., Marcos, H. B. & Choyke, P. L. Vessel surface reconstruction with a tubular deformable model. *IEEE Trans. Medical Imaging* **20**, 1411–1421 (2001).

[87] Sarry, L. & Boire, J.-Y. Three-dimensional tracking of coronary arteries from biplane angiographic sequences using parametrically deformable models. *IEEE Trans. Medical Imaging* **20**, 1341–1351 (2001).

[88] Stein, A. M., Vader, D. A., Jawerth, L. M., Weitz, D. A. & Sander, L. M. An algorithm for extracting the network geometry of three-dimensional collagen gels. *J. Microsc.* **232**, 463–475 (2008).

[89] Pool, M., Thiemann, J., Bar-Or, A. & Fournier, A. E. Neuritetracer: a novel imagej plugin for automated quantification of neurite outgrowth. *J. Neurosci. Methods* **168**, 134–139 (2008).

[90] Meijering, E. *et al.* Design and validation of a tool for neurite tracing and analysis in fluorescence microscopy images. *Cytometry A* **58**, 167–176 (2004).

[91] Peng, H., Ruan, Z., Long, F., Simpson, J. H. & Myers, E. W. V3D enables real-time 3D visualization and quantitative analysis of large-scale biological image data sets. *Nat. Biotechnol.* **28**, 348–353 (2010).

[92] Matula, P., Maška, M., Daněk, O., Matula, P. & Kozubek, M. Acquiarium: free software for the acquisition and analysis of 3D images of cells in fluorescence microscopy. In *ISBI'09: Proceedings of the Sixth IEEE international conference on Symposium on Biomedical Imaging*, 1138–1141 (2009).

[93] Kass, M., Witkin, A. & Terzopoulos, D. Snakes: Active contour models. *Int'l Journal of Computer Vision* **1**, 321–331 (1987).

[94] Vavylonis, D., Wu, J.-Q., Hao, S., O'Shaughnessy, B. & Pollard, T. D. Assembly mechanism of the contractile ring for cytokinesis by fission yeast. *Science* **319**, 97–100 (2008).

[95] Gonzalez, R. C. & Woods, R. E. Digital image processing. *Prentice Hall* (2007).

[96] Xu, C. & Prince, J. L. Snakes, shapes, and gradient vector flow. *IEEE Trans. Image Processing* **7**, 359–369 (1998).

[97] Jose, J. V. & Saletan, E. J. *Classical Dynamics* (Cambridge University Press, 1998).

[98] Marko, J. & Siggia, E. Bending and twisting elasticity of DNA. *Macromolecules* **27**, 981–988 (1994).

[99] Landau, L. D. & Lifshitz, E. M. *Statistical Physics*, vol. 5 (Pergamon Press, 1980), third edn.

[100] Giomi, L. & Mahadevan, L. Statistical mechanics of developable ribbons. *Phys. Rev. Lett.* **104**, 238104 (2010).

[101] Rappaport, S. M., Medalion, S. & Rabin, Y. Curvature distribution of worm-like chains in two and three dimensions. *arXiv:0801.3183* (2008).

[102] Gittes, F., Mickey, B., Nettleton, J. & Howard, J. Flexural rigidity of microtubules and actin filaments measured from thermal fluctuations in shape. *J. Cell Biol.* **120**, 923–934 (1993).

[103] Meijering, E., Smal, I. & Danuser, G. Tracking in molecular bioimaging. *IEEE Signal Processing Magazine* **23**, 46–53 (2006).

[104] Isambert, H. *et al.* Flexibility of actin filaments derived from thermal fluctuations. effect of bound nucleotide, phalloidin, and muscle regulatory proteins. *J. Biol. Chem.* **270**, 11437–11444 (1995).

[105] McCullough, B. R., Blanchoin, L., Martiel, J.-L. & la Cruz, E. M. D. Cofilin increases the bending flexibility of actin filaments: implications for severing and cell mechanics. *J. Mol. Biol.* **381**, 550–558 (2008).

[106] Huckaba, T. M., Gay, A. C., Pantalena, L. F., Yang, H.-C. & Pon, L. A. Live cell imaging of the assembly, disassembly, and actin cable-dependent movement of endosomes and actin patches in the budding yeast, saccharomyces cerevisiae. *J. Cell Biol.* **167**, 519–530 (2004).

[107] Wang, H. & Vavylonis, D. Model of For3p-mediated actin cable assembly in fission yeast. *PLoS ONE* **3**, e4078 (2008).

[108] Wagner, F., Latanzi, G. & Frey, E. Conformations of confined biopolymers. *Phys. Rev. E* **75**, 050902(R) (2007).

[109] Cremers, D., Rousson, M. & Deriche, R. A review of statistical approaches to level set segmentation: Integrating color, texture, motion and shape. *Int'l Journal of Computer Vision* **72**, 195–215 (2007).

[110] Li, S. Z. *Markov random field modeling in computer vision* (Springer-Verlag, London, UK, 1995).

[111] Crocker, J. C. & Hoffman, B. D. Multiple-particle tracking and two-point microrheology in cells. *Methods Cell Biol.* **83**, 141–178 (2007).

[112] Meijering, E., Dzyubachyk, O., Smal, I. & van Cappellen, W. A. Tracking in cell and developmental biology. *Semin. Cell Dev. Biol.* **20**, 894–902 (2009).

[113] Jaqaman, K. & Danuser, G. Computational image analysis of cellular dynamics: a case study based on particle tracking. *Cold Spring Harb. Protoc.* (2009).

[114] Wirtz, D. Particle-tracking microrheology of living cells: Principles and applications. *Annu. Rev. Biophys.* **38**, 301–326 (2009).

[115] Brandenburg, B. & Zhuang, X. Virus trafficking - learning from single-virus tracking. *Nat. Rev. Microbiol.* **5**, 197–208 (2007).

[116] Dahan, M. *et al.* Diffusion dynamics of glycine receptors revealed by single-quantum dot tracking. *Science* **302**, 442–5 (2003).

[117] Crocker, J. & Grier, D. G. Methods of digital video microscopy for colloidal studies. *J. Colloid Interface Sci.* **179** (1995).

[118] Anantharam, A., Onoa, B., Edwards, R. H., Holz, R. W. & Axelrod, D. Localized topological changes of the plasma membrane upon exocytosis visualized by polarized TIRFM. *J. Cell Biol.* **188**, 415–28 (2010).

[119] Karatekin, E. *et al.* A 20-nm step toward the cell membrane preceding exocytosis may correspond to docking of tethered granules. *Biophys. J.* **94**, 2891–905 (2008).

[120] Lopez, J. A. *et al.* Identification of a distal GLUT4 trafficking event controlled by actin polymerization. *Mol. Biol. Cell* **20**, 3918–29 (2009).

[121] Zenisek, D., Steyer, J. A. & Almers, W. Transport, capture and exocytosis of single synaptic vesicles at active zones. *Nature* **406**, 849–54 (2000).

[122] Needleman, D. J. *et al.* Fast microtubule dynamics in meiotic spindles measured by single molecule imaging: evidence that the spindle environment does not stabilize microtubules. *Mol. Biol. Cell* **21**, 323–33 (2010).

[123] Aratyn-Schaus, Y., Oakes, P. W. & Gardel, M. L. Dynamic and structural signatures of lamellar actomyosin force generation. *Mol. Biol. Cell* **22**, 1330–1339 (2011).

[124] http://physics.nyu.edu/grierlab/software.html.

[125] Gao, Y. & Kilfoil, M. L. Accurate detection and complete tracking of large populations of features in three dimensions. *Opt. Express* **17**, 4685–4704 (2009).

[126] http://www.physics.emory.edu/ weeks/idl.

[127] Rogers, S. S., Waigh, T. A., Zhao, X. & Lu, J. R. Precise particle tracking against a complicated background: polynomial fitting with gaussian weight. *Phys. Biol.* **4**, 220–7 (2007).

[128] Mashanov, G. I. & Molloy, J. E. Automatic detection of single fluorophores in live cells. *Biophys. J.* **92**, 2199–2211 (2007).

[129] http://www.nimr.mrc.ac.uk/gmimpro.

[130] Serge, A., Bertaux, N., Rigneault, H. & Marguet, D. Dynamic multiple-target tracing to probe spatiotemporal cartography of cell membranes. *Nat. Methods* **5**, 687–694 (2008).

[131] Matov, A. *et al.* Analysis of microtubule dynamic instability using a plus-end growth marker. *Nat. Methods* **7**, 761–8 (2010).

[132] http://www.mosaic.ethz.ch/downloads/particletracker.

[133] Sbalzarini, I. F. & Koumoutsakos, P. Feature point tracking and trajectory analysis for video imaging in cell biology. *J. Struct. Biol.* **151**, 182–95 (2005).

[134] http://www.imagescience.org/meijering/software/mtrackj/.

[135] Sage, D., Neumann, F. R., Hediger, F., Gasser, S. M. & Unser, M. Automatic tracking of individual fluorescence particles: application to the study of chromosome dynamics. *IEEE Trans. Image Process.* **14**, 1372–83 (2005).

[136] Huet, S. *et al.* Analysis of transient behavior in complex trajectories: application to secretory vesicle dynamics. *Biophys. J.* **91**, 3542–59 (2006).

[137] http://athena.physics.lehigh.edu/speckletrackerj/.

[138] Karatekin, E. *et al.* A fast, single-vesicle fusion assay mimics physiological SNARE requirements. *Proc. Natl. Acad. Sci. U. S. A.* **107**, 3517–21 (2010).

[139] Cheezum, M. K., Walker, W. F. & Guilford, W. H. Quantitative comparison of algorithms for tracking single fluorescent particles. *Biophys. J.* **81**, 2378–88 (2001).

[140] Savin, T. & Doyle, P. S. Static and dynamic errors in particle tracking microrheology. *Biophys. J.* **88**, 623–638 (2005).

[141] Michalet, X. Mean square displacement analysis of single-particle trajectories with localization error: Brownian motion in an isotropic medium. *Phys. Rev. E Stat. Nonlin. Soft Matter Phys.* **82**, 041914 (2010).

[142] Kim, K. *et al.* Structure/function analysis of the interaction of phosphatidylinositol 4,5-bisphosphate with actin-capping protein: implications for how capping protein binds the actin filament. *J. Biol. Chem.* **282**, 5871–9 (2007).

[143] Fujiwara, I., Remmert, K. & Hammer, r., J. A. Direct observation of the uncapping of capping protein-capped actin filaments by CARMIL homology domain 3. *J. Biol. Chem.* **285**, 2707–20 (2010).

[144] Kuhn, J. R. & Pollard, T. D. Single molecule kinetic analysis of actin filament capping. polyphosphoinositides do not dissociate capping proteins. *J. Biol. Chem.* **282**, 28014–24 (2007).

[145] Goulian, M. & Simon, S. M. Tracking single proteins within cells. *Biophys. J.* **79**, 2188–2198 (2000).

[146] McGrath, J. L., Tardy, Y., Dewey, J., C. F., Meister, J. J. & Hartwig, J. H. Simultaneous measurements of actin filament turnover, filament fraction, and monomer diffusion in endothelial cells. *Biophys. J.* **75**, 2070–8 (1998).

[147] Yang, G. *et al.* Architectural dynamics of the meiotic spindle revealed by single-fluorophore imaging. *Nat. Cell Biol.* **9**, 1233–42 (2007).

[148] Hu, C. *et al.* Fusion of cells by flipped SNAREs. *Science* **300**, 1745–9 (2003).

[149] Weber, T. *et al.* SNAREpins: minimal machinery for membrane fusion. *Cell* **92**, 759–72 (1998).

[150] Bowen, M. E., Weninger, K., Brunger, A. T. & Chu, S. Single molecule observation of liposome-bilayer fusion thermally induced by soluble N-ethyl maleimide sensitive-factor attachment protein receptors (SNAREs). *Biophys. J.* **87**, 3569–84 (2004).

[151] Domanska, M. K., Kiessling, V., Stein, A., Fasshauer, D. & Tamm, L. K. Single vesicle millisecond fusion kinetics reveals number of SNARE complexes optimal for fast SNARE-mediated membrane fusion. *J. Biol. Chem.* **284**, 32158–66 (2009).

[152] Fix, M. *et al.* Imaging single membrane fusion events mediated by SNARE proteins. *Proc. Natl. Acad. Sci. U. S. A.* **101**, 7311–6 (2004).

[153] Liu, T., Tucker, W. C., Bhalla, A., Chapman, E. R. & Weisshaar, J. C. SNARE-driven, 25-millisecond vesicle fusion in vitro. *Biophys. J.* **89**, 2458–72 (2005).

[154] Deverall, M. A. *et al.* Transbilayer coupling of obstructed lipid diffusion in polymer-tethered phospholipid bilayers. *Soft Matter* **4**, 1899–1908 (2008).

[155] Sebastian, R. *et al.* Spatio-temporal analysis of constitutive exocytosis in epithelial cells. *IEEE/ACM Trans. Comput. Biol. Bioinform.* **3**, 17–32 (2006).

[156] Mele, K. *et al.* Automatic identification of fusion events in TIRF microscopy image sequences. In *Computer Vision Workshops (ICCV Workshops), 2009 IEEE 12th International Conference on*, 578–584 (2009).

[157] Axelrod, D., Burghardt, T. P. & Thompson, N. L. Total internal reflection fluorescence. *Annu. Rev. Biophys. Bioeng.* **13**, 247–68 (1984).

[158] Wu, P. H., Arce, S. H., Burney, P. R. & Tseng, Y. A novel approach to high accuracy of video-based microrheology. *Biophys. J.* **96**, 5103–5111 (2009).

[159] Wu, P. H., Agarwal, A., Hess, H., Khargonekar, P. P. & Tseng, Y. Analysis of video-based microscopic particle trajectories using kalman filtering. *Biophys. J.* **98**, 2822–2830 (2010).

[160] Thompson, R. E., Larson, D. R. & Webb, W. W. Precise nanometer localization analysis for individual fluorescent probes. *Biophys. J.* **82**, 2775–2783 (2002).

[161] Berglund, A. J. Statistics of camera-based single-particle tracking. *Phys. Rev. E Stat. Nonlin. Soft Matter Phys.* **82**, 011917 (2010).

[162] Acharya, T. & Ray, A. *Image Processing: Principles and Applications* (Wiley-Interscience, 2005).

[163] Press, W. H., Teukolsky, S. A., Vetterling, W. T. & Flannery, B. P. *Numerical Recipes: The Art of Scientific Computing* (Cambridge University Press, 2007).

[164] Svitkina, T. M., Verkhovsky, A. B., McQuade, K. M. & Borisy, G. G. Analysis of the actin-myosin ii system in fish epidermal keratocytes: mechanism of cell body translocation. *J. Cell Biol.* **139**, 397–415 (1997).

[165] Ridley, A. J. *et al.* Cell migration: integrating signals from front to back. *Science* **302**, 1704–9 (2003).

[166] Hotulainen, P., Paunola, E., Vartiainen, M. K. & Lappalainen, P. Actin-depolymerizing factor and cofilin-1 play overlapping roles in promoting rapid F-actin depolymerization in mammalian nonmuscle cells. *Mol. Biol. Cell* **16**, 649–664 (2005).

[167] Le Clainche, C. & Carlier, M. F. Regulation of actin assembly associated with protrusion and adhesion in cell migration. *Physiol. Rev.* **88**, 489–513 (2008).

[168] Tardy, Y., McGrath, J. L., Hartwig, J. H. & Dewey, C. F. Interpreting photoactivated fluorescence microscopy measurements of steady-state actin dynamics. *Biophys. J.* **69**, 1674–82 (1995).

[169] Carrero, G., Crawford, E., Hendzel, M. J. & de Vries, G. Characterizing fluorescence recovery curves for nuclear proteins undergoing binding events. *Bull. Math. Biol.* **66**, 1515–45 (2004).

[170] Schreiber, C. H., Stewart, M. & Duke, T. Simulation of cell motility that reproduces the force-velocity relationship. *Proc. Natl. Acad. Sci. U. S. A.* **107**, 9141–6 (2010).

[171] Mogilner, A. & Edelstein-Keshet, L. Regulation of actin dynamics in rapidly moving cells: a quantitative analysis. *Biophys. J.* **83**, 1237–58 (2002).

[172] Michalski, P. J. & Carlsson, A. E. The effects of filament aging and annealing on a model lamellipodium undergoing disassembly by severing. *Phys. Biol.* **7**, 026004 (2010).

[173] Kuznetsov, I. R., Herant, M. & Dembo, M. Analysis of actin flap dynamics in the leading lamella. *PloS one* **5**, e10082 (2010).

[174] Novak, I. L., Slepchenko, B. M. & Mogilner, A. Quantitative analysis of G-actin transport in motile cells. *Biophys. J.* **95**, 1627–38 (2008).

[175] Stuhrmann, B., Huber, F. & Kas, J. Robust organizational principles of protrusive biopolymer networks in migrating living cells. *PloS one* **6**, e14471 (2011).

[176] Huber, F., Kas, J. & Stuhrmann, B. Growing actin networks form lamellipodium and lamellum by self-assembly. *Biophys. J.* **95**, 5508–23 (2008).

[177] Ditlev, J. A., Vacanti, N. M., Novak, I. L. & Loew, L. M. An open model of actin dendritic nucleation. *Biophys. J.* **96**, 3529–42 (2009).

[178] Kapustina, M., Vitriol, E., Elston, T. C., Loew, L. M. & Jacobson, K. Modeling capping protein FRAP and CALI experiments reveals in vivo regulation of actin dynamics. *Cytoskeleton* **67**, 519–34 (2010).

[179] Ryan, G. L., Petroccia, H. M., Watanabe, N. & Vavylonis, D. Excitable actin dynamics in lamellipodial protrusion and retraction. *Biophys. J.* **102**, 1493–502 (2012).

[180] Zicha, D. *et al.* Rapid actin transport during cell protrusion. *Science* **300**, 142–5 (2003).

[181] Kiuchi, T., Nagai, T., Ohashi, K. & Mizuno, K. Measurements of spatiotemporal changes in g-actin concentration reveal its effect on stimulus-induced actin assembly and lamellipodium extension. *J. Cell Biol.* **193**, 365–80 (2011).

[182] Koestler, S. A. *et al.* F- and G-actin concentrations in lamellipodia of moving cells. *PloS one* **4**, e4810 (2009).

[183] Cramer, L. P., Briggs, L. J. & Dawe, H. R. Use of fluorescently labelled deoxyribonuclease I to spatially measure G-actin levels in migrating and non-migrating cells. *Cell Motil. Cytoskeleton* **51**, 27–38 (2002).

[184] Kiuchi, T., Ohashi, K., Kurita, S. & Mizuno, K. Cofilin promotes stimulus-induced lamellipodium formation by generating an abundant supply of actin monomers. *J. Cell Biol.* **177**, 465–76 (2007).

[185] Henty, J. L. *et al.* Arabidopsis actin depolymerizing factor4 modulates the stochastic dynamic behavior of actin filaments in the cortical array of epidermal cells. *The Plant cell* **23**, 3711–26 (2011).

[186] Chan, C., Beltzner, C. C. & Pollard, T. D. Cofilin dissociates Arp2/3 complex and branches from actin filaments. *Curr. Biol.* **19**, 537–45 (2009).

[187] Bernstein, B. W. & Bamburg, J. R. ADF/cofilin: a functional node in cell biology. *Trends Cell Biol.* **20**, 187–95 (2010).

[188] Cai, L., Makhov, A. M., Schafer, D. A. & Bear, J. E. Coronin 1B antagonizes cortactin and remodels Arp2/3-containing actin branches in lamellipodia. *Cell* **134**, 828–842 (2008).

[189] Hill, T. L. Length dependence of rate constants for end-to-end association and dissociation of equilibrium linear aggregates. *Biophys. J.* **44**, 285–8 (1983).

[190] Andrianantoandro, E., Blanchoin, L., Sept, D., McCammon, J. A. & Pollard, T. D. Kinetic mechanism of end-to-end annealing of actin filaments. *J. Mol. Biol.* **312**, 721–30 (2001).

[191] Tsuji, T., Miyoshi, T., Higashida, C., Narumiya, S. & Watanabe, N. An order of magnitude faster AIP1-associated actin disruption than nucleation by the Arp2/3 complex in lamellipodia. *PloS one* **4**, e4921 (2009).

[192] Okreglak, V. & Drubin, D. G. Loss of Aip1 reveals a role in maintaining the actin monomer pool and an in vivo oligomer assembly pathway. *J. Cell Biol.* **188**, 769–777 (2010).

[193] Okada, K. *et al.* Xenopus actin-interacting protein 1 (XAip1) enhances cofilin fragmentation of filaments by capping filament ends. *J. Biol. Chem.* **277**, 43011–6 (2002).

[194] Ydenberg, C. A., Smith, B. A., Breitsprecher, D., Gelles, J. & Goode, B. L. Cease-fire at the leading edge: new perspectives on actin filament branching, debranching, and cross-linking. *Cytoskeleton* **68**, 596–602 (2011).

[195] Yang, C. & Svitkina, T. Visualizing branched actin filaments in lamellipodia by electron tomography. *Nat. Cell Biol.* **13**, 1012–3; author reply 1013–4 (2011).

[196] Vinzenz, M. *et al.* Actin branching in the initiation and maintenance of lamellipodia. *J. Cell Sci.* (2012).

[197] Urban, E., Jacob, S., Nemethova, M., Resch, G. P. & Small, J. V. Electron tomography reveals unbranched networks of actin filaments in lamellipodia. *Nat. Cell Biol.* **12**, 429–35 (2010).

[198] Pack, C., Saito, K., Tamura, M. & Kinjo, M. Microenvironment and effect of energy depletion in the nucleus analyzed by mobility of multiple oligomeric egfps. *Biophys. J.* **91**, 3921–3936 (2006).

[199] Hansen, S. D. & Mullins, R. D. VASP is a processive actin polymerase that requires monomeric actin for barbed end association. *J. Cell Biol.* **191**, 571–84 (2010).

[200] Breitsprecher, D. *et al.* Clustering of VASP actively drives processive, WH2 domain-mediated actin filament elongation. *The EMBO journal* **27**, 2943–54 (2008).

[201] Amin, L., Ercolini, E., Shahapure, R., Bisson, G. & Torre, V. The elementary events underlying force generation in neuronal lamellipodia. *Scientific reports* **1**, 153 (2011).

[202] Craig, E. M., Van Goor, D., Forscher, P. & Mogilner, A. Membrane tension, myosin force, and actin turnover maintain actin treadmill in the nerve growth cone. *Biophys. J.* **102**, 1503–13 (2012).

Matthew B. Smith

16 Memorial Drive East, Department of Physics.
Bethlehem, PA. 18015
(610)758-2497 - mbs207@lehigh.edu

Current Research

Modeling the dynamics of proteins using data collected from single-molecule speckle microscopy experiments. Developing and implementing tools to analyze fluorescent images of live cells.

Education

- 2007-2012, Maintaining 3.8 GPA in Ph. D. Physics Lehigh University.(Expected graduation September 2012)
- 2004-2006, B.S. Physics, Summa Cum Laude. California State University Chico.
- 1997-2002, B.S. Mechanical Engineering, California State University Chico.

Achievements

- 2011 Selected to attended the 61st Lindau Nobel Laureate Meeting, Lindau Germany.
- 2008 Yoshida Travel Award (Department of Physics, Lehigh University)
- 2007-2009 GAANN Fellowship (Grant from the U.S. department of Education to Lehigh University Department of Physics) which required a teaching assignment.
- 2002-2004 Completed Peace Corps two year service in The Gambia, West Africa. teaching math and science to students grades 7-9.

Publications

- "Two State Model For Polymerization Kinetics." Matthew B. Smith and Dimitrios Vavylonis, in preparation.

- "Model of Actin Turnover in the Lamellipodium Suggests Remodeling through Slowly Diffusing Oligomers." Matthew B. Smith, Naoki Watanabe, Dimitrios Vavylonis *Under Revision*

- "Interactive, Computer-Assisted Tracking of Speckle Trajectories in Fluorescence Microscopy: Application to Actin Polymerization and Membrane Fusion," Matthew B. Smith, Erdem Karatekin, Andrea Gohlke, Hiroaki Mizuno, Naoki Watanabe, and Dimitrios Vavylonis, Biophys. J. 101, 1794-1804 (2011).

- "Segmentation and Tracking of Cytoskeletal Filaments using Open Active Contours," M. B. Smith, H. Li, T. Shen, X. Huang, E. Yusuf, and D. Vavylonis, Cytoskeleton (Hoboken) 67, 693-705 (2010).

- "Automated Actin Filament Segmentation, Tracking, and Tip Elongation Measurements based on Open Active Contour Models," H. Li, T. Shen, M. B. Smith, I. Fujiwara, D. Vavylonis, and X. Huang, Proc IEEE Int. Symp. Biomed Imaging. 2009:1302-1305 (2009).

Open Source Software from Publications

Speckle TrackerJ, for tracking point-like particles in 2D images.
http://athena.physics.lehigh.edu/speckletrackerj

JFilaments, for tracking filament structures in 2D and 3D images.
http://athena.physics.lehigh.edu/jfilament

Conferences

- "Model of actin turnover and the role of slowly diffusing oligomers in the lamellipodium," Matthew B. Smith and Dimitrios Vavylonis, Biophysical Society Annual Meeting 2012, San Diego, CA.

- "Model of Actin Turnover in the Lamellipodium that Reconciles Prior Experiment Results," (poster presentation, Matthew B. Smith, Naoki Watanabe, and

Dimitrios Vavylonis) 2011 American Society for Cell Biology Annual Meeting, Denver, CO.

- "Segmentation and Tracking of Cytoskeletal Filaments using Open Active Contours." (poster presentation, M. B. Smith, H. Li, T. Shen, X. Huang, E. Yusuf, D. Vavylonis). 2010 American Society for Cell Biology Annual Meeting, Philadelphia, PA.

- "Turnover Dynamics of Diffuse Actin and Regulators at the Leading edge", (oral presentation, Matthew B. Smith, Naoki Watanabe and Dimitrios Vavylonis). 2010 Biophysical Society Annual Meeting, San Francisco, CA.

- "Segmentation and Tracking of Cytoskeletal Filaments using Open Active Contours." (poster presentation, M. B. Smith, H. Li, T. Shen, X. Huang, E. Yusuf, D. Vavylonis). The Cellular Cytoskeleton workshop, Pingree Park, CO. 2010.

- "Actin Filament Segmentation and Tracking using Active Contours,(poster presentation," M. B. Smith, D. Vavylonis, T. Shen, H. Li, X. Huang, M. Fedorka, A. Ruby, L. Vasko). 2009 Computational Science and Engineering/HPC Workshop, Lehigh University, Bethlehem, PA.

- "Mechanisms of large length fluctuations during actin filament growth," (poster presentation Matthew B. Smith, Dimitrios Vavylonis). 2009 Biophysical Society Annual Meeting, Boston, MA.

- "Turnover dynamics of diffuse actin and regulators at the leading edge," (poster presentation, Matthew B. Smith, Naoki Watanabe and Dimitrios Vavylonis). 2009 American Society for Cell Biology Annual Meeting, San Diego, CA.

- "Mechanisms of large length Fluctuations during actin Filament growth," (oral presentation, Matthew B. Smith, Dimitrios Vavylonis). 2009 The American Physical Society March Meeting, Pittsburgh, PA.

- "The effect of cooperative polymerization kinetics in actin filament elongation rate and length fluctuations," (poster presentation, M.B. Smith and D. Vavylonis). 2009 Lehigh University Research Symposium.